RADIATIVE TRANSFER IN THE MARTIAN ENVIRONMENT: IN-SITU RESULTS FROM THE MSL CURIOSITY ROVER AND LABORATORY EXPERIMENTATION ON MARTIAN REGOLITH AND CRYSTALLINE ROCK ANALOGS

CASEY A MOORE

A DISSERTATION SUBMITTED TO
THE FACULTY OF GRADUATE STUDIES
IN PARTIAL FULFILMENT OF THE REQUIREMENTS
FOR THE DEGREE OF

DOCTOR OF PHILOSOPHY

GRADUATE PROGRAM IN EARTH & SPACE SCIENCE
YORK UNIVERSITY
TORONTO, ONTARIO

January 2019

Abstract

Global circulation models predicted a suppressed planetary boundary layer within Gale Crater prior to the landing of the Mars Science Laboratory. Images from Mars allow the amount of suspended dust near the crater floor to be estimated numerically. The atmosphere within the crater is shown to be relatively dust free compared to the amount of dust inferred in the atmospheric column, suggesting little mixing between the upper and lower layers. The dust within the crater appears to be well mixed horizontally, implying that dust events (such as dust devils or lateral dust transport) in the northern plains of Gale Crater are rare, even during the most convective time of day. This supports the notion of a suppressed planetary boundary layer within Gale Crater.

Radiative transfer modeling of the martian atmosphere benefits from this quantification of low-lying dust. This dissertation aims to expand our knowledge of the radiation environment of Mars into its surface and subsurface.

The scattering of radiation through analog martian materials is an area with little research. A mini-goniometer is built to collect transmission spectra as a function of scattering angle for martian analog regoliths and crystalline rock samples. Materials show strong forward or isotropic scattering profiles through the samples. The transmission through the materials is assessed at ultraviolet and visible wavelengths. Kieserite and the majority of the rock samples exhibit an isotropic scattering profile and attenuate ultraviolet radiation significantly.

Ultraviolet shielding materials are potential ecological niches for biosignatures, and this dissertation aims to guide the search for these environments on present day Mars.

Studies into the habitability of martian surface analogs typically assess the amount of

radiation transmitting perpendicular into a surface. This does not fully characterize the multiple surface scattering that exists within these materials. The depths at which radioresistant microorganisms can exist on present day Mars are estimated by modeling the isotropic transmission scattering profiles for kieserite and crystalline rocks under martian insolation. A depth between 2 and 10 mm into the martian subsurface is enough to attenuate ultraviolet radiation to levels suitable to terrestrial radioresistant microorganisms.

–

Dedicated to my grandfather for showing me the many worlds beyond our own.

–

Acknowledgements

First and foremost, I would like to thank Dr. John Moores for taking me on as his first Ph.D. student. It was through his mentorship that I began to believe that my contributions to planetary science are meaningful. He has been crucial to my current and future success as a planetary scientist.

I would like to thank the Canadian Space Agency for funding which allowed me to be part of the Mars Science Laboratory.

I would like to thank the many early, mid, and late career scientists I have met through conferences, colloquia, my daily interactions at York University, and the numerous members of the Mars Science Laboratory's Science Team.

A large portion of the data acquisition for this dissertation was taken on by a large team of undergraduate students throughout the years at York University. I am deeply grateful for their involvement and I can only hope that they, themselves, benefited from the experience.

To my peers: thank you for being part of this journey, thank you for your help, thank you for your friendship. I wish you success and hope our paths cross in the future.

To my parents and grandparents: thanks for all the support and instilling in me a sense of curiosity. Without which, many of my dreams may not have come to fruition.

Lastly, I am very thankful to have had the support of my partner, Jonathan De Leon. Without you by my side, this journey would not have been the same.

Table of Contents

List of Tables

List of Figures

1 Introduction

1.1 Radiation Environment of Mars

Given that Mars is roughly 1.5× further away from the Sun than is the Earth, and that solar flux falls off as $1/r^2$, a novice might assume that the radiation environment of Mars is simply that of Earths' but scaled down by 55%. This would be true if both Earth and Mars had no atmosphere, as the top of the atmosphere (TOA) solar flux of Mars should be 45% of those seen at TOA on Earth.

The wavelength dependent intensities that make it from TOA to the surface of a planet are dictated by the density and composition of its atmosphere. Earth's atmosphere averages 1013 mbar at sea level and is composed primarily of N_2 and O_2, with trace amounts of water vapor and ozone dictating the energy balance. Mars, on the other hand, has a thin, 7 mbar, mostly CO_2 surface pressure (Zurek et al., 1992). Because of that, Mars' atmosphere is much more transparent than Earths in the context of ultraviolet (UV) radiation (Gómez-Elvira et al., 2014; Nicholson et al., 2005).

Due to the thin atmosphere on Mars, dust plays a critical role in dictating the amount of solar radiation that is absorbed and scattered as it passes through the atmosphere (Gierasch

and Goody, 1972; Gómez-Elvira et al., 2014; Smith et al., 2016), ultimately making its way to the surface. Telescopic, orbital, and in situ observations of the martian atmosphere have observed dust storms ranging from global (McKim, 1999; Smith, 2004, 2009) to local (Cantor et al., 2001; Wang and Richardson, 2015; Wang et al., 2003) in scale. These dust events have been observed to have a predictable seasonal and multi-annual cycle (Lemmon et al., 2015; Montabone et al., 2015).

To better understand the seasonal cycles of dust in the martian atmosphere, it is necessary to first introduce two basic time-keeping conventions. Figure 1.1 shows an illustration of the martian year. Seasons are defined by the position of Mars in its solar orbit, known as its solar longitude (L_S). By convention, most recent works in the literature adopt the counting of Mars Years (MY) from Piqueux et al. (2015), in which MY1, $L_s = 0^\circ$ corresponds to an Earth date of April 11, 1955. Over the last several decades studies were conducted to measure the amount (Cantor, 2007; Hunt et al., 1980; James et al., 1994; Montabone et al., 2015) and physical characteristics (Clancy et al., 1995, 2003; Pollack et al., 1977; Tomasko et al., 1999) of martian atmospheric dust in order to further our knowledge of the radiation environment of the martian atmosphere.

Montabone et al. (2015) compiles a near 8 Mars year record of dust column optical depth, a measure of the amount of dust in the atmospheric column, by combining multiple datasets from orbiting spacecraft and interpolation. Reproduced in Figure 1.2 is the zonal mean dust column optical depth as a function of L_S and latitude for MY24 to MY31. Note how larger opacities are seen in the later half of the Mars year and are predominately observed

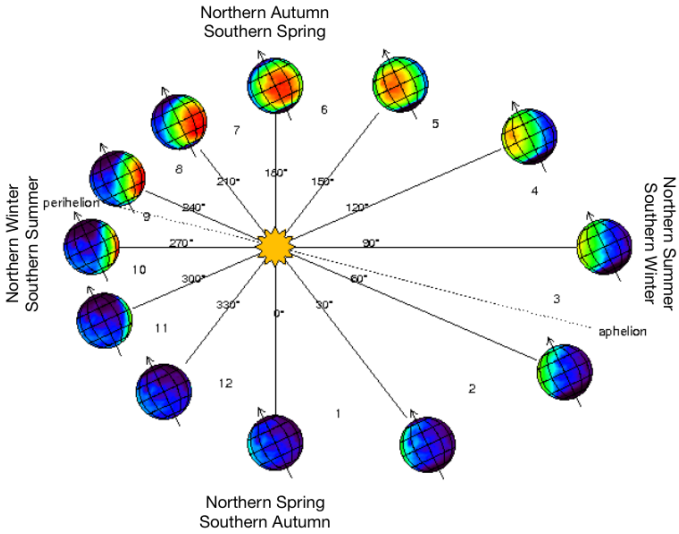

Figure 1.1: *Orbit of Mars*

Illustration of the orbit of Mars relating to the convention of time keeping on Mars in the literature. Seasons are defined as a function of solar longitude (L_S). Not to scale.

Image adapted from:

http : //www − mars.lmd.jussieu.fr/mars/time/solar_longitude.html

in the southern hemisphere. Intuitively, it makes sense that the majority of dust events originate in the southern hemisphere. Perihelion and southern summer align in such a way that make southern summers much warmer than northern summers, and hence creating the atmospheric dynamics necessary to loft surface dusts.

With the arrival of the Mars Exploration Rovers, Spirit (Arvidson et al., 2006) and Opportunity (Squyres et al., 2004) in 2006, a continual long history of column optical depths (Lemmon et al., 2015) from Mars surface-based instruments began. Opportunity and the Mars Science Laboratory (Grotzinger et al., 2012) rover, Curiosity, which landed in August 2012, have been making concurrent optical depth measurements for more than 3 Mars years at the time of this dissertation (Guzewich et al., 2017; Lemmon et al., 2015; Moore et al., 2016, 2018; Moores et al., 2015).

Figure 1.3 shows the column opacity at Meridiani Planum and Gale Crater, from the MER Opportunity and MSL Curiosity rovers, respectively. The column opacity shows a repeating pattern year-over-year where there exists a double peak in maximal opacities in the second half of the year, for the seven year record. Also note how the opacities at both sites track one another despite their different locations on the planet.

The record of column optical depth is beneficial to our overall understanding of martian atmospheric dust even though all three rovers are at separate locations. Having multiple monitoring stations over the planet allows the science and operations teams to coordinate observations. This is seen with the most recent global dust storm, in 2018 (MY34), which was initially observed by Opportunity (not shown in Figure 1.3), and allowed Curiosity to

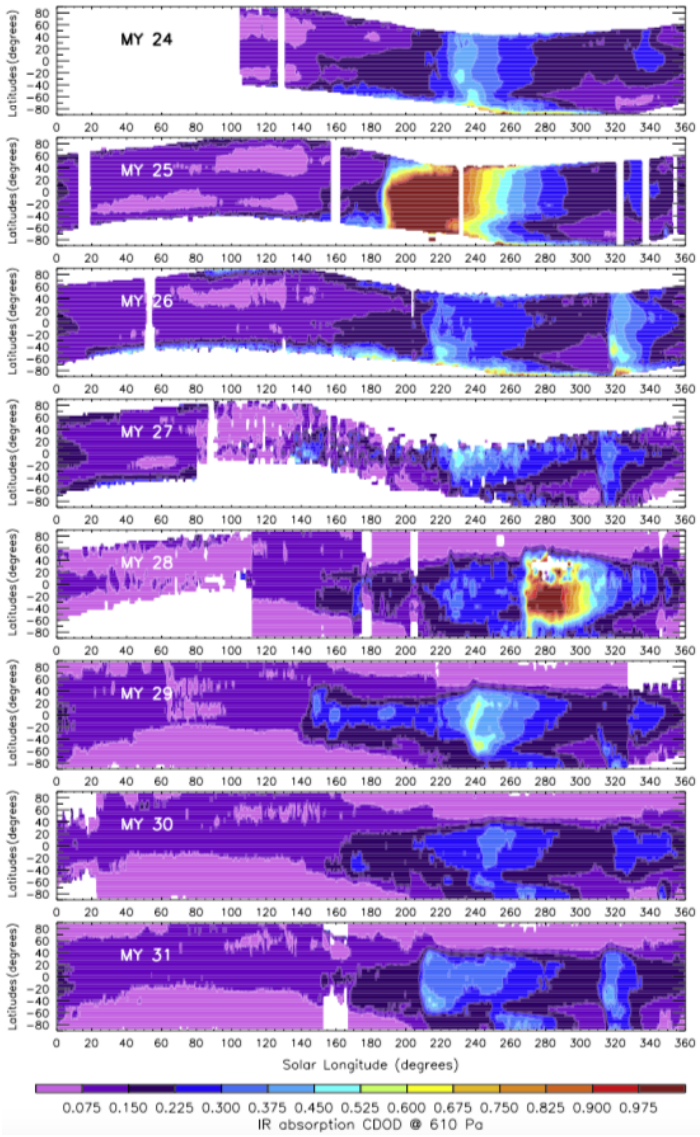

Figure 1.2: ***8 Mars Years of Column Optical Depth Maps***

Zonal means of 9.3 μm absorption column dust optical depth maps (normalized to 610 Pa) as a function of solar longitude and latitude for the eight available martian years. Data are extracted from the irregularly gridded maps obtained with the application of the iterative weighted binning procedure. Figure, caption and more information can be found in Montabone et al. (2015).

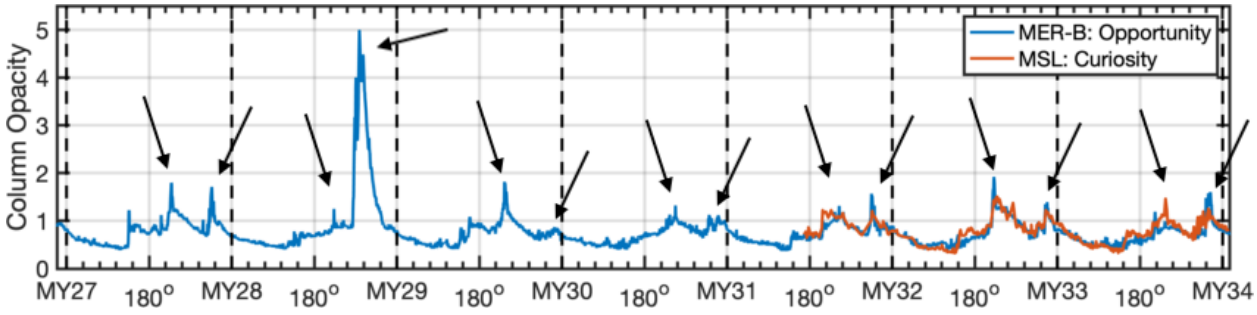

Figure 1.3: ***Column Opacity: Meridiani Planum and Gale Crater***

The column opacity for Meridiani Planum and Gale Crater as a function of solar longitude. The opacities are measured by solar disc imaging taken from the MER Opportunity and MSL Curiosity rovers respectively. The Opportunity data span over 7 Mars years, while the Curiosity data span 2.5 Mars years at the time of retrieval. Note the double peaked behavior of the column opacity in the later half of the Mars year. Data from Mark Lemmon at Texas A&M University(personal communication).

start its global dust storm protocol (Guzewich et al., 2018).

Comparisons can be made between these ground-truth measurements and orbital measurements (Guzewich et al. (2017) among others) that ultimately lead to the ability to convert opacity measurements of one type to another. Not only is this convenient, it allows a comparisons to be made between spacecraft which may not have had any overlapping measurements (as in Montabone et al. (2015)).

The distribution of dust within a few kilometers of the surface is missing from this long standing record of opacity measurements. Modeling of the thermal properties and hence the circulation for near-surface environments (Fonseca et al., 2018), can be improved by constraining amount of dust low in the martian atmosphere. Limb measurements are typically incapable of making reliable measurements within 1-2 scale heights from the surface due to the viewing geometry. The optical thickness along the slant path though the atmosphere increases dramatically at these lower elevations (Guzewich et al., 2017; Kleinböhl et al., 2015; Määttänen et al., 2013), which makes assessments of the vertical profile at these altitudes difficult. A ground based lidar is the best way to obtain the near-surface opacities, but one has not been flown to Mars since Phoenix (Whiteway et al., 2008), and no plans currently exist to send another.

This dissertation proposes a way to obtain near surface measurements of the opacity within Gale Crater, Mars, by using the Navigation Cameras (Navcam) on the MSL Curiosity rover (Moore et al., 2016, 2018; Moores et al., 2015).

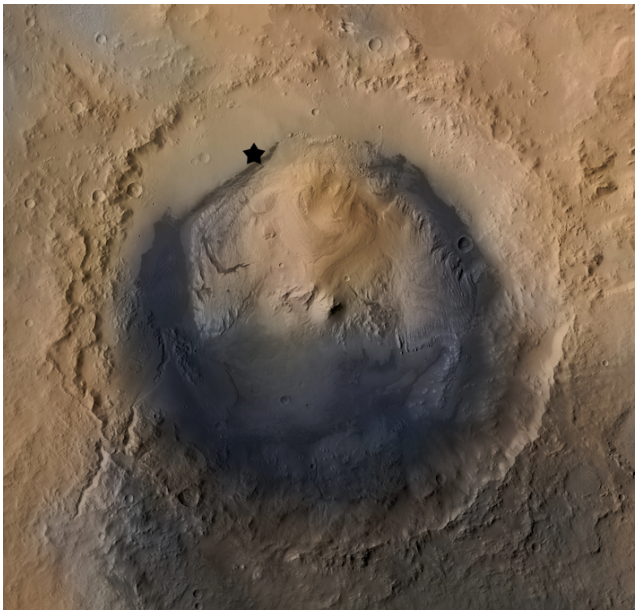

Figure 1.4: *Map of Gale Crater*

Gale Crater as seen from orbit. The image combines elevation data from the High Resolution Stereo Camera on the European Space Agency's Mars Express orbiter, image data from the Context Camera on NASA's Mars Reconnaissance Orbiter, and color information from Viking Orbiter imagery. North is up and the star represents the landing site of MSL. Image Credit: NASA/JPL-Caltech/ESA/DLR/FU Berlin/MSSS.

1.1.1 MSL and Gale Crater

MSL landed in the northern plains of Gale Crater (4.5895°S, 137.4417°E). Gale Crater is roughly 150 km in diameter and has a 5 km tall central peak (Vasavada et al., 2014), and is shown in Figure 1.4. It is located on the dichotomy boundary, in which the north plains of Gale Crater are lower in elevation than the south plains.

Atmospheric circulation within Gale Crater was examined prior to the arrival of MSL.

Leading to predictions of the effect the atmosphere would have on the Entry Decent and Landing phase of the spacecraft at Mars (Vasavada et al., 2012). This study also yields predictions (Haberle et al., 2012) of what the Rover Environmental Monitoring Station (REMS) instrument package would measure and a broad description of the circulation within Gale Crater, which predicts a suppression of the planetary boundary layer (PBL) to 1-2 km within versus 8-10 km outside the crater (Tyler and Barnes, 2013).

The modeled potential temperature profile of Gale Crater as predicted by the Mars Regional Atmospheric Modeling System (MRAMS; Rafkin et al. (2001)) is shown in Figure 1.5, which is reproduced from Moores et al. (2015).

The potential temperature is defined as the temperature at which a parcel of air at a pressure P could achieve if it were adiabatically brought to a reference pressure P_o. It is given by the equation:

$$\theta = T\left(\frac{P_o}{P}\right)^{R/c_p} \tag{1.1}$$

Where T is the temperature in Kelvin of the parcel, R is the gas constant, and c_p is the specific heat capacity at constant pressure.

Potential temperature is used as a proxy for the stability of an atmosphere. When the partial derivative with respect to altitude of the potential temperature is positive, the atmosphere is stable in that vertical motions are suppressed. When it is negative, the atmosphere is unstable to vertical motions, meaning convection is likely to occur.

A positive gradient of potential temperature with respect to altitude within northern Gale

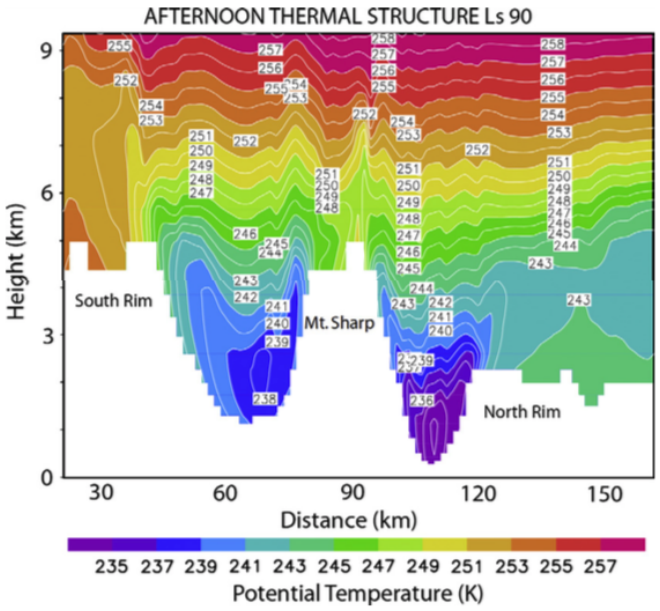

Figure 1.5: ***Modeled Potential Temperature of Gale Crater***

MRAMS modeling of potential temperature within and surrounding Gale Crater. The near zero gradient of potential temperature within the crater is suggestive of a suppressed convective layer within the crater, while outside the crater a negative gradient exists suggesting a large convective layer over the martian surface. Figure taken from Moores et al. (2015).

Crater is shown in Figure 1.5. This suggests that the atmosphere is stable and convection does not occur. If convection does not occur here, a vertical transport of dust cannot occur within Gale Crater during the timeframe modeled. However, the gradient of potential temperature with respect to altitude is negative for the first few kilometers above the surface outside the crater, to the north, indicating a convective layer.

To check the validity of these models, the suppressed PBL can be observed indirectly by

its influence on the production of dust lifting events. Dust devils are a byproduct of solar heating which cause vigorous convection at the surface of Mars (Rennó et al., 1998). This near surface convection can loft dust into the atmosphere, as observed previously with lidar (Komguem et al., 2013). A suppressed PBL would reduce the strength of convective mixing which results in fewer and/or less intense vortices compared to other similar locations on Mars (Kahanpää et al., 2016; Moores et al., 2015).

A Navcam observation was designed to capture dust devil activity, by taking a series of time-lapsed images. A dearth of dust devil activity in the northern plains of Gale Crater is observed (Moores et al., 2015) and validates the prediction of a shallow PBL, in comparison to the landing sites of Pathfinder, the MERs, and Phoenix, where dust devils were relatively common.

Recall Figure 1.3, in which the vertical column opacities at Meridiani and Gale Crater are similar. This is curious due to the fact that the MSL landing site is situated at a much lower elevation than Opportunity, -4.5 km versus -1.8 km (Squyres et al., 2004; Vasavada et al., 2014). One would expect to see a larger opacity if looking through a deeper atmosphere. If the near surface air within Gale Crater is relatively dust-free this similarity in opacity can be reconciled.

The dataset used to search for dust devils has since been repurposed to derive low lying opacities within Gale Crater, and is one of the topics covered in this dissertation, see Chapters 2 and 3.

1.1.1.1 Meteorology of Gale Crater

Since the landing of MSL in August 2012 there have been several studies into the meteorology local to Gale Crater. The Rover Environmental Monitoring Station (REMS) is an onboard meteorological station situated on the MSL rover. REMS hosts a suite of sensors developed to measure the pressure, ground and air temperature, wind speed and direction, relative humidity and the UV radiation environment local to the rover (Gómez-Elvira et al., 2014). Like the Mastcam column opacities, over a seasonal timeframe, all these measurements have a double peak to them.

For instance, take a look at the REMS pressure data presented by Ordonez-Etxeberria et al. (2019) and reproduced here in Figure 1.6. In this plot, the pressure is the purple shaded region, each vertical slice through the plot shows the diurnal pressure variations. Note yearly low pressure occurring just before $L_s = 180^\circ$ (southern winter) being sandwiched between two annual peaks in pressure occurring near $L_s = 60^\circ$ and $L_s = 270^\circ$. These peaks occur at different times than they show up in the column opacity and insolation data, but align very well with Mars' aphelion and perihelion timeframes, with the larger peak happening during the southern hemisphere's stronger summer ($L_s = 270^\circ$) compared to the other peak happening during the northern hemisphere's weaker summer ($L_s = 60^\circ$).

The REMS pressure sensor also detects convective vortices (Kahanpää et al., 2016), shown as dips in the pressure signal over a time period of a few tens of seconds, but there was little evidence for these vortices to contain any dust as the initial dust devil detection imaging sequences (Moores et al., 2015) did not show anything. This is evidence for a weak convective

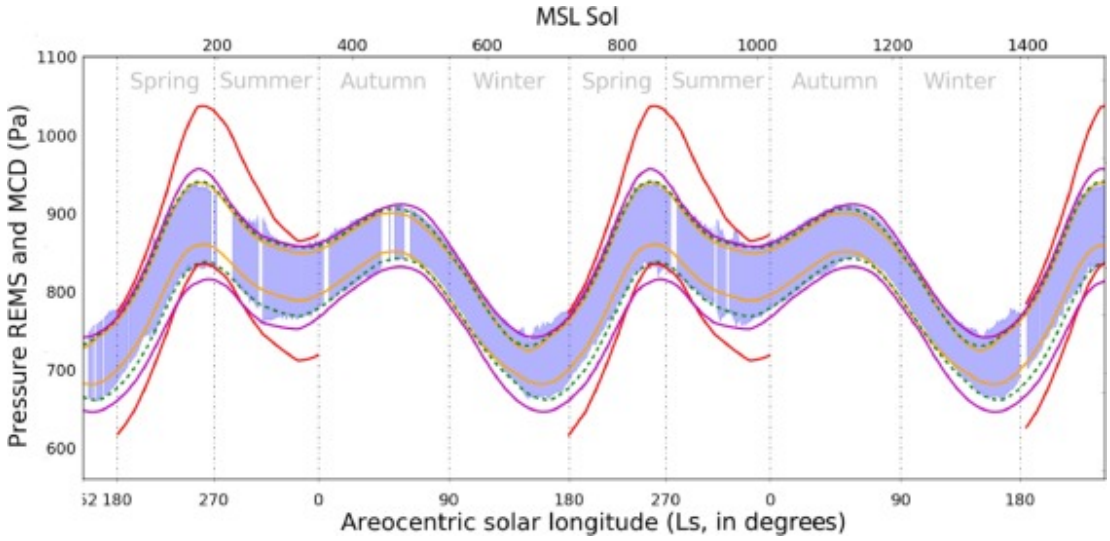

Figure 1.6: ***REMS Pressure at Gale Crater***

Daily pressure (purple shaded region) as measured at Gale Crater by the REMS instrument as a function of solar longitude for two Mars years starting from landing in mid MY31.

layer within Gale Crater limiting the vertical transport of dust into higher altitudes.

As of mission sol 1561 an upwards of 19 events ranging from dust devils to wind driven lateral dust transport have been observed within Gale Crater (Lemmon et al., 2017) in Navcam and Mastcam images. These were observed south of the rover towards Aeolis Mons and over the Bagnold dune fields. It is thought that these observations have more to do with local heating and stronger winds towards the south and not due to PBL mechanics.

Models (Rafkin et al., 2016; Tyler and Barnes, 2013) predict minimal convection within Gale Crater limiting the possibility of local lifting of dust to feed the atmosphere above. Local winds have been seen to actively transport dust and sand (Bridges and Ehlmann, 2018) but due to limited convection this transport is constrained to the lower atmosphere.

1.1.1.2 Radiation Environment at Gale Crater

The surface level UV radiation environment is being directly measured by the REMS UV Sensors. This is the first device sent to the surface of Mars to take in-situ measurements of this kind (Gómez-Elvira et al., 2014). These measurements are paramount in the characterization of aerosols in the atmosphere above Gale Crater (Smith et al., 2016) by allowing a measurement of the aerosol optical depth. Additionally, the REMS UV Sensor data is incorporated into radiative transfer codes to further refine modeling of the radiation environment at Mars, as seen in Moores et al. (2017), and discussed further in Chapter 7.

1.2 Martian Surface and Subsurface Interactions with Radiation

To extend our understanding of Mars' radiation field into the subsurface, we need to understand the materials that make up its surface. Specialized instruments on orbiters allow maps of the mineralogy of the surface of Mars to be produced(e.g. Seelos et al. (2014) and others). Furthermore, landed assets allow in-situ investigations into the surface composition local to the asset.

A collection of martian analogs is created through such investigations. One analysis, from Viking Lander 1 (VL-1) (Toulmin et al., 1977), lead Johnson Space Center (JSC) to development of one of the most commonly used martian regolith analogs, JSC Mars-1 (Allen et al., 1998).

JSC Mars-1 is composed of crushed up rocks from Pu'unene on the Island of Hawaii, and shares a similar reflectance spectrum, chemical composition, mineralogy, grain size, specific

gravity and magnetic properties to what was observed at VL-1 site (Allen et al., 1998). Over the decades numerous analogs have been created (Cloutis et al., 2015, for example) that mimic properties of martian regolith.

Rocks created during meteorite impact events can also be added as martian analogs as impact cratering is one of the few mechanisms that is confirmed to occur on both Earth and Mars, and as such, the geological end products should be similar (Napier and Clube, 1979). The temperatures and pressures at impact are high enough to melt the underlying bedrock; when this melt cools, microfractures and pore spaces develop (Cockell and Lee, 2002), which aide the transmission of radiation into their subsurface. The rock samples exhibit different shock stages, which relates to porosity, and is detailed in Table 1.1, which is reproduced from Pontefract et al. (2014).

These analogs are used to simulate the martian surface environment in Earth-based experimentation in lieu of requiring material from a Mars sample return mission.

Common to the studies that assess the transmission of radiation though these samples (Amaral et al., 2007; Cockell and Raven, 2004; Pontefract et al., 2014) is to exclude scattering. That is, these studies report the transmission perpendicular to the sample, without considering the portion that is scattered at angles off zenith through the sample. Thus, these papers confuse absorption, scattering, and extinction.

This dissertation, therefore, further aims to classify the transmission through martian regolith and rock analogs, as a function of scattering angle. This allows a better assessment of the radiation environment of the martian surface and subsurface by characterizing the

Shock Stage	Pressure Range (GPa)	Average Porosity (%)
0	–	0.5
1	2-5	n/a
2	5-10	1.0
3	10-30	1.5
4	30-35	10.5
5	35-55	18.5
6	55-60	44.0
7	60-80	63.0

Table 1.1: *Shock and Porosity of Impact Generated Rocks*

Classification of shock stages in impact generated gneisses based on petrographic analysis and observations from microscopic and confocal imaging and scanning electron micrographs. Table and caption reproduced from Pontefract et al. (2014).

way in which light propagates through various analogs, and has applications to the search for biosignatures on Mars.

1.3 Astrobiology

While NASA's Mars Exploration Program recently transitioned from a mindset of "follow the water" to the "search for biosignatures", astrobiology is not a new field. It is only now, however, becoming possible to search for evidence of biosignatures in-situ in the martian environment, forthcoming with the Mars2020 rover (Grant et al., 2018).

When sending spacecraft from Earth to Mars, contamination is near unavoidable. Some Earth microbes do make it to Mars (Benardini et al., 2014) despite measures being in place to limit the amount of contamination. However, studies (Moores et al., 2007; Schuerger et al., 2003) suggest that the harsh radiation environment of Mars would have likely sterilized any stowaways on timescales of a few martian days for Sun-exposed surfaces.

If, however, the search is for native extant (living) or extinct organisms, biosignature evidence likely exists in subsurface bedforms or endolithic environments (Cockell and Lee, 2002; Weiss et al., 2000). If such biosignatures exist, the question of whether or not life on both planets share a common evolutionary path remains purely hypothetical. However, making this assumption helps guide research in astrobiology. Astrobiology is aided by studying extremophiles (Cavicchioli, 2002; Pikuta et al., 2007), which are organisms on Earth that seem to defy the laws of nature by thriving in inhospitable terrestrial environments, by subjecting them to martian conditions (Gross, 2014).

Schuerger et al. (2003) reports that there have been several studies on microbial survival under simulated martian conditions such as Foster et al. (1978); Koike et al. (1996); Mancinelli and Klovstad (2000); Packer et al. (1963) among others. Microbial lifeforms tended to survive well under martian atmospheric conditions of low temperature, low pressure and a mix of N_2 and CO_2 atmospheres (Hagen et al., 1964; Hawrylewicz et al., 1962; Imshenetsky et al., 1973). However, only the martian UV environment is being assessed as a theoretical study in this dissertation.

Of the studies that simulated the martian UV radiation environment (Green et al., 1971; Koike et al., 1996; Mancinelli and Klovstad, 2000; Packer et al., 1963), a rapid onset of near total inactivation of the microbial cultures was noted. Mancinelli and Klovstad (2000) and Packer et al. (1963), show that thin layers of martian regolith analogs, such as JSC Mars-1 and *Fe*-montmorillonite, as well as a variety of earth soils, is sufficient to shield microorganisms from lethal dosages of UV irradiation.

Endoliths, on Earth, live in crack and pore spaces within rocks (Friedmann, 1980). These microorganisms get their energy from light penetrating the first few millimeters into the rocks surface (Walker and Pace, 2007). Endolithic lifeforms inhabit impact generated crystalline rocks, as these shocked gneisses provide moisture retention and protection from UV radiation (Cockell and Lee, 2002; Fike et al., 2002). These types of rocks are thought to exist in similarly created impact craters on Mars (Napier and Clube, 1979), and so warrant further study.

The studies mentioned above lack a proper accounting of the radiation environment of

Mars and how it varies by season and latitude, and gloss over the three dimensional scattering through geologic materials. This dissertation proposes a theoretical exercise that aims to find materials that may exist on Mars in which biosignatures may be preserved and microorganisms are protected. Assuming autotrophs, a successful material will block lethal dosages of UV radiation from penetrating the subsurface while allowing photosynthetically active radiation to be used as a source of energy. If such materials exist, this could help identify more probable locations and seasons in which signatures for extant or extinct microbial lifeforms may be detected.

1.4 How Do These Projects Fit Together?

A synergy exists between the three projects carried out in this body of work. We start by looking at the distribution of dust in the lower martian atmosphere, which adds to our knowledge of the radiation environment of the martian surface. Atmospheric science and geology overlap in aeolian processes, which, in the current era, are the most dominant mechanisms responsible for modifications to Mars' geomorphology (Fenton, 2003). As such, advances in our understanding in martian atmospheric dust and surface regolith have a profound impact on both fields. Characterizing the way in which light scatters through the martian surface can guide the search for biosignatures on Mars, the new frontier for Mars exploration.

1.5 Summary

This dissertation primarily focuses on radiative transfer in the martian environment – from interactions between light and atmospheric dust, to how light penetrates into the martian subsurface and the implications of both, ultimately answering these three questions:

1. By quantifying the dust content in the lower atmosphere, can the strange dynamics seen in numerical models of the planetary boundary layer be understood at Gale Crater?

2. How does the phase function of radiation change with respect to wavelength as it penetrates regolith and rock samples that are analogous to those seen on Mars?

3. Is it possible for niche environments to exist on Mars that could shield biosignatures and microorganisms from lethal dosages of UV radiation?

To put it in layman's terms, this dissertation aims to be a guide on how light interacts with atmospheric dust, piles of dirt, and of rocks on Mars, and to look at how Earth creatures may fair in the martian environment.

The first question above is answered by creating a mathematical approximation that relates the radiance values from observations to an opacity. The radiance values are obtained by a Mars-based radiometrically calibrated imager that points horizontally through the low-laying atmosphere within the interior of Gale Crater. The opacity is a proxy for the amount of suspended dust in the atmosphere between the rover and the distant crater rim. These observations and measurements are made on a regular basis and have been made for the majority of the ground phase of the mission.

The second question is answered through laboratory based experiments conducted within the Planetary Volatiles Laboratory, by myself and a handful of undergraduate researchers. A high powered light source is incident on regolith and rock samples and a mini-goniometer, fiber optically connected to a series of spectrometers, collects the transmission spectra. These spectra are calibrated, by myself, and the transmittance is assessed as a function of wavelength and phase angle.

The third question is a theoretical exercise I propose, using the data on transmission spectroscopy, discussed in this dissertation, as well as others research into terrestrial radioresistant extremophiles. Seasonal and longitudinal insolation values for Mars are obtained from a doubling and adding radiative transfer code (Moores et al., 2017). These values are then scaled by the appropriate attenuation seen in the laboratory experiments for various martian analogs. I then compare these values to the maximal dosages of UVA and UVB radioresistant extremophiles can withstand.

1.6 Following Chapters

Chapter 2 details the study of dust in the lower atmosphere of Gale Crater by introducing the instruments, the datasets, and the methodology. Chapter 3 gives the results of the in-situ investigation of the dust content within Gale Crater and ultimately provides interpretations for the odd atmospheric dynamics seen in numerical simulations. Chapter 4 introduces the experimental setup and methodology used to understand the propagation of light through regolith and rock samples. Chapters 5 and 6 provide the results and a discussion on how

light propagates in packed simulated martian regolith and within crystalline rock samples, respectively. Chapter 7 discusses the impact this experimental study may have on the search for subsurface and endolithic lifeforms on Mars. Chapter 8 concludes this dissertation. Chapter 9 details future research areas to build on these studies.

2 Investigation of Atmospheric Dust within Gale Crater, Mars

Global circulation models predict a suppressed planetary boundary layer (PBL) within Gale Crater (e.g. Tyler and Barnes (2013)). The typical depths of the PBL in these models are on the order of 2-4 km inside the crater, while in regions beyond the crater walls, the depths are the more typical 8-10 km seen elsewhere on Mars.

These prediction could be easily proved or disproved in-situ had the Mars Science Laboratory (MSL) been equipped with a lidar, as lidar data can be used to assess the vertical profile of dust and aerosols within the atmospheric column. This has been demonstrated on Earth (Collis and Russell, 1976; Kloos et al., 2018), as well as on Mars with the Phoenix mission from 2008 (Komguem et al., 2013).

MSL is, however, equipped with a camera that is designed to allow sun imaging without over-saturating the CCD. The Mastcam achieves this by placing a filter with five orders of neutral density in front of the CCD. The Mastcam is aptly named as it sits atop the Remote Sening Mast (RSM) of Curiosity and is one of the primary science cameras on the mission.

Early vertical column opacities derived from the Sun viewing Mastcam observations,

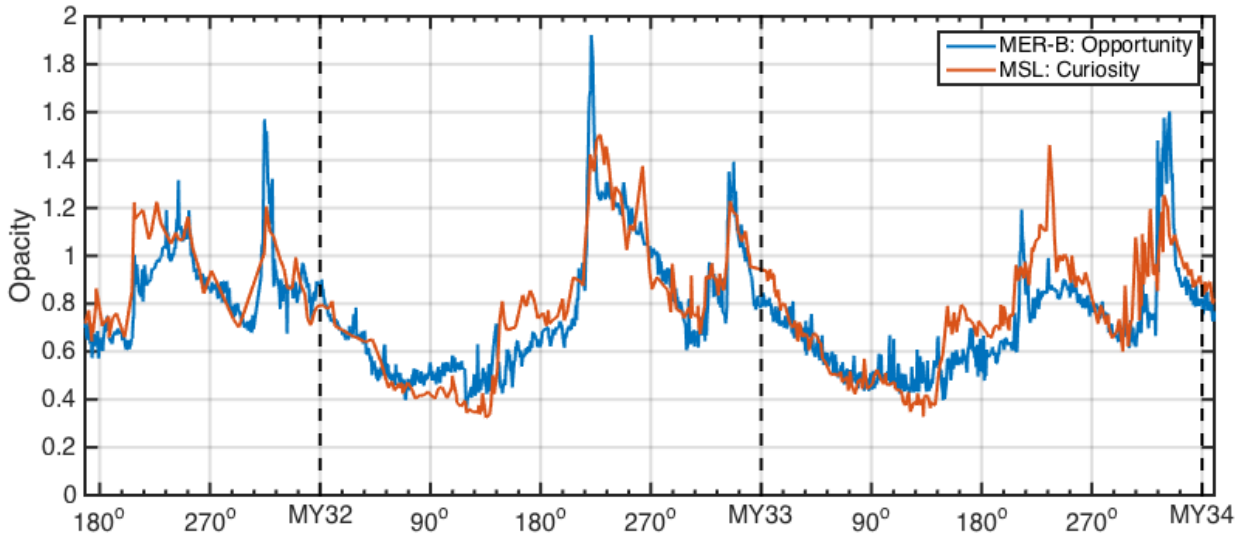

Figure 2.1: ***Column Opacity Record: Pancam + Mastcam***

Vertical column opacity derived from Pancam (MER-B: Opportunity; Meridiani Planum) and Mastcam (MSL: Curiosity: Gale Crater) Sun observations for the overlapping time period of MY32 $L_s = 168°$ and MY34 $L_s = 7°$. There are very subtle differences in the values despite a large disparity in the elevation of each rover. Data from Mark Lemmon (personal communication).

herein referred to as Mastcam Tau, indeed suggest that something unique is happening at Gale Crater (Moores et al., 2015). Mastcam Tau measurements suggest that the atmospheric column opacity over Gale Crater is remarkably similar to values derived from data from the Mars Exploration Rover (MER) Opportunity in Meridiani Planum, despite a difference of some 2.5 km in elevation between the two sites. Figure 2.1 displays the column opacity at Meridiani Planum and at Gale Crater for the overlapping duration of the missions up to MY34.

This similarity is puzzling. Not only do Mastcam Tau observations look through a deeper atmosphere than its MER counterpart, they look through a thicker atmosphere that, theoretically, should be capable of supporting a higher dust concentration, which would in turn increase the opacity of the atmosphere over Gale Crater.

This lead to the first investigation of the line-of-sight dust extinction (LOS-Ext) within Gale Crater (Moores et al., 2015) using radiometrically calibrated images from the Navigation Cameras (Navcam), also on-board Curiosity. It is easy to see the difference in high and low opacities within the line-of-sight of these images, as shown in Figure 2.2 that compares the same image sequence on different sols of the mission.

The primary findings of that study suggest that the atmosphere in the crater does exhibit a lower value of dust loading when compared to the near surface atmospheric column.

It is from Moores et al. (2015) that this body of work originates and has been detailed in Moore et al. (2016) which examines the seasonality of the line-of-sight dust extinction, and is discussed in this dissertation. Moore et al. (2018) further examines the geographical distribution of dust within northern Gale Crater, and is discussed in this dissertation. A similar methodology to that discussed in 2.2.1 has also been used to derive post-Entry, Decent, and Landing phase opacity measurements of the dust plumes that were raised using the Hazard Avoidance Cameras on MSL (Moores et al., 2016).

Figure 2.2: ***Low and High Opacity in the Line-of-Sight***

Images from Navcam depicting sols with a low (top) and high (bottom) line-of-sight opacity. The top image was taken on Sol 601 (MY 32, $L_s = 116.8°$) and the bottom image was taken on Sol 795 (MY 32, $L_s = 224.9°$) of the mission. Product IDs can be found in Appendix A.

2.1 Datasets

Two primary datasets are used in this study, namely images obtained by the Navcam to derive the LOS-Ext and the column opacity measurements derived by Mark Lemmon from the solar disc observations obtained by the Mastcam (Lemmon et al., 2015). Both sets of cameras are situated on the RSM on the Curiosity rover some 1.8 m above the crater floor. The images in Figure 2.3 are taken with the Mars Hand Lens Imager located on a retractable arm of Curiosity, the first image is provided to give context while the second image zooms in on the RSM to show configuration of Navcam (cyan) and Mastcam (white).

2.1.1 Navcam and Navcam Dataset

The Navcam has a spectral range of 600-800 nm, shown in Figure 2.4, and consists of a total of four cameras mounted on the mast of Curiosity. This system of cameras is comprised of two left-right pairs used for stereoscopic imaging, with each pair being connected to a separate computer system within the rover body. Each imager has a field-of-view of 45° in both the horizontal and vertical directions. A single image from Navcam has a maximum resolution of 1024 × 1024 pixels. For well exposed images, a 200:1 signal-to-noise ratio can be achieved. For the complete technical specifications of the engineering cameras produced for MSL, see Maki et al. (2012). For information on the performance of the MER-derived optics used in Navcam, see Maki et al. (2003).

The images used in this study are freely available in their raw form through NASA's Planetary Data System (McMahon, 1996), pds.nasa.gov. Radiometrically calibrated images

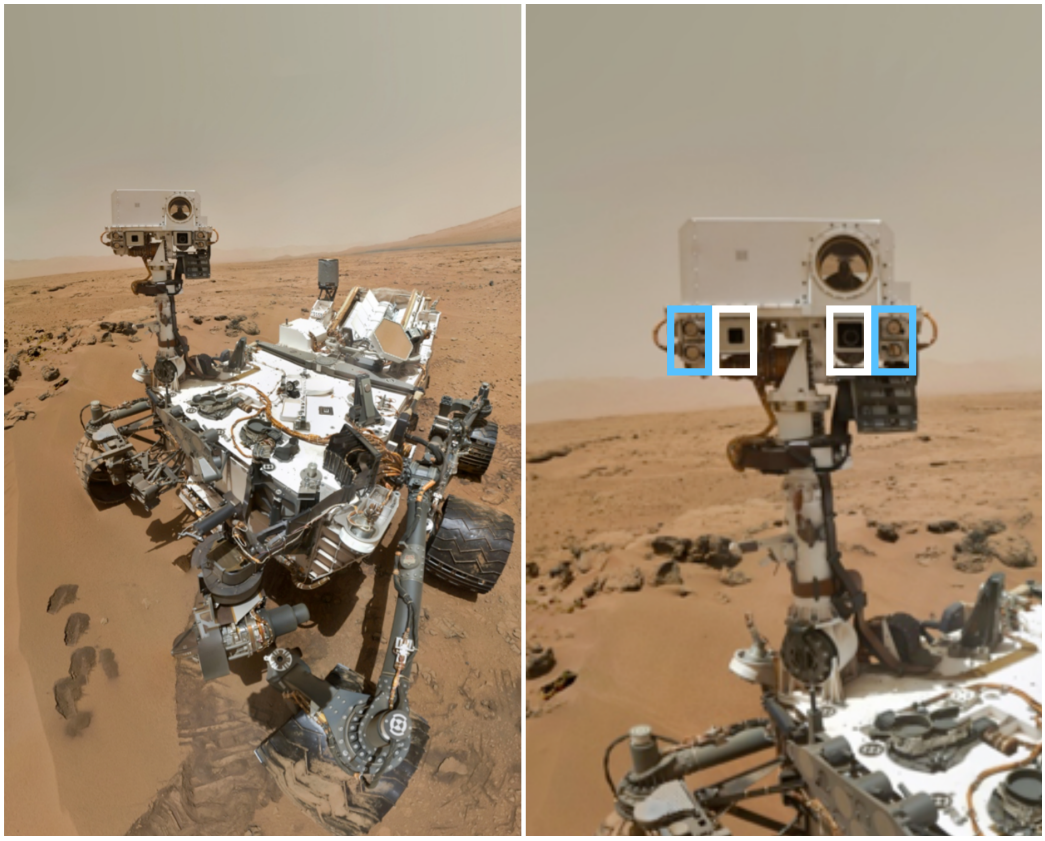

Figure 2.3: ***Curiosity Self-Portrait and Configuration of Navcam and Mastcam***

This image was taken by the Mars Hand Lens Imager mounted on Curiosity's retractable arm on Sol 84 (October 31, 2012). The left image is for context: MSL is roughly the size of a compact car, the RSM is some 1.7 m above the crater floor. The image to the right shows a close-up of the RSM, the Navcams are situated on the outer edges of the RSM (highlighted in cyan) while the Mastcam is more centrally located on the RSM (highlighted in white). NASA/MSSS PIA16239.

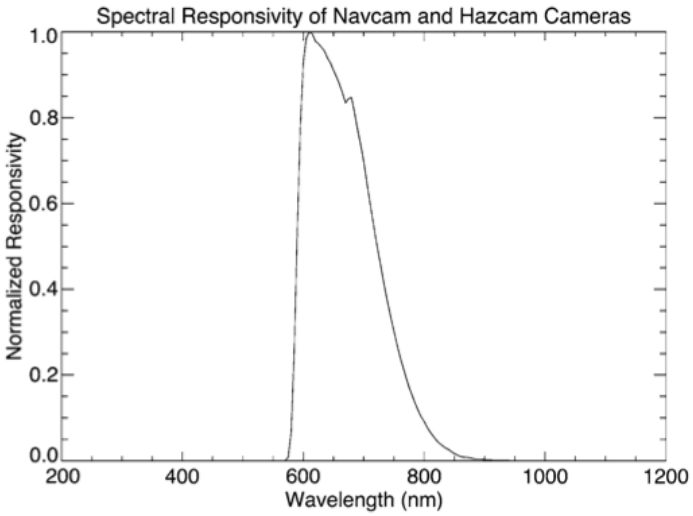

Figure 2.4: ***Navcam Spectral Responsivity***

Normalized, representative spectral responsivity for the Navcam and Hazcam cameras. The curve incorporates the spectral transmission properties of the optics, filters, and CCD QE. Figure and Caption taken from Maki et al. (2012).

were obtained through an internal file exchange accessible to MSL Science Team members. The dataset consists of two imaging sequences colloquially, and herein, referred to as the Dust Devil Search Movies (DDSM) and the North Crater Rim Extinction (NCRE) observations.

Both sequences are taken in a 2:1 aspect ratio (horizontal to vertical) and point in the northward direction slightly above the horizon. The requested azimuth and elevation of the Navcam are 0° and 5°, respectively, for these observations. The requested Navcam aspect ratio and pointing allows for the images to contain the near rover foreground, the distant crater rim, and the sky just above the crater rim, all important in determining the LOS-Ext as discussed in Section 2.2.1

The major differences between the DDSM and NCRE imaging sequences are the number of frames taken and the resulting image size. The DDSMs are comprised of four frames, with the Navcam being instructed to wait a set amount of time between each one, and are sub-framed to 1024 pixels in width and 512 pixels in height. Meanwhile, the NCREs are comprised of a single sub-framed 1024 $\times$ 512 pixel image, that is down sampled by 2:1, resulting in an image that is 512 pixels in width and 256 pixels in height. Figure 2.5 shows how the DDSM and NCRE images compare in size, and give a general idea of what these images look like.

The NCREs effectively replaced the DDSMs for these studies. This is done both to reduce data volume and to retire an observation that did not live up to its name. The DDSMs were initially designed to detect dust devil activity by compiling the frames into a movie. This proved to be ineffective as only one marginal detection has been made (Kahanpää et al.,

Figure 2.5: ***Image Comparison of DDSM and NCRE***

Both images taken with the Navcam. The image on the left is a frame from a DDSM from sol 635. The image on the right is a NCRE from sol 1661. Size has been preserved, the DDSMs are 1024 × 512 pixels while the NCREs are 512 × 256 pixels. Note the significant difference in dust loading as the crater rim is barely visible in the NCRE. Product IDs can be found in Appendix A.

2016; Moores et al., 2015) in the northern direction. Recently, however, numerous dust devils have been observed south of the rover towards Aeolis Mons with different Navcam sequences (Lemmon et al., 2017) effectively rendering the DDSM obsolete for dust devil observation. To continue the LOS-Ext record that began with the DDSMs, the NCRE was created.

The LOS-Ext dataset consists of 153 images from the DDSMs and 7 NCRE images taken between 1000 LTST and 1400 LTST, Local True Solar Time. The data span sols 100 to 1701, (MY31 $L_s = 208^\circ$ to MY34 $L_s = 7^\circ$), approximately 2.44 Mars years, sampling the LOS-Ext approximately once every ten sols. See Appendix A for a table of all image IDs used in this project.

2.1.2 Mastcam and Mastcam Dataset

The Mastcam is a scientific camera onboard Curiosity, composed a set of two fixed-focal length cameras: one medium angle (34-mm focal length; M34) and one narrow angle (100-mm focal length; M100). Each camera is affixed with its own filter wheel, in which the two have four shared bandpasses.

The Mascam Tau observation is a longstanding sequence that is used to derive the atmospheric column opacity. Typically this sequence runs at a minimum of once every few sols. During periods of increased dust activity the frequency increases and it is not atypical to have this sequence run multiple times during the sol. The sequence calls for the medium angle camera to observe the solar disc at 440 $\pm$ 10 nm and the narrow angle camera to

observe at 880 ± 10 nm, both observations are taken behind a neutral density filter with an opacity of 5. These images are processed similarly to those taken with the MER rovers, by Dr. Mark Lemmon at Texas A&M University. For full detail on how these images are processed to obtain a column opacity the reader is directed to Lemmon et al. (2015).

The opacities calculated at 880 nm are used in this body of work as this wavelength more closely resembles the Navcam bandpass. The opacity record derived by Mark Lemmon is shown in Figure 2.1 as a function of solar longitude for the time period of this study along with similar opacities seen at Meridiani Planum with the Pancam on MER Opportunity. This is the total opacity for all aerosols in the atmospheric column, atmospheric dust being the largest contributing factor to this opacity. A tiny fraction of the reported opacity may come from water-ice clouds, but this is considered negligible as Kloos et al. (2016) and Kloos et al. (2018) report that the opacities of water ice clouds over Gale Crater are on the order of 0.01.

Additionally, there exists a set of Mastcam Crater Rim Extinction (MCRE) observations that I briefly use to examine vertical and horizontal variations in the LOS-Ext and potentially measure the depth of the PBL within Gale Crater. The MCRE observations were a set of two RGB images with a resolution of 1200 × 1200-pixels. One image is taken with the M34 and one with the M100, both of which provided an impressive increase in spatial resolution. The field of view of the M34 and M100 imagers, 15° and 5.1°, respectively, are much narrower than Navcams 45° field-of-view (22.5° of which is standard for the DDSMs and NCREs). Figure 2.6 shows an example of the M34 and M100 MCRE observations for two sols with

Figure 2.6: ***Mastcam Images of Crater Rim***

Mastcam images of the crater rim on sols 994 and 1234 showing varying line-of-sight opacities within the crater. The images on the left are taken with the Mastcam 34. Images on the right are taken with the Mastcam 100. Product IDs can be found in Appendix A.

varying opacities in the LOS.

In Navcam DDSM observations, the crater rim is at most some 60 pixels tall. In comparison, the in the MCRE observations the crater rim has a height of 240-pixels and 600-pixels in the M34 and M100 respectively. Figure 2.7 nests the MCRE observations into a DDSM observation that was taken on the same sol. This diagram preserves the fields-of-view, with the M34 being more pixel dense than the Navcam, and the M100 being more pixel dense

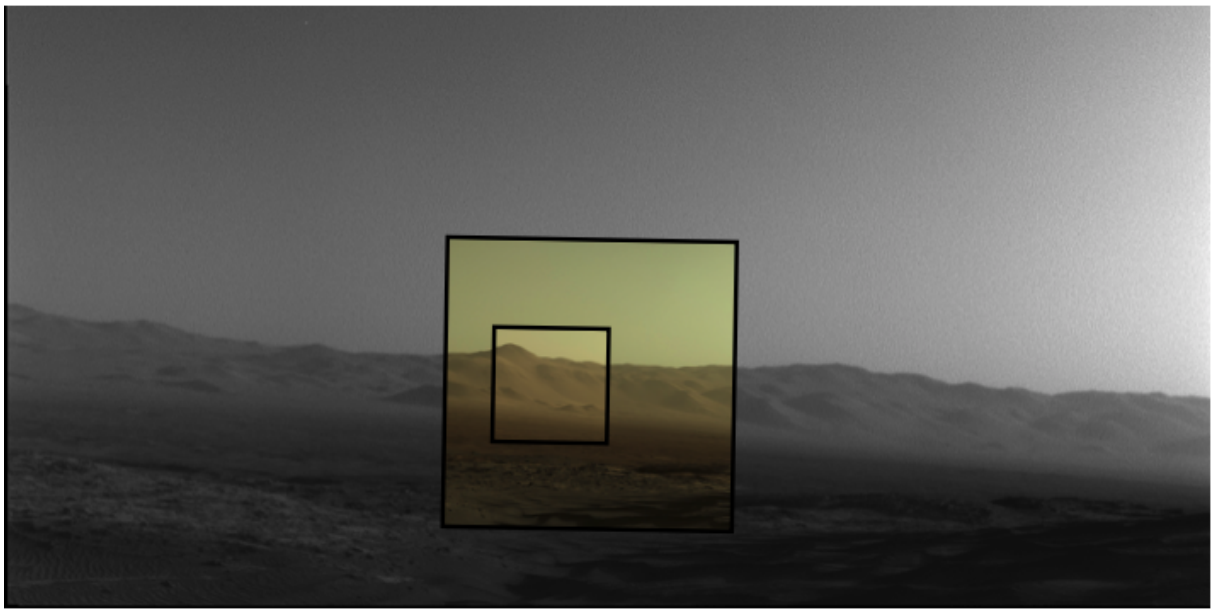

Figure 2.7: ***Nested Images of Crater Rim***

Mastcam 34 and Mastcam 100 images are overlaid on a Navcam DDSM image. The images were taken on Sol 1235, within a few minutes of one-another. The resolution of the Navcam image is 512 × 1024 pixels, while the resolution of both Mastcam images are 1200 × 1200. Product IDs can be found in Appendix A.

than the M34.

The MCREs also provide color information, allowing an assessment of the extinction at different wavelengths, something not available to the Navcam counterpart observations.

Only 12 MCRE observations are examined between sols 939 and 994 (MY 32 $L_s = 316$ – 347°). The observations were put on hold for a while and then resumed as a regular observation for the Environmental Science Theme Group on the MSL mission starting on sol 1187. My analysis of the data shows that the MCRE observations can be useful for further

research.

2.2 Methodology

The LOS-Ext can be calculated starting from the radiometrically calibrated images. Before getting into the physics and mathematics behind this derivation, it might help to have a simple model in mind.

The DDSM and NCRE images consist of three main parts: the foreground, the distant crater rim, and the sky above the crater rim. The foreground is at most a few tens of meters away from the rover, the crater rim is some 20+ km away from the rover, and the sky above the crater rim creates a near-infinite path through the atmosphere.

It does not require a stretch of the imagination to believe that the amount of dust suspended in the atmosphere between the rover and the foreground is negligible. Nor to believe that a near-infinite path through the atmosphere would imply seeing nothing but suspended dust. Details on the crater rim can still be made out, but they are a bit hazy, 20 km is a long path-length – so the amount of dust must not be negligible.

If we make the assumption that everything on Mars is coated in the same material (a fine layer of dust), and that material is lambertian (diffusively reflecting), then it would be fair to say that close up, one region would be indistinguishable from another. That is to say, we would expect a similar response from Navcam under the same lighting conditions. But if you add tens of kilometres of atmosphere between the two regions, then atmospheric dust becomes a part of the problem. However, if we know what response we are looking for

without dust (foreground) and we know what response we get with nothing but dust (sky), then we can infer how much dust must be in the line-of-sight to the crater rim.

The following section will describe how each component of the image fits into the numerical derivation of the line-of-sight opacity, following the derivation in Moores et al. (2015) using the notation of Hansen and Travis (1974).

2.2.1 Line-of-Sight Opacity

2.2.1.1 Radiance at Zero Optical Depth

As mentioned above, the distance between the Navcam and the foreground is a few tens of meters at most. The optical depth in this line-of-sight is indeed negligible, barring a global dust storm or a dust plume picked up by gusts of wind local to the rover. Thus radiance measured by the Navcam for the foreground regolith is observed at near-zero opacity.

It is then possible to use the radiance of the ground as a proxy for the radiance of the crater rim, if the opacity of the atmosphere between the rover and rim were near zero. Meaning:

$$I_R(\tau = 0) \approx I_F \tag{2.1}$$

Where I_R and I_F are the radiance of the crater rim and foreground, respectively. Note, we are suggesting that I_R is inherently a function of the opacity within the line-of-sight, and when that opacity is zero, the radiance of the crater rim would match that of the foreground.

This requires the assumptions that (a) the material covering the foreground is comparable to the material covering the crater rim and (b) that this material is sufficiently lambertian so

as the reflectance phase function is near-isotropic in that it changes by only a small amount at the varying observation angles of the foreground and crater rim.

2.2.1.2 Radiance of Dust in a Semi-Infinite Path

The radiance scattered by the dust can be derived from the radiance of the sky just above the crater rim. It is possible to calculate the scattered radiance strictly as a function of optical depth without knowledge of the precise scattering properties of the dust. It is possible to neglect secondary and tertiary aerosol particles, as the dust is the dominant source of scattering.

Letting n be the number density of dust particles with a scattering cross-section of σ_{sca} and a source function of J_D in the optical path, the light scattered in the direction of Navcam can be formulated as:

$$\mathrm{d}I_D(\vec{l}) = n\,\mathrm{d}l \int_{600nm}^{850nm} \sigma_{sca} J_D(\vec{l},\lambda)\,\mathrm{d}\lambda \tag{2.2}$$

where dI_D is the infinitesimal radiance added to the beam per path length $\mathrm{d}l$ towards Navcam. The limits on the integral correspond to Navcam's spectral range. If polarization is neglected, the source function of the dust in the direction of the rover, $J_D(\vec{l},\lambda)$, can be written as:

$$J_D(\vec{l},\lambda) = \frac{1}{4\pi} \int_{4\pi} I_o(\vec{d},\lambda) P(\theta_{l-d})\,\mathrm{d}\Omega_d \tag{2.3}$$

where I_o is the sum of direct and diffuse sources of radiation from all directions $\vec{d}$, and P is an arbitrary phase function of the scattered light from all directions that scatter towards the rover.

A number of assumptions can be made to simplify the expressions for the source function and, in turn, the cumulative radiance received by Navcam if we compare Equations 2.2 and 2.3 for a horizontal path (to the crater rim) and a path 3° above horizontal. Adding the superscript 'LOS' for the horizontal path and 'ACR' for the path above the crater rim and placing the formulation of the source function into Equation 2.2, we have:

$$\mathrm{d}I_D^{LOS}(\vec{l}) = \frac{n^{LOS}\,\mathrm{d}l}{4\pi}\int_{600nm}^{850nm}\int_{4\pi}\sigma_{sca}^{LOS}I_o^{LOS}(\vec{d},\lambda)P^{LOS}(\theta_{l-d})\,\mathrm{d}\Omega_d\,\mathrm{d}\lambda \tag{2.4}$$

and

$$\mathrm{d}I_D^{ACR}(\vec{l}) = \frac{n^{ACR}\,\mathrm{d}l}{4\pi}\int_{600nm}^{850nm}\int_{4\pi}\sigma_{sca}^{ACR}I_o^{ACR}(\vec{d},\lambda)P^{ACR}(\theta_{l-d})\,\mathrm{d}\Omega_d\,\mathrm{d}\lambda \tag{2.5}$$

If the dust particles are uniform in shape, size, and composition, the phase functions of the dust will be equivalent regardless of path. That is to say, $P^{LOS}(\theta_{l-d}) = P^{ARC}(\theta_{l-d}) = P(\theta_{l-d})$. Furthermore, the dust in both paths are illuminated similarly, e.g. $I_o^{LOS}(\vec{d},\lambda) = I_o^{ACR}(\vec{d},\lambda) = I_o(\vec{d},\lambda)$. Since the source function only depends on the incident radiation and phase function, which are independent of path, the source function is also equivalent regardless of path. Reducing Equation 2.4 and 2.5 to:

$$\mathrm{d}I_D^{LOS}(\vec{l}) = \frac{n^{LOS}\,\mathrm{d}l}{4\pi}\int_{600nm}^{850nm}\sigma_{sca}^{LOS}J_D(\vec{l},\lambda)\,\mathrm{d}\lambda \tag{2.6}$$

and

$$\mathrm{d}I_D^{ACR}(\vec{l}) = \frac{n^{ACR}\,\mathrm{d}l}{4\pi}\int_{600nm}^{850nm}\sigma_{sca}^{ACR}J_D(\vec{l},\lambda)\,\mathrm{d}\lambda \tag{2.7}$$

Additionally, assuming the scattering cross-section is proportional to the extinction cross-section over the wavelength range, implying a constant single scattering albedo, ω, recalling

that an element of optical depth is defined as: $\mathrm{d}\tau = n\sigma_{sca}\,\mathrm{d}l/\omega = n\sigma_{ext}\,\mathrm{d}l$, and taking the integrals with respect to wavelength and solid angle, yields:

$$\mathrm{d}I_D^{LOS}(\vec{l}) = \omega J_D\,\mathrm{d}\tau^{LOS} \tag{2.8}$$

and

$$\mathrm{d}I_D^{ACR}(\vec{l}) = \omega J_D\,\mathrm{d}\tau^{ACR} \tag{2.9}$$

Integrating along the path through the atmosphere will yield the total amount of light scattered in the direction of Navcam. However, since these path lengths are long and opacity exists between the scattering centers and the Navcam, it is to be expected that some of the scattered light is itself attenuated. Removing the superscripts, integrating, and remembering that some of the light will be attenuated leaves:

$$I_D = \omega J_D \int_0^{\tau_o} e^{-(\tau_o - \tau)}\,\mathrm{d}\tau \tag{2.10}$$

Where τ_o is the total opacity along the path. Completing the integration we can solve for ωJ_D:

$$I_D = \omega J_D[e^{\tau-\tau_o}]\Big|_0^{\tau_o} \tag{2.11}$$

$$I_D = \omega J_D[1 - e^{-\tau_o}] \tag{2.12}$$

$$\omega J_D = \frac{I_D}{[1 - e^{-\tau_o}]} \tag{2.13}$$

This formulation for the source function multiplied by the single scattering albedo, ωJ_D, converges to the observed radiance of the dust, I_D, as the opacity approaches infinity, i.e. as

$\tau_o \to \infty$. This is a direct result from the assumption that all locations along the path are uniformly illuminated.

We want to relate the source function to the radiance of the sky, I_S, which can be measured directly from the image when a path just over the crater rim is chosen. Using a measured optical depth, e.g. from Mastcam Tau, and assuming a constant extinction along the path just above the crater rim, τ_o can be estimated by taking into account the airmass, and ωJ_D can be calculated using Eq. 2.13.

In fact, the airmass, which is defined as the ratio between the path length in question to the zenith optical path length, provides another valuable approximation. Since we are already assuming a plane-parallel, homogeneous atmosphere, and the airmass is equivalent to the secant of the angle from zenith to just above the crater rim, and the record of column optical depth at Gale Crater, $\tau \geq 0.5$, all suggest that the radiance of the sky, I_S, would differ by approximately 0.3% from the source function multiplied by the single scattering albedo, ωJ_D. In practice, it is assumed that $\tau_o = \infty$ as a 0.3% error is negligible, and thus we have a formula for one part of the puzzle:

$$I_S = \omega J_D \tag{2.14}$$

It is now possible to create a relationship between the radiances of the three regions of the images and relate this to the optical depth along the line-of-sight.

2.2.1.3 Radiance through a Quasi-Dusty Atmosphere

The radiometrically calibrated Navcam images provide measurements of the radiance of the foreground, I_F, the sky, I_S, and the crater rim, I_R in units of Watts per square meter per steradian. With this information and the formalisms outlined above, it is possible to determine the amount of optical depth filling the atmosphere between the crater wall and Navcam. Assume the atmosphere between the crater wall and Navcam contains enough aerosol dust to produce an unknown optical depth, τ_o. The measured radiance value of the crater rim, I_R is a function of τ_o, that is to say: $I_R = I_R(\tau_o)$. The radiance of the rim can also be formulated as the sum of the radiance of the crater rim when viewed through zero optical depth attenuated by τ_o and the radiance provided by the atmospheric dust within the line-of-sight. That is to say:

$$I_R(\tau_o) = I_R(\tau = 0)e^{-\tau_o} + I_D^{LOS} \tag{2.15}$$

Using the radiance of the foreground as a proxy for the radiance of the crater rim with zero optical depth (Equation 2.1) and Equation 2.12 for the radiance of the dust yields:

$$I_R(\tau_o) = I_F e^{-\tau_o} + \omega J_D[1 - e^{-\tau_o}] \tag{2.16}$$

Equation 2.14 showed that the source function multiplied by the single scattering albedo is equal to the measured radiance of the sky, giving:

$$I_R(\tau) = I_F e^{-\tau} + I_S[1 - e^{-\tau}] \tag{2.17}$$

Rearranging and solving for the optical depth, τ, yields the analytical approximation for the opacity between the crater rim and the Navcam as:

$$\tau = -\ln \frac{I_R - I_S}{I_F - I_S} \tag{2.18}$$

The above expression has been validated for use on Mars by comparing it to radiative transfer simulations for a range of line-of-sight and column optical depths for near-noon, northward pointing observations. These simulations were run at Texas A&M University and agreed with the analytical expression to within 4%, with the analytical expression yielding a slightly lower opacity in the line-of-sight than the simulations (Moores et al., 2015).

2.2.2 Line-of-Sight and Column Averaged Extinction

The line-of-sight opacity and the column optical depth measurements cannot be compared to one another at this point. The optical depth in both the line-of-sight and atmospheric column are strongly dependent on path length. That is to say:

$$\tau = \int_0^l \sigma_{ext} \, \mathrm{d}l \tag{2.19}$$

Where τ is the opacity, σ_{ext} is the extinction coefficient, and l is the path length. The quantity we want to compare are the line-of-sight and column averaged extinction coefficients, σ_{ext}^{LOS} and σ_{ext}^{CA}, respectively. E.g.:

$$\sigma_{ext}^{LOS} = \frac{\tau_{LOS}}{l} = -\frac{1}{l} \ln \frac{I_R - I_S}{I_F - I_S} \tag{2.20}$$

and

$$\sigma_{ext}^{CA} = \frac{\tau_{CA}}{l} \tag{2.21}$$

To do this, it becomes necessary to make some assumptions about the path lengths both in the line-of-sight and in the atmospheric column.

2.2.2.1 Line-of-Sight Extinction

Both Moores et al. (2015) and Moore et al. (2016) treat the line-of-sight path length to be a static 30 km. Moores et al. (2015) had a reasonable argument to treat this path length as static, as the rover did not traverse any appreciable distance during the first 360 sols of the mission. Moore et al. (2016) used the same 30 km static line-of-sight distance for consistency, but in retrospect, it should have handled this a bit more carefully.

In Moore et al. (2018), a more rigorous approach to determine the distance between the rover and the crater rim was implemented. This new approach, detailed extensively in Appendix B, required the use of a digital elevation model (DEM) and rover positioning data. The DEM and rover positioning data allowed a derivation of the distance between the rover and the crater rim for every image in the dataset. This distance ranged from approximately 23.5 km on sol 100 to 27.5 km on sol 1701.

2.2.2.2 Column Averaged Extinction

Both Moores et al. (2015) and Moore et al. (2016) assume that the majority of the dust in the atmospheric column is within one scale height. One would expect most of the dust to be within the PBL, but with no direct measurements of the PBL within Gale Crater, we decided to link the dust scale height with the atmospheric scale height of a carbon dioxide

atmosphere.

Assuming uniform optical properties and density for the dust, if the dust-mixing ratio is constant with height, the dust will exponentially decrease with height in the same way the density would. A scale height of 10.7 km is calculated for an isothermal carbon dioxide atmosphere at 210 K. The density of the atmosphere in this model will exponentially decrease following $\rho(z) = \rho_o e^{-z/H}$. The column density of dust in this model decreases exponentially with height as well: $N(z) = N_o e^{-z/H}$. The total column optical depth can be written as

$$\tau_{CA} = \int_0^l \sigma N(z)\,\mathrm{d}z \tag{2.22}$$

where σ is the attenuation cross section of the dust (assumed constant) and $N(z)$ is the number density of the dust at a height z. Integration yields the optical depth through a column of height l.

$$\tau_{CA} = \frac{\sigma N_o}{H}[1 - e^{-l/H}] \tag{2.23}$$

The total opacity through a path length of one scale height would be $\tau_{CA} = \frac{\sigma N_o}{H}[1 - e^{-1}]$. As such, the average extinction seen through one scale height would be τ_{CA}/H. This height is thought of as a worst-case scenario, as previous studies on Mars using Lidar (Komguem et al., 2013) have shown that most of the dust observed was within the PBL. Thus, the reported column averaged extinction in Moores et al. (2015) and Moore et al. (2016) is considered a minimum value, as H is likely to be smaller than the 10.7 km modeled here.

In Moore et al. (2018) the column opacity was normalized by the height of the PBL as predicted by Global Circulation Models (GCM). Average peak PBL depths are derived from MarsWRF (Richardson et al., 2007; Toigo et al., 2012) and the values reported by Guzewich

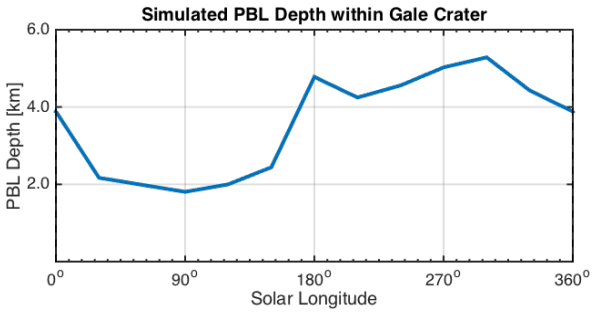

Figure 2.8: *MarsWRF PBL Depth*

MarsWRF predictions of the depth of the planetary boundary layer within Gale Crater as described in Newman et al. (2017). The values represent the diurnal peak PBL depth, typically between 1400 - 1600 LTST.

et al. (2017) were used. These are derived from the high spatial resolution 'B' grid MarsWRF simulation described by Newman et al. (2017) for increments of 30° in solar longitude and represent the diurnal peak PBL depth, typically between 1400 - 1600 LTST and reproduced in Figure 2.8. These values are similar to other GCM predictions of the PBL depth within Gale Crater (Fonseca et al., 2018).

2.2.2.3 MarsWRF PBL Depths

MarsWRF allows the option of inputing a preferred PBL parameterizing scheme or using the built in Medium Range Forecast PBL scheme as discussed in Richardson et al. (2007) adapted from Hong and Pan (1996) for use on Mars. The height of the PBL is determined iteratively using a mixed-layer diffusions model. A brief description is as follows.

The mixed layer diffusion model is described as Hong and Pan (1996):

$$K_{zm} = kw_s z\big(1 - \frac{z}{h}\big)^2 \tag{2.24}$$

Where K_{zm} is the momentum diffusivity coefficient, k is the von Karaman constant, z is the height above the surface, w_s is the mixed-layer velocity scale, and h is the depth of the PBL.

Satisfying boundary conditions for diffusion at heights $0.1h$ and h yield an expression for the height of the PBL in terms of the horizontal wind speed and potential tempreature at h, $U(h)$ and $\theta(h)$ respectively, the potential temperature of the lowest level, θ_a and the temperature of the surface, θ_s as:

$$h = Rib_{cr}\frac{\theta_a|U(h)^2|}{g(\theta(h) - \theta_s)} \tag{2.25}$$

Where Rib_{cr} is the critical bulk Richardson number, a dimensionless number that is the ratio to the buoyancy and flow shear, and g is the gravitational acceleration, 3.72 m s^{-2} on Mars.

Initially the height, h is approximated by taking a guess at the surface temperature, θ_s, as being the potential temperature of the lowest level. This yields estimates of the mixed layer velocity which in turn allows a better approximation of the surface temperature. This process is iterative and improves the final determination of h.

The method above has also been adapted for use on Titan (Richardson et al., 2007). For the full derivation see Hong and Pan (1996).

2.3 Implementations of LOS-Ext Analytical Expression

This dissertation extends the record of LOS-Ext within Gale Crater through sol 1701 and examines the dataset for seasonality and variability in both the vertical profile and horizontal expanse of the northern plains of Gale Crater. This section describes four algorithms in which the LOS-Ext analytical expression (Equation 2.20) is applied to derive: 1) a mean-valued LOS-Ext for each image, 2) a geographically constrained LOS-Ext value, 3) a LOS-Ext value for numerous sub-divisions along the horizontal swath of the crater rim, and 4) a mean-valued vertical profile of LOS-Ext values within the crater.

The four applications differ mainly in the size of the patch used on the crater rim. In all cases, the mean radiance value of the area in question is used and the width of the foreground and sky patches correspond to the width of the patches along the crater rim. This is done to alleviate any effects due to observation geometry. In all applications, the line-of-sight distance used corresponds to the mean distance for the patch on the crater rim.

1. Mean-Valued LOS-Ext

   This algorithm assesses a 16-pixel tall region, roughly three-quarters the way up the crater rim. The width of the patch used is ideally the width of the image at 1024-pixels, but some images needed adjustment as this region may have been obscured by foreground objects and geological features.

2. Geographically Constrained LOS-Ext

   This algorithm assesses a 16-pixel tall region, roughly three-quarters the way up

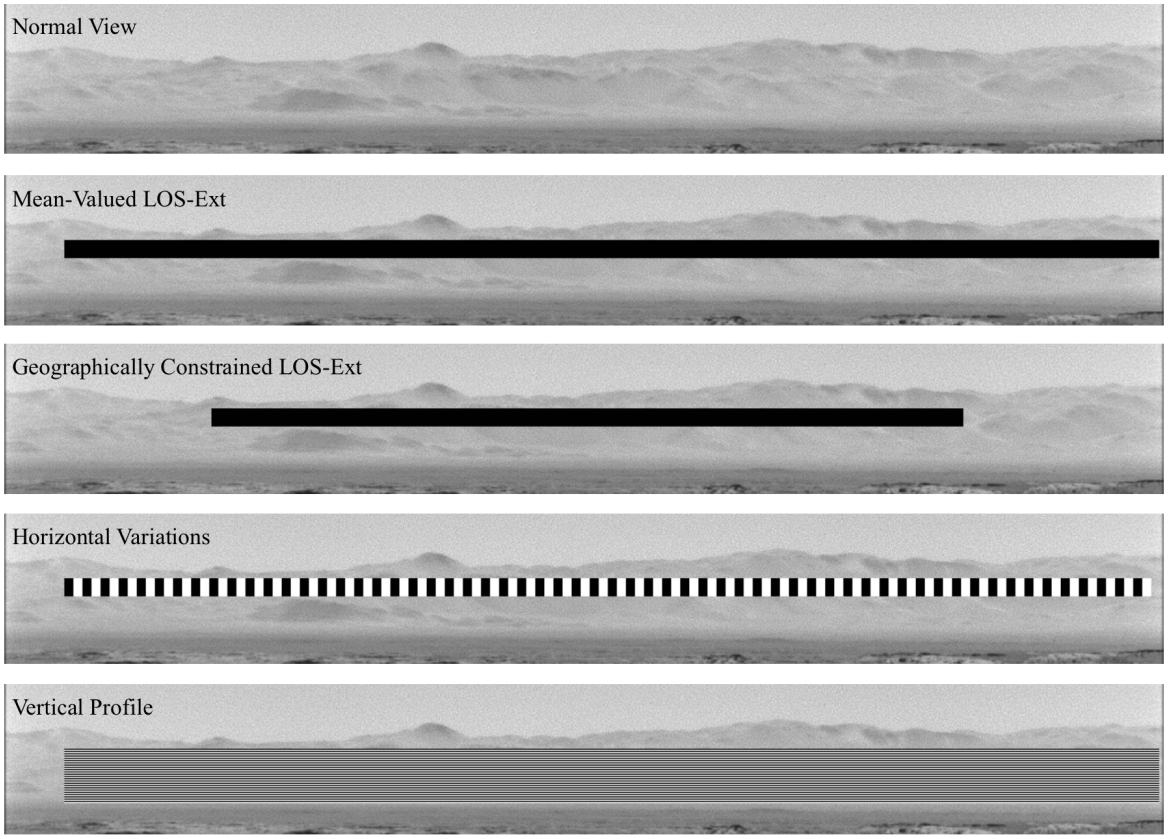

Figure 2.9: ***Areas of Interest on the Crater Rim***

The black and white regions are the locations on the crater rim that the radiance values are averaged over. Normal View: Cropped DDSM taken on sol 635 for context. Mean-Valued LOS-Ext : This produces one value per image. The full width is not used due to variations in distance to the west. Geographically Constrained LOS-Ext : This produces one value per image. The black region is 664-pixels wide and is a common portion of the crater rim in the majority of observations. Horizontal Variations: Gives multiple values for each block along the crater rim that are used to look for temporal variations in different regions. Vertical Profile: Each region is one pixel tall, this creates a profile of the dust within the crater, that is then used to look for temporal variations. The product ID can be found in Appendix A.

the crater rim, it differs from the Mean-Valued algorithm in that it isolates a specific 664-pixel wide region on the crater rim common in most images. The size was chosen to maximize the number of images containing the region, as well as provide a statistically significant portion of the crater rim to average over.

3. Horizontal Variations

   This algorithm assesses a 16-pixel tall region, roughly three-quarters the way up the crater rim, it differs from the Mean-Valued and Geographically Constrained algorithms in that it breaks the image into as many 16×8 pixel blocks along the crater rim. This produces a horizontal profile to assess for geographical variations in the LOS-Ext.

4. Vertical Profile

   This algorithm creates a vertical profile, consisting of the middle 48-pixels of the crater rim. Each patch making up the vertical profile is one-pixel in height and as wide as allowed, following the same constraints as the Mean-Valued algorithm. These values are then scaled, as if the dust profile should fall off with altitude in the same way as pressure would.

A visual representation of the regions along the crater rim that are used can be found in Figure 2.9 in which the portion of the rim used has been converted to black or white.

2.4 Sources of Error

The radiometrically calibrated images are assumed to be perfect. However, the radiance received by Navcam is dependent on a number of variables, illumination being just one of them. Illumination effects, such as shadows, can affect how much light is received by the Navcam. As such, the dataset is restricted to images obtained in a four-hour window centered around local noon. This restriction in solar elevation reduces sources of error from shadowing on the crater rim. This is inferred by near identical standard deviations of the radiance values for the patch on the crater rim and that of the sky above.

Systematic uncertainties arise in our assumption that the material making up the surface is sufficiently lambertian, that is, it reflects light similarly at all scattering angles. The observation angle between the foreground and the distant crater rim differ by only a few degrees. Reflectance values for JSC Mars-1, a martian regolith, from Johnson et al. (2006) suggest deviations in the phase function on order of 10% for the viewing geometries of the Navcam dataset. A change of 10% in the radiance values for the foreground accounts for a change in the derived LOS-Ext up to 20%. An additional uncertainty that arises in derivation of the LOS-Ext comes from the assumption that the material in the foreground is representative of the material making up the crater rim. This assumption is likely the largest source of error in the derivation of LOS-Ext arises due to the variegated terrain local to the rover. As the rover changes locations, the foreground is not consistent between each location. Over the dataset, the mean radiance values of the foreground are seen to range from 1500 - 4000 W m^{-2} sr^{-1} and the mean radiance values for the sky and crater rim are

seen to only range from 4000 - 6000 W m^{-2} sr^{-1}. The large variation in the foreground radiances introduce large uncertainties into the derivation of LOS-Ext , likely on the order of 50%.

It is worth noting that the Mean-Valued LOS-Ext and the Geographically Constrained LOS-Ext algorithms were run to understand if there were significant differences between the two methods. While the Geographically Constrained method gives a more robust determination of the LOS-Ext in a specific direction within Gale Crater, it also reduces the dataset by some 20%. Since the differences in values between the two methods was less than the systematic uncertainties mentioned above, it was deemed that the Mean-Valued LOS-Ext should be used in favor over the Geographically Constrained LOS-Ext method to include more data points in the LOS-Ext dataset.

A 95% confidence interval is derived for each image by measuring the LOS-Ext for multiple regions on the crater rim. The crater rim is divided into n distinct 8-pixel wide by 16-pixel tall regions and the radiance of the foreground and sky come from the same horizontal pixel numbers. The size of the region is chosen to optimally negate effects due to image compression while still allowing a significant number of measurements, $n > 80$, within each image. The LOS-Ext is determined for the n regions and the intervals are determined by: $CI = 1.96\sigma/\sqrt{n}$, where σ is the standard deviation of the LOS-Ext values for each image.

3 Line-of-Sight Extinction within Gale Crater, Mars: Results and Analysis

This chapter discusses the results of the LOS-Ext record within Gale Crater, Mars from sol 100 - 1701, and offer some insights into what can be inferred from this study, specifically whether or not the analysis of the LOS-Ext can test the hypothesis of early modeling that suggests a suppressed planetary boundary layer within Gale Crater.

3.1 Seasonality

Year-over-year the LOS-Ext values appear to track one another quite well, as seen in Figure 3.1, which shows the Mean-Valued LOS-Ext with their uncertainty estimates time-folded over one Mars year.

A seasonal patterns is observed for the entire dataset with minimal LOS-Ext in the first half of the year and maximal values occurring in the second half of the year. For the two full Mars years in which data has been collected, MY32 and MY33, annual minimum and maximum LOS-Ext values occur near $L_s = 90°$ and $L_s = 300°$, respectively. Between $L_s = 90 – 300°$ the trend for LOS-Ext is to increase, while the trend between $L_s = 300 – 90°$ from

one Mars Year to another is a decreasing one.

It appears that a trend of slightly higher valued LOS-Ext exists as time progresses. The values derived for MY33 are typically larger than those for MY32 and values derived for MY32 are typically larger than those for MY31. This interannual variability suggests that while the LOS-Ext values indeed follow seasonal trends, the values themselves will differ for the same solar longitude for different Mars years.

Significant differences in LOS-Ext are seen between MY32 and MY33 during the L_s = 0 – 180° seasons. During these seasons, the values between the two years fall outside of the error estimates of each individual observation. Since large sol-to-sol variations in the LOS-Ext are not seen in the data, it can be suggested that within Gale Crater, MY33 was statistically slightly dustier during the southern winter than it was in MY32.

Outside of this timeframe, e.g. during the L_s = 180 – 360° seasons, again differences in LOS-Ext are seen with the LOS-Ext values for MY33 being slightly elevated compared to those for MY32. However, in this instance the differences are within the margin of error and may not be as significant.

These trends do not correlate with the interannual variability in the Mastcam column opacity measurements for MY32 and MY33 as seen in Figure 3.2, or those seen at the MER locations (Lemmon et al., 2015; Montabone et al., 2015). The column opacity measurements are typically double peaked in the later half of the year around $L_s = 240°$ and $L_s = 320°$ with a seasonal low around $L_s = 120°$.

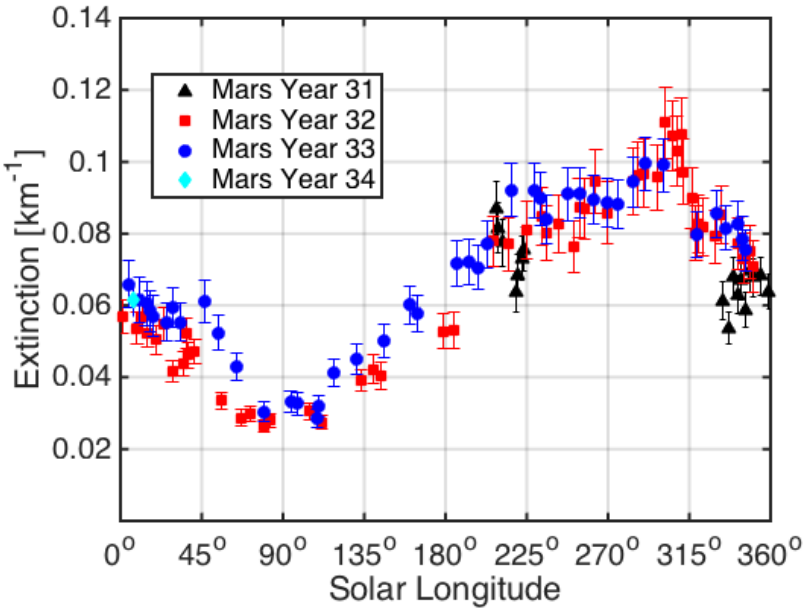

Figure 3.1: ***LOS-Ext and Uncertainties as a Function of Solar Longitude***

Mean-Valued LOS-Ext as a function of solar longitude. The data have been time-folded to show how well the LOS-Ext values track one another year-over-year. The data begins on sol 100, MY 31 $L_s = 208°$, and ends on sol 1701, MY34 $L_s = 7°$. Black triangles represent the LOS-Ext for MY31, red squares for MY32, blue circles for MY33, and cyan diamonds for MY34. Seasonally low LOS-Ext (less dust) occurs near $L_s = 90°$ and seasonally high LOS-Ext (more dust) occur between $L_s = 270 - 315°$.

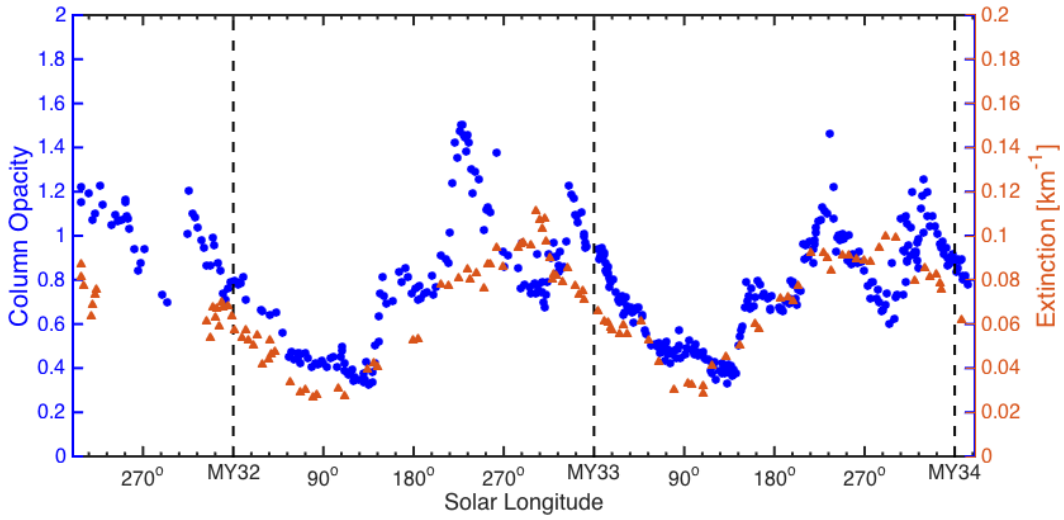

Figure 3.2: ***Column Opacity and LOS-Ext as a Function of Solar Longitude***

Mastcam Tau vertical column opacities and Mean-Valued LOS-Ext as a function of solar longitude. The blue circles represent the column opacity (left vertical axis). The orange triangles represent the LOS-Ext (right vertical axis). Column opacity is double peaked in the later half of the year, whilst the LOS-Ext is singly peaked and offset from the Mastcam Tau Peaks.

3.2 Horizontal (Geographic) Variations

Implementing the Horizonatal Variations version of the algorithm, the LOS-Ext for 16 × 8-pixel blocks across each observation can be assessed to look for changes in LOS-Ext across the crater rim, the results are shown in Figure 3.3. The data in Figure 3.3A is interpolated to fill in the temporal gaps and is presented as Figure 3.3B. On average, cooler colors, indicating lower LOS-Ext values, are seen between $L_s = 0 - 180°$ implying high visibility during southern autumn and winter; on average, warmer colors, indicating higher LOS-Ext values, are seen between $L_s = 180 - 360°$ implying low visibility during southern spring and summer.

It is worth noting that as time progresses, the changes in LOS-Ext across the crater rim appear to change as one. That is, the colors tend to get brighter and darker, indicating increases and decreases in LOS-Ext, as one. This can be seen in the non-interpolated data in Figure 3.3A, which is suggestive of minimal lateral transport of dust. Transport would present itself as a spreading out of higher valued LOS-Ext from a singular point. These differences in LOS-Ext across the crater rim are likely due to features on the crater rim itself affecting the illuminating conditions, and not due to varying dust loads across the image. As such, it can be said that the dust suspended within the crater is indeed well-mixed horizontally and the source for this dust is likely sedimentation from the over lying air masses.

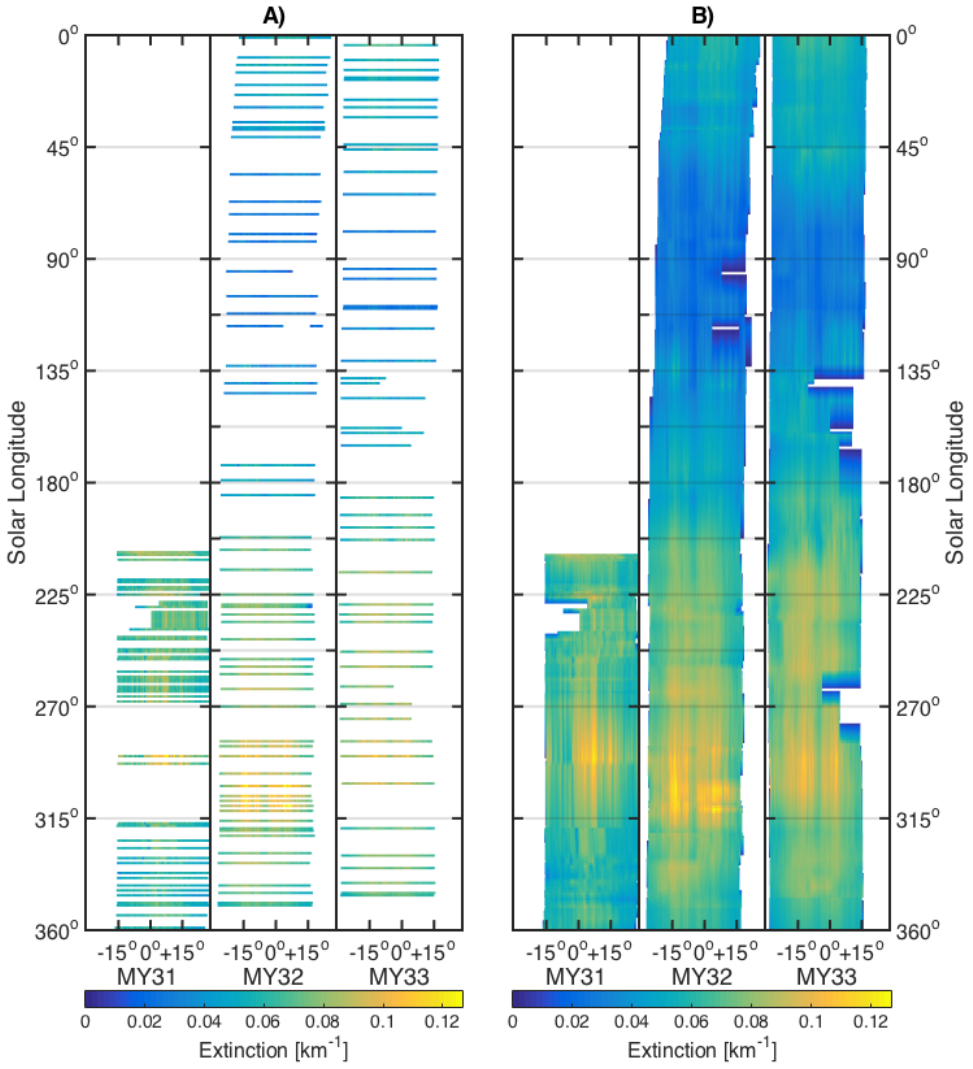

Figure 3.3: ***Horizontal Variations in LOS-Ext***

LOS-Ext values versus relative location on the crater rim for the period of the observations covering 2.44 MY. The LOS-Ext value is displayed with the color axis. The horizontal axis are degrees from north, with north being 0°. Time is conveyed on the y-axis and reads top to bottom. The three frames represent the 3 different Mars years this data spans: MY31 on the left, MY32 in the middle and MY33 on the right. A) Shows only the data for the images used in this study. B) Interpolates the data in A) to fill in temporal gaps.

3.3 Vertical Variations

Implementing the Vertical Profile version of the algorithm generates LOS-Ext values with height within the crater. These profiles are shown in Figure 3.4A for the images in the dataset and Figure 3.4B interpolates the data to fill in the temporal gaps, much like was done in 3.3B.

It is possible to see some vertical structure in the raw data alone in Figure 3.3A, but interpolating over the un-sampled times provides a better visualization and is displayed in Figure 3.4B. Interpolation is a good-enough approximation as to what would be seen within Gale Crater if the frequency of observations increased to a per sol basis as the LOS-Ext appears to be more predictable than the column opacity on sol-to-sol timescales.

Notice in Figure 3.4B that for nearly the entire dataset the LOS-Ext values are maximal at minimal altitude and have a slight gradient of decreasing LOS-Ext with increased altitude. This makes sense as the atmosphere is the thickest at the lowest altitudes, thus a greater capacity to suspend dust at these lower altitudes.

One of the most interesting take-aways from this plot is that the dusty season in MY32 is bookended by a point in time where the LOS-Ext is seasonally low at low altitudes, $L_s = 200°$, and a point in time where the LOS-Ext is seasonally high at low altitudes, $L_s = 300°$. This warrants further investigation as the same phenomena dose not occur in MY33 on the same magnitude as only a small inversion is seen in MY33 at $L_s = 215°$. This inversion is suggestive of dust being uplifted from the crater floor and thrown to higher altitudes during the most convective time of day.

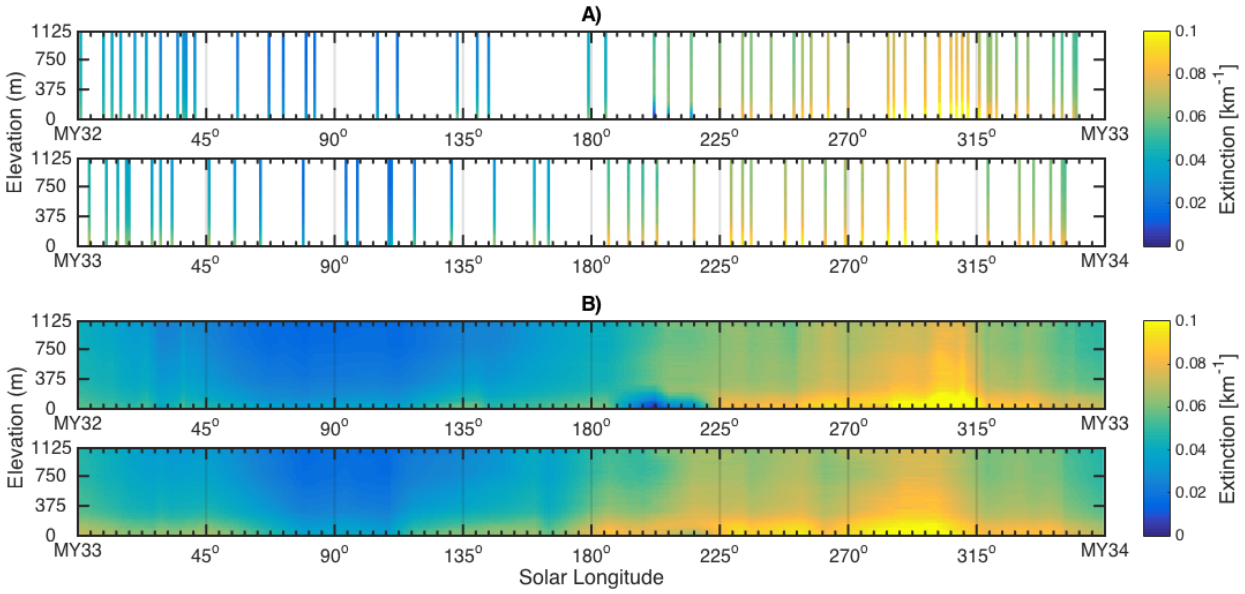

Figure 3.4: ***Vertical Profile of LOS-Ext***

Vertical distribution of LOS-Ext values as a function of solar longitude for MY32 and MY33. The LOS-Ext value is represented with the color axis, while vertical location on the crater rim is displayed on the y-axis, in meters relative to the crater floor. A) Shows only the data for the images used in this study. B) Interpolates the data in A) to fill in temporal gaps. MY31 was excluded from this analysis due to very few images showing the entire vertical expanse of the distant crater rim.

3.4 Geographic Heterogeneity in Line-of-Sight Extinction

This work aims to remove the geographic variability from the LOS-Ext dataset by rectifying the images to one another to preserve the geography of the crater rim. Initially, it was thought that variations in the LOS-Ext in a single image would reveal regions in which dust enters and/or leaves the crater. Such locations would have been identified on the plots of Figure 3.3 as a horizontally spreading of warmer or cooler colors indicating dust entering or leaving the crater, respectively. However, this horizontal movement is not apparent in the dataset and would tend to support the hypothesis that the dust in the northern part of the crater is well mixed and is injected into the crater from above. The variations that remain, horizontally, instead likely mark changes in reflectance from one spot to another on the crater rim. This is more easily seen in Figure 3.3B where interpolation is used to obtain approximate LOS-Ext values for times in which data is missing.

The same geographic location on the crater rim separated in time should not exhibit seasonal reflectance differences, however, they tend to reproduce statistically similar normalized extinction values. This suggests that the horizontal variations in LOS-Ext are due to the features on the crater rim itself. This is further supported by the fact that two regions near each other on the crater rim can vary in LOS-Ext by an order of 50% when comparing a fully illuminated and fully shadowed section of the crater rim.

It might be possible to resolve this issue by mapping the reflectance along the crater rim on a dust free sol and normalize each image to this map, but it would be difficult as different sunlight geometries have the potential to vary sub-pixel shadows on the crater rim. Further

investigation is needed to resolve this issue, and at the moment it is being left as for future study.

Moreover, the method to derive the LOS-Ext relies on similar reflectance values between the foreground and the crater rim, a situation that cannot always be a reality due to the variety of terrains that enter the foreground, effectively varying the radiance measured for the foreground in nearly every image. To minimize these differences, a large portion of the foreground is selected as a representative to obtain a mean radiance.

As such, the horizontal variations in LOS-Ext are not considered to be variations in the dust loading of the atmosphere within the crater, but instead due to the physical differences of the crater rim.

3.5 Comparisons to Mastcam Tau

It would be ideal to compare the LOS-Ext to the lower altitude extinction seen with a lidar system, but one does not exist on MSL. As such, the total atmospheric column opacity at Gale Crater is used as a proxy for the average extinction in the atmosphere above the rover. The column opacity is obtained from the Mastcam Tau observation at 880 nm. The opacity values at Gale Crater are similar to those reported for the Mars Exploration Rover Opportunity at Meridiani Planum (Lemmon et al., 2015) which was shown in Figure 1.3.

Both Opportunity and Curiosity are located at semi-equatorial latitudes. Opportunity is situated in the northern hemisphere near Eagle crater on Meridiani Planum (1.9° N, 354.5° E) (Squyres et al., 2004), meanwhile, Curiosity is located in the southern hemisphere in the

north west planes of Gale Crater (4.6° S, 137.4° E) (Vasavada et al., 2014). The equatorial region of Mars broadly defines the dichotomy boundary, a global feature from an ancient massive impact that created the northern lowlands and southern highlands (Andrews-Hanna et al., 2008). Opportunity is located in the northern hemisphere, so one might anticipate that its elevation is lower than Curiosity, which is located in the southern hemisphere. This is not the case however, the elevation of Opportunity is -1.8 km (Squyres et al., 2006), and that of Curiosity is -4.5 km (Vasavada et al., 2014), with respect to datum.

The elevations at which the two rovers are located make the similarity in column opacity puzzling. Due to Curiosity being nearly 2.7 km lower in elevation than Opportunity, one would expect to observe higher opacities above Gale Crater than Meridiani Planum. If we assume a constant dust mixing ratio with height above both sites, when integrated for the depth of the atmosphere, to obtain an opacity, since there exists more atmosphere above Gale Crater, a higher opacity is expected. This has led to the idea that the atmosphere within Gale Crater itself is relatively dust free.

In this section I look at two methods that attempt to approximate the extinction due to dust in the atmosphere above the crater. The two methods differ in their assumptions and can be thought of as limits to the actual extinction seen in this layer.

3.5.1 Pre-Peer Review

Lidar studies on Mars, such as Dickinson et al. (2011); Komguem et al. (2013); Whiteway et al. (2009), have shown that most dust in the atmospheric column is within the planetary

boundary layer (PBL). As such, the column-averaged extinction reported here is the column opacity divided by the depth of the PBL.

Average peak PBL depths are derived from MarsWRF (Richardson et al., 2007; Toigo et al., 2012) and the values reported by Guzewich et al. (2017) are used here. These are derived from the high spatial resolution "B" grid MarsWRF simulation described by Newman et al. (2017) for increments of 30° in solar longitude and are in Figure 3.5B.

Figure 3.5 compares the mean valued LOS-Ext to that of the column-averaged extinction as a function of solar longitude. The column-averaged extinction values are greater than the LOS-Ext values implying a much larger dust mixing ratio exists in the atmosphere above the crater with relatively dust-free air in the crater. Guzewich et al. (2017) confirms this with the support of orbital observations from the Mars Climate Sounder (MCS).

The values do appear to converge annually leading up to $L_s = 300°$ indicating a more homogenous dust-mixing ratio to greater altitudes above Gale Crater in this season. This corresponds to the annual maximum LOS-Ext and the annual minimum column-averaged extinction. This is likely due to an inflated PBL during this season (Fonseca et al., 2018; Guzewich et al., 2017) where the height of the PBL is some 5+ km above the crater floor. This inflated PBL is more than sufficient to reach the atmosphere above the crater rim (which itself is only $\sim$ 2 km above the crater floor), allowing mixing between the air above and that inside the crater, yielding similar values in LOS-Ext and column-averaged extinction.

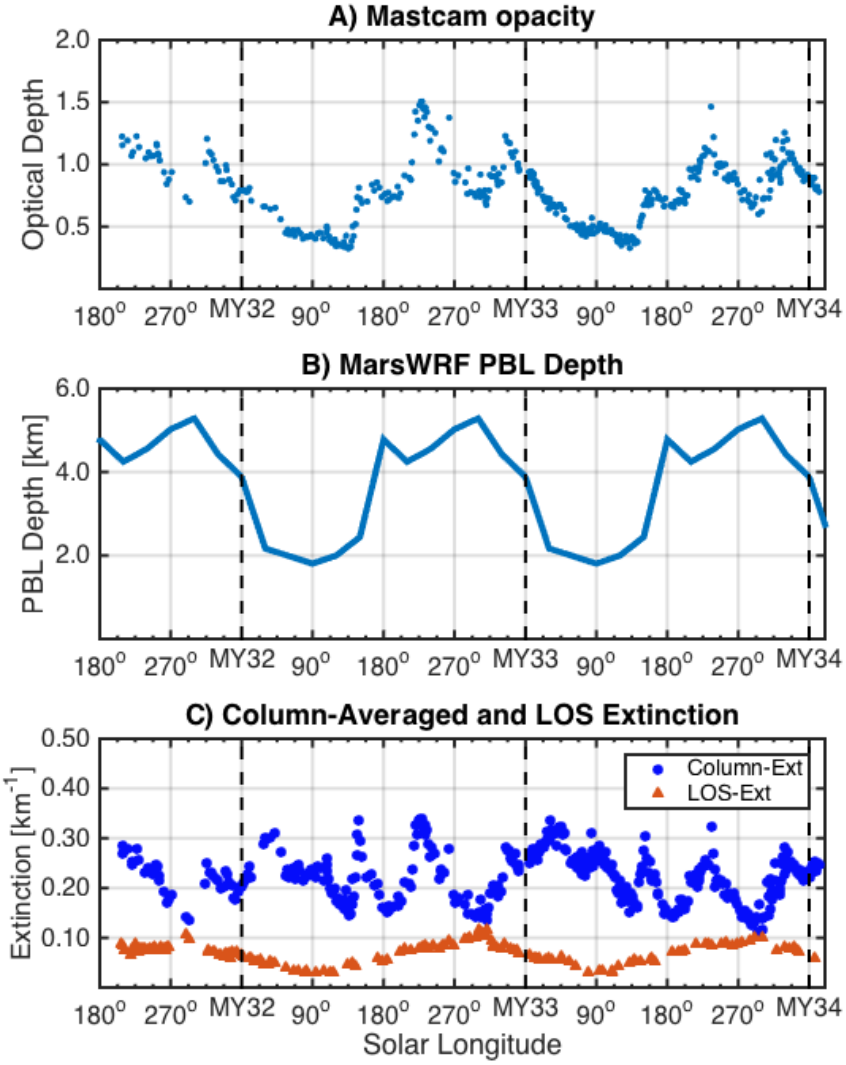

Figure 3.5: ***Mastcam Opacity; MarsWRF PBL Depths; CA-Ext vs LOS-Ext***

A) Mastcam opacity shown as a function of solar longitude. B) MarsWRF predictions of the PBL depth at 30° intervals in solar longitude. C) Column-Averaged Extinction and LOS-Ext as functions of solar longitude. The Column-Averaged Extinction is arrived at by dividing the Mastcam Tau opacity by the MarsWRF PBL Depth.

3.5.2 Peer-Review

The above assessment of the averaged extinction in the atmosphere above Gale Crater was not taken seriously under peer-review. The complaints were as follows: 1) Do polar latitudes in one season represent the column extinction year round for all latitudes (in reference to using Phoenix Lidar data). 2) Guzewich et al. (2017) suggests a completely different vertical structure of dust above the Gale Crater.

I concur that it is potentially problematic to assume that the dust profile above Phoenix during summer time can be representative of the entire planet for all seasons. The study by Guzewich et al. (2017) made use of the LOS-Ext, Rover Environmental Monitoring Station UV Sensor opacities and dust profiles from MCS on Mars Reconnaissance Orbiter to approximate the vertical profile of dust above Gale Crater. Shown in that study are seasonal opacities for dust within the PBL (LOS-Ext), dust high above the crater (MCS) and the layer sandwiched between the two, which has been reproduced here as Figure 3.6. Note the single peaked nature of the opacity within the PBL but an overall double peak in the total column opacity.

As such, I modified the analysis to obtain an averaged extinction of the layer above Gale Crater. Assuming that the extinction within the PBL is constant and valued as the LOS-Ext measurements, it is possible to derive an opacity for the dust within the PBL. This is done simply by multiplying the interpolated LOS-Ext by the interpolated PBL depth from the MarsWRF simulations. Subtracting this value from the interpolated Mastcam Tau values gives the opacity of the atmosphere above the PBL.

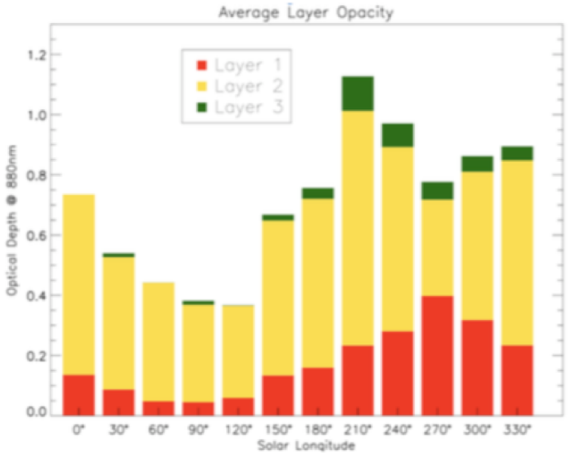

Figure 3.6: ***Three Layer Column Opacity***

Seasonal column opacities above Gale Crater confined to three layers: that of the PBL, the high atmosphere and the layer sandwiched in between. The figure is from Guzewich et al. (2017) and incorporates the LOS-Ext values for the opacity for the PBL and a combination of MCS and REMS UVS data for the two other layers.

To compare the LOS-Ext to the column averaged extinction above the crater, the scale height for dust in this layer is needed. Through the use of Phobos occultation photometry using the Mastcam, Mark Lemmon determined this scale height to be on the order of 8.5 km in the higher atmosphere (Mark Lemmon, *personal communication*). Thus the column averaged extinction above the crater is given by the difference in opacities of the atmospheric column and the PBL, divided by the scale height of dust in the high atmosphere (8.5 km).

This analysis significantly differs than the one above and the updated averaged column extinction compared to the LOS-Ext values can be seen in Figure 3.7 as a function of solar longitude. The LOS-Ext is shown to be slightly less than the column-averaged extinction for the majority of the Martian year save for southern summer $L_s = 270 - 360°$ and periods in which the two values converge, seen around $L_s = 135°$ and $L_s = 180°$ for MY32 and MY33. This suggests that the atmosphere within Gale Crater does indeed have a lower dust extinction value than the atmosphere above the crater during most seasons, but the opposite is true during southern summer.

3.6 Mastcam PBL Imaging

The Mastcam NCRE observations were assessed for the vertical structure of dust within the crater at a higher resolution than that offered by the Navcam observations. Early results were promising, where in images that were taken before 1100 LTST show a gradual increase of the LOS-Ext as altitude increases, while images taken after 1100 LTST show a near constant LOS-Ext with altitude to a certain depth in the atmosphere, after which the

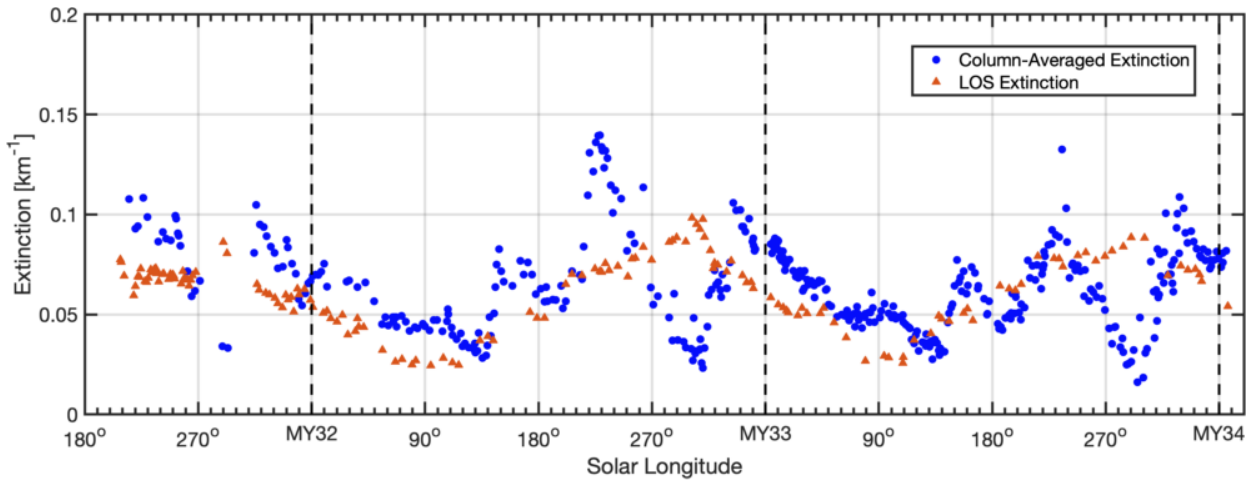

Figure 3.7: ***Updated Column Averaged Extinction versus LOS-Ext***

A modified analysis of the column averaged extinction that assumes the PBL has a constant LOS-Ext and is used to derive the opacity of the atmosphere above the PBL. This opacity is dividid by the scale height for dust at high altitudes to convert into an extinction.

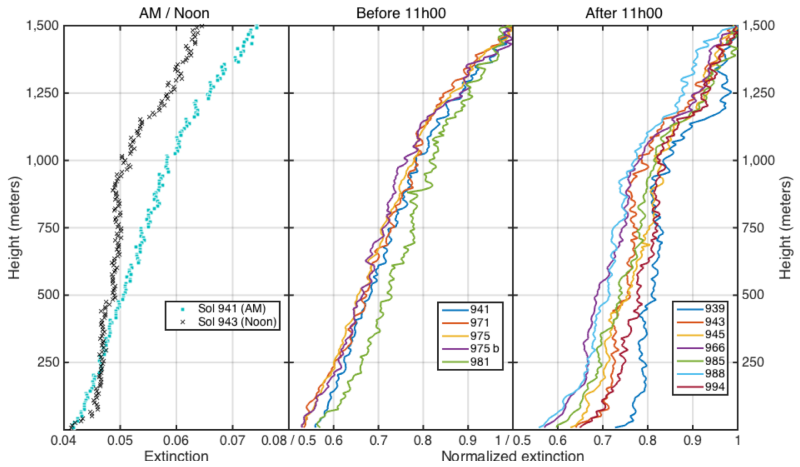

Figure 3.8: ***Mastcam LOS-Ext Case Study***

A vertical profile of the LOS-Ext was derived with the Mastcam NCRE images. This work is preliminary, but seems to suggest that at the time of these observations the PBL is well mixed, during the most convective time of sol, with an airmass of a higher capacity to hold dust existing above the crater floor. Note the use of Mission Sol instead of solar longitude. The images span were taken in MY32 between $L_s = 287 - 347°$.

LOS-Ext increases.

These observations show that the concentration of dust in the near-surface atmosphere within Gale Crater is indeed lower than the air above the crater during the most convective time of sol. Figure 3.8 shows the early results from this study, the first panel shows a comparison of a morning and afternoon observation, the second panel shows the 'normalized extinction' for each morning image and the third panel shows the 'normalized extinction' for each image taken after 1100 LTST. A normalized extinction was chosen to compare the shape of the profiles to one another as the actual LOS-Ext coefficients ranged wildly within

the dataset.

Work is being done to better understand these early results, and the imaging sequences have continued to be a part of the regular cadence of MSL.

3.7 Is Gale Crater a source or a sink for dust in the current era?

The analysis of the LOS-Ext compared to that of the column-averaged extinction, Figure 3.5C, suggests a much higher mixing ratio of dust above the crater. As such, treating this as a purely diffuse system, it is possible to approximate the rate at which dust settles into northern Gale Crater using Ficks First Law and a number of assumptions.

From Ficks first law:

$$J = -D\frac{\mathrm{d}\phi}{\mathrm{d}x} \tag{3.1}$$

where, J is the diffusion flux ($\mathrm{m}^{-2}\ \mathrm{s}^{-1}$), D is the Eddy diffusivity coefficient ($\mathrm{m}^2\ \mathrm{s}^{-1}$), and $\mathrm{d}\phi/\,\mathrm{d}x$ is the change in concentration of dust particles with depth (m^{-4}) of the PBL.

In this instance, the eddy diffusion rate is the most important factor to consider as it has the ability to affect the resulting diffusion flux the most. Rodrigo et al. (1990) suggest using a constant value on the order of 2000 $\mathrm{m}^2\ \mathrm{s}^{-1}$ for the Eddy diffusivity coefficient for middle latitudes for altitudes below 90 km. Later, Taylor et al. (2007) ran a 1D PBL simulation to derive Eddy diffusivity as a function of time and altitude in the martian atmosphere. The study showed that the peak Eddy diffusivity lasted several hours, on order of 20% of a sol, for near-polar latitudes. As such, if the constant value of 2000 $\mathrm{m}^2\ \mathrm{s}^{-1}$ from Rodrigo et al. (1990) is typical of noon-time peak Eddy diffusivity over Gale Crater, and if this peak diffusivity

lasts on the order of 20% of a sol in equatorial latitudes as it does in polar latitudes, the average Eddy diffusivity is approximately 400 m^2 s^{-1}.

The derivative, $d\phi/dx$, is treated as a constant within the PBL, $d\phi$ is the difference between the column-averaged extinction and the LOS-Ext , while, dx is the modeled depth of the PBL. A doubling and adding radiative transfer code (Moores et al., 2007) is used to establish a relationship between particle density and observed extinction (or opacity). This assumes the distribution of dust particles can be modeled by a modified Gamma distribution (Hansen and Travis, 1974) which has been used with success on Mars, e.g. using an effective radius of a = 1.6 μm and b = 0.2 would put the modal radius of optically active particles at 0.5 μm (Tomasko et al., 1999).

A settling rate is obtained from the diffusion flux by assuming the dust would fall out into a simple cubic packing regime, effectively assuming a static atmosphere.

The analysis performed here is shown in Figure 3.9 for the 'pre-peer reviewed' assumed column-averaged extinction of Figure 3.5. A plot of the sedimentation rate in μm sol^{-1} as a function of solar longitude can be seen in Figure 3.9. The settling rate of dust into the crater is very similar between the two Mars years, with an approximate cumulative 35 μm per Mars Year (μm MY^{-1}) of dust deposition for both MY32 and MY33. Note this methodology produces vastly larger settling rates in southern autumn and winter, with approximately 80% of the total dust deposition occurring in the first half of the year (L_s = 0 – 180°). This makes some intuitive sense, as the second half of the Mars year (southern spring and summer) experiences windier conditions (Newman et al., 2017; Rafkin et al.,

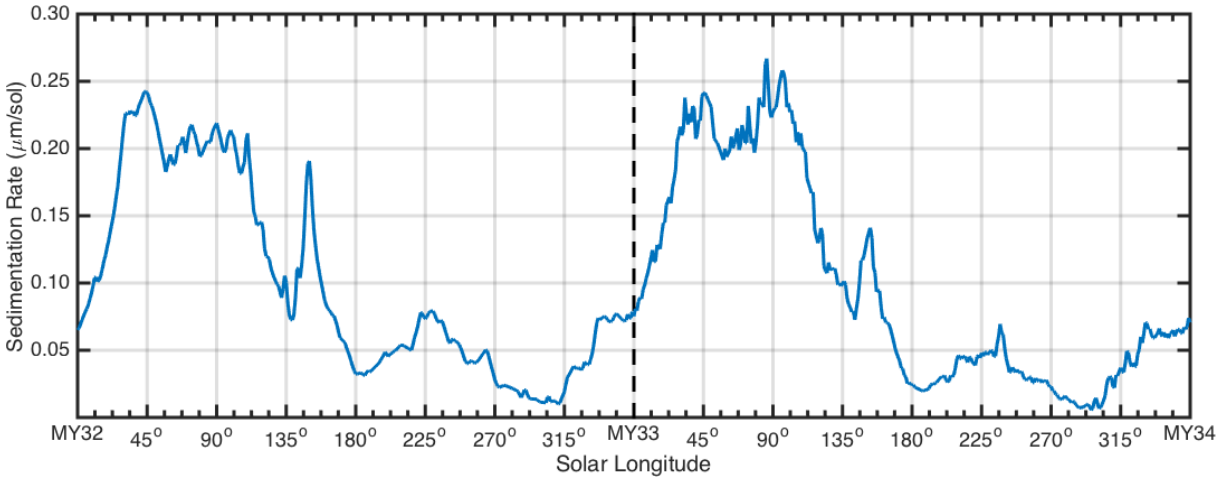

Figure 3.9: ***Sedimentation Rate of In-Falling Dust in Gale Crater, Mars***

A sedimentation rate is approximated for Gale Crater by comparing the LOS-Ext and the 'pre-peer reviewed' column-averaged extinction and invoking Fick's first law and a number of assumptions. A rate of 35 μm MY^{-1} is obtained for both MY32 and MY33, consistent with findings at other locations on Mars and other studies within Gale Crater.

2016) and is modeled to have a much thicker PBL (Fonseca et al., 2018; Guzewich et al., 2017) fighting against the settling of dust into the crater.

A similar analysis is preformed on the 'peer-reviewed' assumed column-averaged extinction of Figure 3.7. The diffusion rate of dust into and out of he crater is shown in Figure 3.10. The vertical axis is now a diffusion rate in the same units as before, but the terminology change is due to the inclusion of negative sedimentation rates, where as before we only saw positive. A negative sedimentation rate implies that dust is lifting from the crater floor to higher altitudes in the atmosphere. A positive diffusion rate implies dust is settling into the crater while a negative diffusion rate implies dust lifting. In MY32 were the inversion

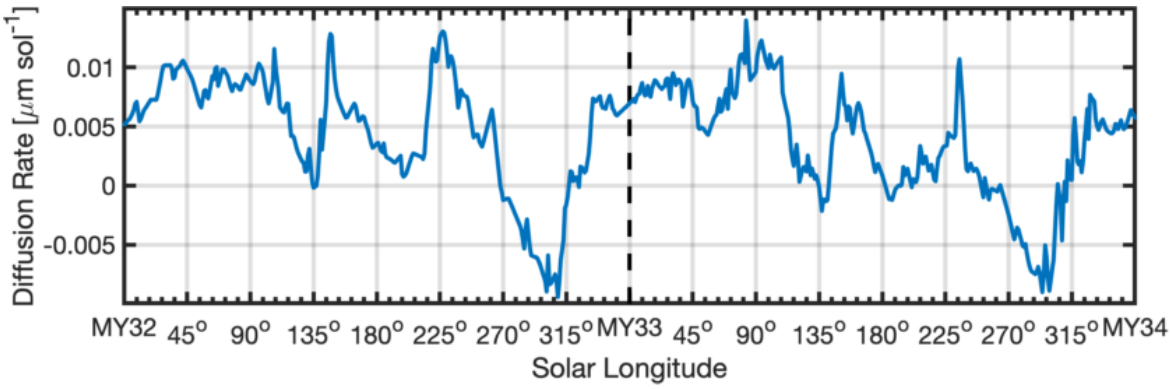

Figure 3.10: ***Diffusion Rate of In-Falling Dust in Gale Crater, Mars***

A diffusion rate is approximated for Gale Crater by comparing the LOS-Ext and the 'peer reviewed' column-averaged extinction and invoking Fick's first law and a number of assumptions. A rate of 2.7 to 3.5 μm MY^{-1} is obtained for both MY32 and MY33. Here the term diffusion rate is used because we see negative diffusion, meaning dust lifting in the second half of the Mars year.

is seen in the vertical profile around $L_s = 200°$ the diffusion rate is positive suggesting dust lifting in this season, whereas in the small inversion seen in MY33 around $L_s = 215°$ the diffusion rate is negative suggesting dust being injected into the crater. Integrating the rate of diffusion yields 3.5 μm MY^{-1} of dust accumulation within Gale Crater for MY32 and 2.7 μm MY^{-1} accumulation for MY33.

The values obtained from this methodology can be considered as bounds to the true diffusion flux of dust into and out of Gale Crater. Comparatively, others have seen sedimentation rates at the Mars Pathfinder landing site to be 40 - 80 μm MY^{-1} (Johnson et al., 2003) and at the Phoenix landing site to be 40+ μm MY^{-1} (Drube et al., 2010). Corresponding values

for MER Spirit and Opportunity have been reported to be on order of 20 μm MY^{-1} and 16 μm MY^{-1} for their respective landing sites (Kinch et al., 2007).

Estimates for the sedimentation of dust within ancient Gale Crater range in value but are consistent with the bounds set here. It is in line with the 10-100 μm MY^{-1} suggested by Lewis and Aharonson (2014) for the formation of rhythmites and closely matches the 8-37 μm MY^{-1} deposition rates required to create Aeolis Mons as modeled in Borlina et al. (2015). Furthermore, when Gale Crater acts as a sink for atmospheric dust (positive diffusion) we believe this is suggestive of a suppressed PBL verifying results of previous models. It is only in the later half of the year where Gale Crater acts as a source for atmospheric dust. This occurs when the PBL is inflated enough to reach the higher altitudes of the dust above the crater.

3.8 Dust mixing within Gale Crater

Insights in to how well mixed the atmosphere is, inside the crater, can be provided by the vertical structure of dust within Gale Crater. The observations used in this analysis are all within two hours of local noon and thus are a snapshot of the most dynamically active time of day. In a similar process to that used in Section 3.7, rates of deposition and/or dust lifting can be calculated. This time, instead of allowing the reservoir of dust above the crater to diffuse into the crater through the depth of the PBL, the dust from higher elevations, but still within the crater, is compared to that of the dust closer to the crater floor. This analysis uses the data from Figure 3.4 where a mean LOS-Ext value for the 8 highest altitudes is

subtracted from the mean LOS-Ext value for the 8 lowest altitudes. The depth at which dust is diffusing in this situation is roughly 850 m.

Contrary to the analysis in Section 3.7, where Gale Crater is found to be a sink for dust in the martian atmosphere, it is seen that over the course of a martian year during the most convective time of day, dust lofts weakly from the crater floor to higher altitudes which is to be expected. Figure 3.11 gives a rate of diffusion for MY32 and MY33. The rate is positive more often in MY32 than in MY33, e.g. MY32 $L_s = 0 - 45°$, $L_s = 190 - 230°$ and near $L_s = 350°$. In MY33, the rate is positive during three short periods: near $L_s = 10°$, $L_s = 100°$, and $L_s = 210°$. This rate is predominately negative, meaning dust is being lifted from the crater floor on a sol-to-sol basis but from the vertical structure of LOS-Ext in Figure 3.4 it is believed that this lifting of dust from the crater floor is not vigorous enough for Gale Crater to be a source of dust for the atmosphere above the crater.

3.9 Summary

The line-of-sight extinction in the northern portion of Gale Crater is reliably repeatable on an interannual basis. This suggests that the mechanisms responsible for the dust-loading environment of the crater (topography and wind patterns) are consistent, year-over-year. The visibility within the crater is high (e.g. low LOS-Ext) during southern autumn and winter ($L_s = 0 - 180°$) and low (e.g. high LOS-Ext) during southern spring and summer ($L_s = 180 - 360°$).

Dust is seen to be lifting from the crater floor by analyzing the vertical distribution of

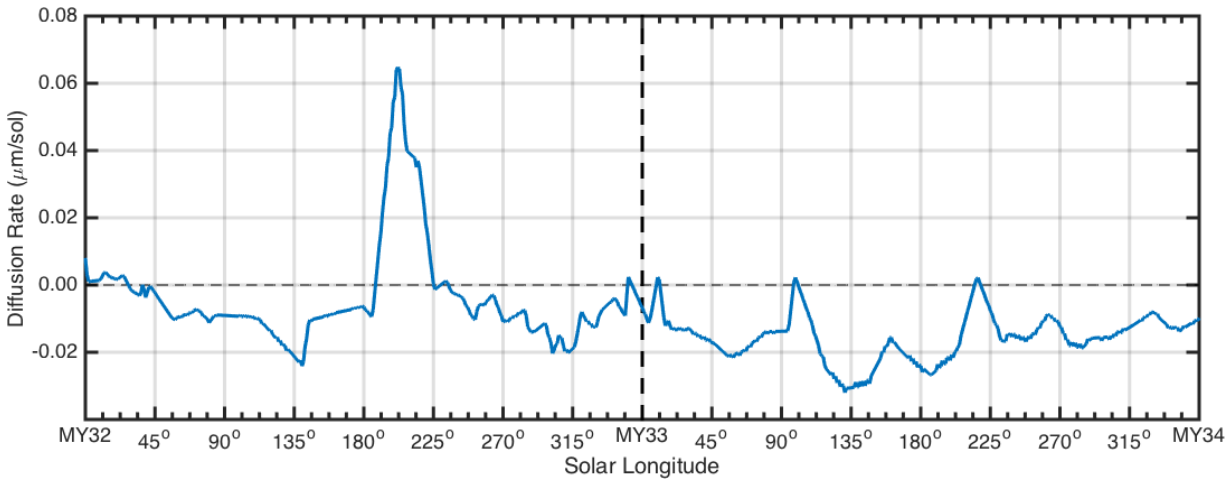

Figure 3.11: ***Dust Mixing within Gale Crater, Mars***

Dust mixing in the atmosphere inside the crater A similar diffusion rate is calculated for air interior to Gale Crater by comparing the LOS-Ext at a high and a low altitude. Net negative rates of diffusion are seen, implying that during the most convective time of day, winds are capable of lofting dust into the air interior to the crater, which is to be expected.

dust within the crater during the most convective time of day. Dust within Gale Crater is not well mixed during the most convective time of day, as a gradient in the dust loading exists, exhibiting higher concentrations of dust at higher altitudes within the crater than those of the crater floor.

Comparisons between LOS-Ext and the 'pre-peer review' column-averaged extinction imply a greater dust-mixing ratio existing in the atmosphere above the crater for the duration of the Mars year. Comparisons between the newer, 'peer-reviewed' column averaged extinction and the LOS-Ext suggest that the LOS-Ext is slightly less than the column-averaged extinction for the majority of the Martian year save for southern summer $L_s = 270 - 360°$ and periods in which the two values converge, seen around $L_s = 135°$ and $L_s = 180°$ for MY32 and MY33. This suggests that the atmosphere within Gale Crater does indeed have a lower dust extinction value than the atmosphere above the crater during most seasons, but the opposite is true during southern summer. These two scenarios are thought of as bounds to the true extinction of the dust above the crater.

Using a simple diffusion model, ignoring dynamics, and assuming Gale Crater is a sink of dust for the Martian atmosphere sets bounds for the diffusion rate of dust into and out of Gale Crater. An accumulation of infalling dust is expected to be between 2.7 and 35 μm MY^{-1}. This value is comparable to other landing sites and other analyses at Gale Crater. This analysis also suggests a positive diffusion rate of dust settling into Gale Crater, a situation that is indicative of Gale Crater having a suppressed PBL as predicted pre-landing (e.g. Tyler and Barnes (2013)).

4 Transmission Spectroscopy: Experimental Apparatus and Methodology

This experiment aims to characterize the transmission of radiation through packed martian regolith samples and thin slices of impact generated rocks as a function of wavelength and scattering angle.

Transmission is the ratio between the amount of light emitted from the sample to the amount that is incident the sample. We are interested in the transmission of three wavelength bands through the samples, Ultraviolet A (UVA; 315-400 nm), Ultraviolet B (UVB; 280-315 nm) and the photosynthetically active radiation (PAR; 400-700 nm) band. The ultraviolet section of the electromagnetic spectrum is typically subdivided into three wavelength bands based on their interactions with ozone in the Earths atmosphere. UVA is not absorbed by ozone and hence makes its way to the surface of Earth, UVB is mostly absorbed by ozone, and UVC (100-280 nm) is completely absorbed. The Ultraviolet (UV) and PAR regions of the electromagnetic spectrum have biological implications as UV wavelengths are typically harmful to living organisms and (in the case of plants) PAR wavelengths are a source of energy. This dissertation branches into astrobiology by examining how terrestrial organisms

would fare in a non-terrestrial radiation environment.

This chapter describes the experimental setup, data collection, calibration techniques, and methods of analysis. Following chapters cover the results for the martian regolith analogs (Chapter 5) and the impact generated rocks (Chapter 6), and concludes with a discussion on the potential astrobiological implications of light scattering through these samples (Chapter 7).

4.1 The Experimental Apparatus

The setup consists of a mini-goniometer, two Maya 2000 Pro spectrometers (wavelength ranges: 151 - 599 nm; 530 - 961 nm), two Newport arc-lamp sources (#6291: 200 W Hg(Xe); #6258 300 W Xe, Ozone Free) and simple optics to both reduce the diameter of the beam of light produced in the arc-lamp housing and to redirect the beam to illuminate the samples from below. A schematic of the experimental apparatus can be seen in Figure 4.1.

4.1.1 Mini-goniometer Setup and Usage

A mini-goniometer is conceived of and is built, by myself, in order to characterize the transmission of radiation through martian regolith and rock analog samples. A goniometer is an instrument that can be rotated to specific angular positions. The goniometer in use for these experiments is designed to sample three-dimensional space, in that we track both azimuthal and elevation angles. Attached to the goniometer is a receiving telescope fiber optically connected to a spectrometer. We term the setup as a mini-goniometer as the it is confined to

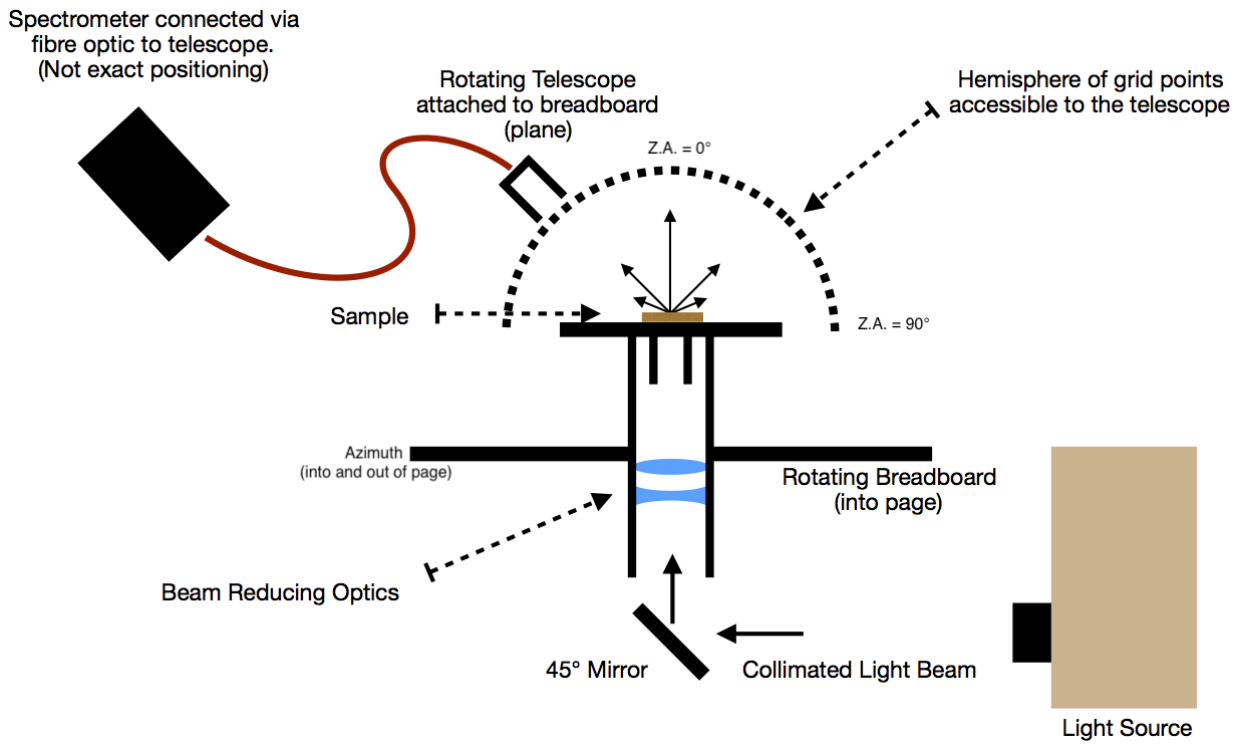

Figure 4.1: ***Experimental Apparatus Schematic***

Diagram of the experimental apparatus. A collimated beam of light strikes a mirror mounted at 45° which then reflects the light through a series of beam diameter reducing optics. The reduced beam then illuminates the sample from below. The breadboard rotates azimuthally and the telescope can change zenith angles. Not shown is the tilt-able arm holding the telescope. Combined the rotating breadboard and tilt-able arm are referred to as a mini-goniometer.

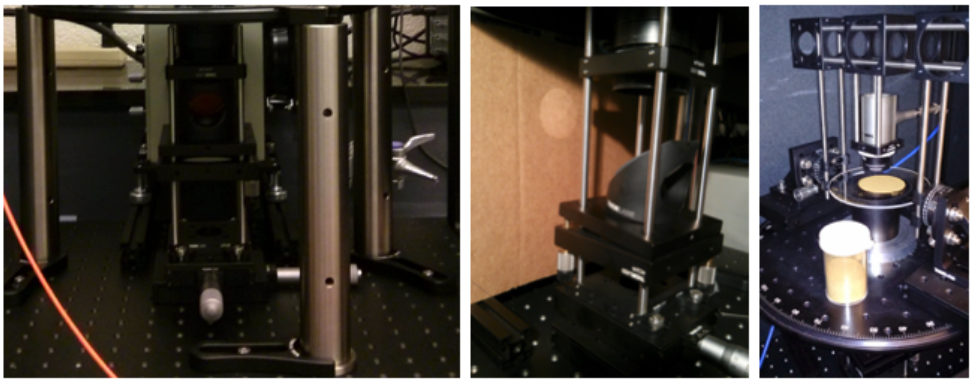

Figure 4.2: ***Experimental Apparatus Photos***

Left: Two stacked linear stages hold a cage-system that houses the 45° *mirror used to illuminate the samples from below, in the background, the light source housing is seen. Middle: Alternate view of the* 45° *mirror and cage system. Right: Rotating breadboard, sample, and telescope are shown after a run of JSC Mars-1.*

a box with a volume of 0.2 m^3, compared to a much larger automated version used in Mike Daly's lab that takes up an entire laboratory (Shaw et al., 2016). Pictures of the setup are shown in Figure 4.2 in which the telescope is mounted above the stationary sample platform on a rotating breadboard. The arms of the telescope are connected to two rotating stages that allows the elevation angle of the telescope to be adjusted. Thus, allowing measurements of the entire upward hemisphere to be made with the mini-goniometer. As the samples are illuminated from below, the mini-goniometer allows the transmission of radiation through the samples to be assessed in three-dimensional space.

The operator of the mini-goniometer is responsible for manually adjusting the angle the telescope makes with respect to normal (the elevation angle). This is done by turning two

knobs in tandem away from the operator, one knob for each continuous rotating stage. The stage is equipped with a vernier scale allowing precision adjustments to within 5 arcmin. In the case of this project, operators never needed to adjust the zenith angle by less than 2° increments, but are told to make use of the vernier scale in an attempt to be as precise with their measurements as possible.

Additionally, the operator of the mini-goniometer needs to manually adjust the azimuthal angle of the telescope. This is done by rotating the breadboard to which the telescope is mounted. Typically, during data collection the azimuthal angle is adjusted in increments of 20° or 30°, for a full 360°. The rotating breadboard has markings in 1° increments and it is expected that the operator is capable of a precision on the order of ± 2°.

4.1.2 Light-Sources, Spectrometers and Optics

The Newport arc-lamp sources were chosen as they are high power solar simulator light sources. This work primarily uses the Newport #6258 300 W *Xe*, Ozone Free. A plot of the irradiance as a function of wavelength for the Newport #6258, given by Newport, is shown in Figure 4.3. Shown in Figure 4.4 are the counts per ms as a function of wavelength recorded by the spectrometers for the 300 W *Xe* arc-lamp, looking through 4.6 orders of optical depth (discussed below) in the laboratory.

The spectrometers are from Ocean Optics and are from the Maya 2000 Pro series. One is optimized for UV and visible wavelengths (151.04 - 598.82 nm) and is colloquially referred to as the UV spectrometer (Serial Number: MAYP111150), and the other is optimized for the

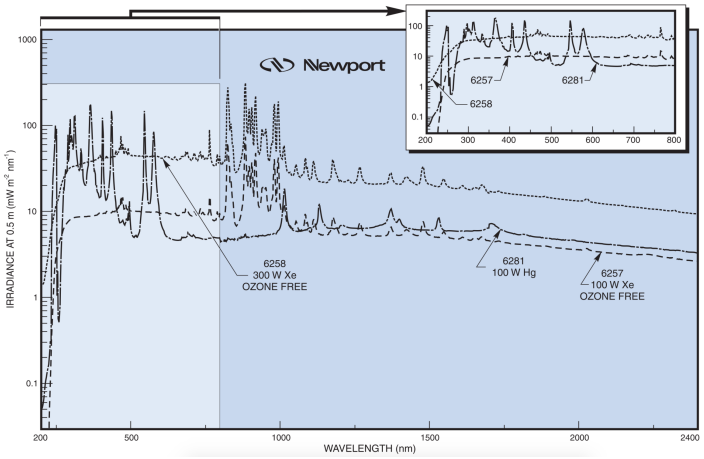

Figure 4.3: ***300 W #6258 Irradiance***

Irradiance at 0.5 m for the Newport #6258 300 W Xe *arc-lamp used in this dissertation. The plot is taken from the specifications sheet and is available here: https* : *//www.newport.com/medias/sys$_m$aster/images/images/hfb/hdf/8797196451870/Light−Sources.pdf*

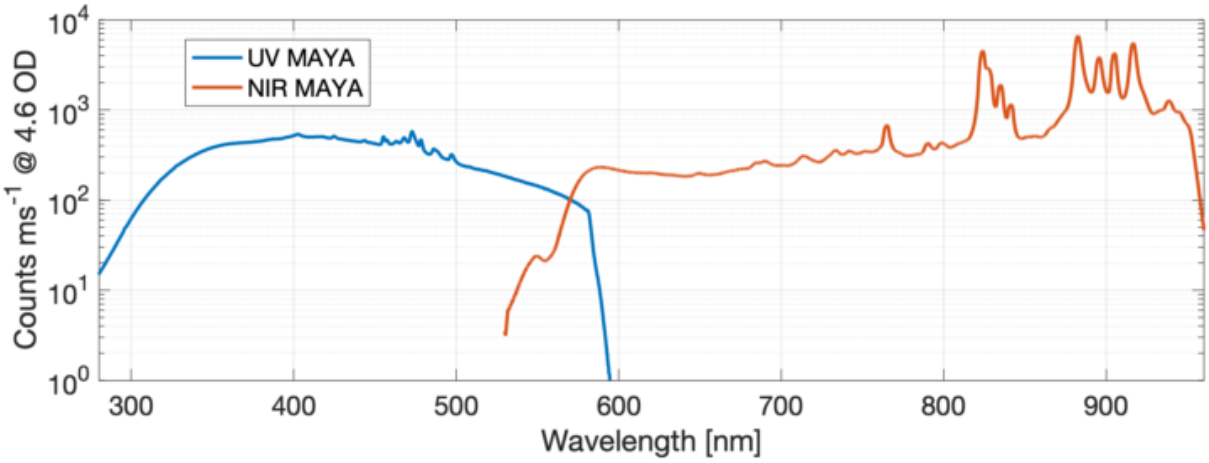

Figure 4.4: ***Light Throughput***

The relative intensity of the 300 W Xe *arc-lamp as a function of wavelength as observed by the UV and NIR spectrometers from Newport.*

visible and NIR wavelengths (529.84 - 961.41 nm) and is colloquially referred to as the NIR spectrometer (Serial Number: MAYP112029). The UV spectrometer has an H1 diffraction grating (600 lines/mm) and a blaze wavelength of 300 nm. The NIR spectrometer has an H4 diffraction grating (600 lines/mm) and a blaze wavelength of 750 nm. The number of lines per millimeter in the diffraction grating corresponds to the spectral resolution of the spectrometer and the blaze wavelength reflect where each spectrometer is most efficient.

A collimated beam of light leaves the light-source housing. The beam of light is normally incident to and over-fills a 5 cm diameter mirror placed at 45° with respect to normal. The light is reflected upwards into the positive normal direction and encounters two optics to reduce the beam size before it illuminates the samples from below.

This results in a beam of light roughly 25 mm in diameter being incident on the under-

side of the samples. The light interacts with the sample by being scattered and absorbed. The mini-goniometer is used to collect the scattered and transmitted light in the forward hemisphere.

It is often necessary to place up to six decades of opacity in front of the telescope due to the high intensity of the light source and the high sensitivity of the spectrometers. This is done with a set of mounted reflective neutral density filters from ThorLabs. The filter's substrate is UV-Fused Silica, transmissive in the range of 200 - 2600 nm in wavelength. A coating of Nickel on the substrate provides the neutral density, which is base-ten logarithmic, and ThorLabs recommends an upper limit of operation to 1200 nm. That is, if I_o is the intensity of the incoming light, for an opacity of τ, the transmitted light, T, is attenuated by $T = I_o \cdot 10^{-\tau}$.

However, in practice these neutral density filters are wavelength dependent. Specification sheets from ThorLabs provide the opacity as a function of wavelength for each filter and are reproduced in Figure 4.5.

4.2 Experimental Steps

An overview of the experimental steps are outlined below with references to relevant sections for further detail.

1. Place a 5.2 optical depth filter on the telescope and move to an elevation of 30°.

2. Turn on the arc-lamp power source and the arc-lamp.

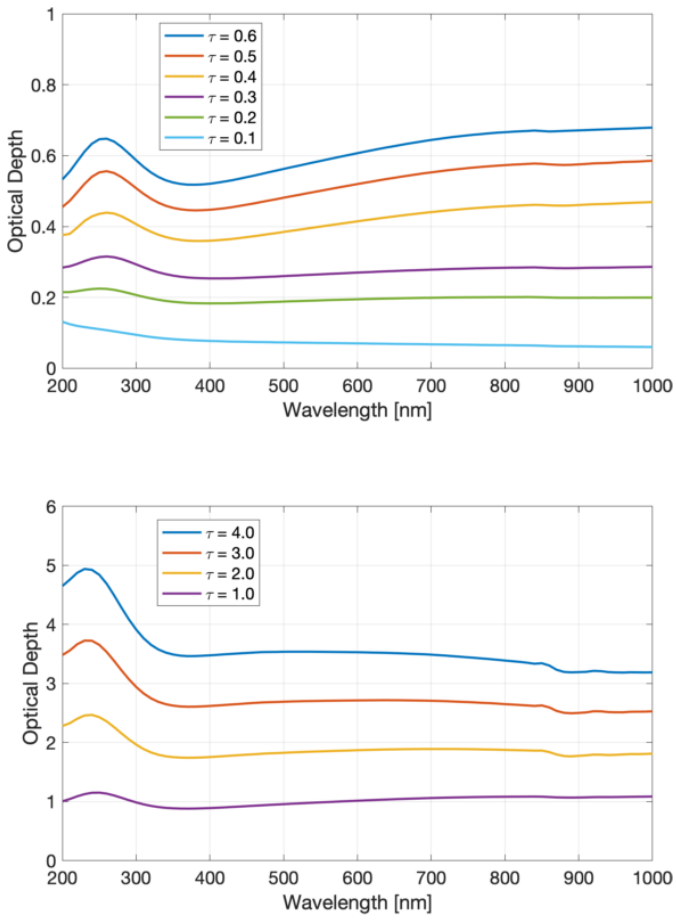

Figure 4.5: ***Opacity versus Wavelength for the ThorLabs NUK01 ND Filters***

Opacity versus wavelength for the ten ThorLabs NUK01 ND Filters used to attenuate the incoming radiation shown for the wavelengths of the spectrometers. The quoted value on each filter is for 300 nm in wavelength. Top: filters with less than 1 decade of optical depth. Bottom: filters with 1 or more decades of optical depth. The data is compiled from the specification sheets from ThorLabs and can be found here:

$https://www.thorlabs.com/newgrouppage9.cfm?objectgroup_id = 3193$

3. Prepare the sample. For regolith see 4.6.1 for rocks see 4.6.2.

4. After the lamp is warmed up (a few minutes), adjust the elevation angle back to 0° and take a reference 'Light' spectra. See 4.3.

5. Place the sample on the sample stage mount.

6. Adjust the amount of optical depth on the telescope in tandem with the integration times to minimize both, use the NIR spectrometer as a reference. See 4.3.

7. Start saving spectra at intervals of 20° (regolith) or 30° (rocks) for the entire range of 0° to 360°.

8. Switch the optical fiber to the UV spectrometer, adjust integration times, but *do not* adjust the optical depth on the telescope.

9. Repeat Step 7 for the UV spectrometer.

10. Adjust the elevation angle (see Table D.1 for regolith and Table D.2 for rock sample elevations used).

11. Switch back to the NIR spectrometer and repeat Steps 6 - 10 until all elevation angles have been collected.

12. Turn off the arc-lamp and wait for the power source to read 0 Watts.

13. Begin collecting 'dark' spectra for both spectrometers at the optical depths and integration times used for each elevation angle.

14. Finally, save a reference 'dark' spectrum to match the 'light' spectrum taken in Step 4.

4.3 Data Acquisition

The process to collect transmission spectra is fairly straight-forward with only minimal modifications needing to be made on-the-fly by the operator. This section details this process. It should be noted here that, I, personally collected roughly half the spectra used in this study with the remaining spectra collected by undergraduate research assistants. As such, I will make use of 'the operator' as the person collecting the experimental data.

The operator places 5.2 optical depths on the telescope before turning on the light source. The added opacity minimizes the chance of overexposing the pixels on the CCD within the spectrometers. The 5.2 orders are achieved by stacking three of the mounted UVFS ND filters, e.g. NDUV40A ($\tau_4 = 4$), NDUV10A ($\tau_1 = 1$) and NDUV02A ($\tau_{0.2} = 0.2$), on top of one-another. That is $\tau_{total} = \tau_4 + \tau_1 + \tau_{0.2}$ as, $x = a + b$ in the case that $10^{-x} = 10^{-a} \times 10^{-b}$.

The order in which they are stacked matters, to reduce multiple scattering within the stack of filters, the filter with the highest opacity is placed on the bottom of the stack, closer to the source.

To begin, the light source needs to be turned on and allowed to warm up. This step is more crucial for the 200 W *Xe(Hg)* light source as the mercury within the bulb needs to be vaporized before the light-source is stable, typically three to five minutes in duration. For the 300 W *Xe* bulb, a typical warm up duration is one to two minutes.

While the bulb is warming up the operator typically prepares the sample. This process is detailed in Section 4.6 for both the regolith analogs and the crystalline rock samples.

Before a sample is placed on the sample stage, the operator collects one spectrum for each spectrometer. These spectra are colloquially referred to as 'lights' and are taken at an azimuth angle of 0° and perpendicular to the sample stage. A series of 'darks' are also collected, at the end of the run. The 'lights' are a record of the incoming radiation and will allow the ratio of transmitted radiation to be determined. Since the arc-lamps have a designed lifetime on the order of 1000 hours, it is important to collect these spectra before and after each sample is run through the system. This allows for any changes in the intensity of the bulb to be recorded and ensures that the transmission data can be compared to one another.

Once the 'lights' have been taken and the sample is prepared, the operator places the sample on the sample stage. With the telescope connected to the NIR spectrometer, the operator inspects the spectra in the OceanOptics Spectra Suite software. The operator then adjusts the amount of opacity and the integration time so as to minimize both. The NIR spectrometer is used to make these adjustments because the 300 W Xe bulb has very intense peaks in the NIR as seen in Figure 4.4. The same amount of opacity is used for both NIR and UV data collection, however, the operator is expected to adjust the integration times and the number of scans to average over so as to obtain spectra with decent signal-to-noise.

The SpectraSuite software can be set up to automatically save spectra given a set of conditions. The operator will typically set up this autosave routine having the software collect

19 spectra and waiting 3-5 seconds between each save. The 19 spectra correspond to one spectrum being taken for every 20° in azimuth, with 0° and 360° being repeat measurements. The wait time allows the operator to rotate the breadboard by 20° after each spectrum is saved.

The operator collects measurements for each spectrometer. They then adjust the zenith angle of the telescope, adjust the opacity and integration time, and this process repeats until either the zenith angle is at its maximum (∼48°) or the integration times get too long and it becomes hard to distinguish a signal from noise.

Once the spectra have been collected, the operator turns off the arc-lamp and waits for the readout on the power source to read 0 Watts. A 'dark' spectrum needs to be taken for each combination of optical depth and integration time for each spectrometer. This includes 'darks' that match the 'lights' from the beginning of the run with no sample. These dark spectra are subtracted from the data collected to remove any noise that may have been added by the lighting conditions in the laboratory.

4.4 Calibration

The spectrometers in use are not radiometrically calibrated and thus do not measure power or flux. Instead, they give a digital number (DN) associated with the number of photons at each wavelength. This should not be an issue for this project as the collected data is taken as a ratio to the incoming radiation, giving the amount of light transmitted through the samples as a function of wavelength.

The optical fiber, telescope, mirror and lenses do not change between scans and hence their transmission properties can be ignored as they will affect the entire dataset in the same way. This is not the case for the ND Filters, which are added and subtracted to the system based on the amount of light penetrating the sample. For each zenith angle, all azimuthal spectra are collected with the same amount of optical depth attached to the telescope for both the UV and NIR spectrometers. However, when changing the zenith angle, it may become necessary to change the amount of optical depth as the amount of transmitted radiation is a function of the scattering angle.

The set of filters, item NUK01 from ThorLabs, are optimized to attenuate ultraviolet radiation, and hence their quoted opacity represents the amount of attenuation at 300 nm in wavelength. Fortunately, ThorLabs provides specification sheets that detail the opacity with wavelength (200 - 2200 nm) for each of the filters and can be seen in Figure 4.5 for wavelengths used in this project. A quick inspection of Figure 4.5 and one can see why the transmission properties of the ND filters needs to be accounted for: in the UV (200 - 400 nm) the opacity varies significantly with wavelength, while in the PAR (400 - 700 nm), roughly stable values of the opacity are seen for the three least ($\tau = 0.1 - 0.3$) and four most ($\tau = 1.0 - 4.0$) optically thick filters. Seeing as the general trend of how the opacity changes with wavelength is not constant across the filters and remembering that the opacity and transmission are related to one-another by a logarithm, each transmission spectra collected needs to be calibrated to take into account the amount of optical depth placed on the telescope during its acquisition.

4.4.1 Spectra Processing

The spectra are scaled to provide a DN per wavelength per millisecond at zero optical depth. The process is similar to that outlined here for a hypothetical spectra collected with optical depth $\tau(\lambda)$ as given by the ThorLabs specifications sheet, and an integration time of t_{int}. Let $I_r(\lambda)$ be the spectrum received by the spectrometer, let $I_{DARK}(\lambda)$ be the dark spectrum associated with $\tau(\lambda)$ and t_{int}. The scaled spectrum $I(\lambda)$, will be:

$$I(\lambda) = \frac{10^{\tau(\lambda)}}{t_{int}} \cdot [I_r(\lambda) - I_{DARK}(\lambda)] \tag{4.1}$$

Fortunately, adding multiple ND filters attenuates the received spectrum in an additive way, for instance, if the optical depth added to the telescope was $\tau = 2.2 = \tau_{2.2}(\lambda)$, composed of the $\tau = 2.0 = \tau_{2.0}(\lambda)$ and $\tau = 0.2 = \tau_{0.2}(\lambda)$ ND filters, then $\tau_{2.2}(\lambda) = \tau_{2.0}(\lambda) + \tau_{0.2}(\lambda)$.

The total scaled radiance incident the sample is determined from the 'lights' and 'dark' spectra collected without a sample on the sample stage. The incident radiation, $I_o(\lambda)$, is calculated as:

$$I_o(\lambda) = \frac{10^{\tau(\lambda)}}{t_{int}} \cdot [I_{LIGHT}(\lambda) - I_{DARK}(\lambda)] \tag{4.2}$$

Where, $I_{LIGHT}(\lambda)$ and $I_{DARK}(\lambda)$ are the spectra recored by the spectrometers for the 'lights' and 'dark' sources, respectively.

The percent transmission is calculated as the ratio of the scaled received spectrum to the scaled incident spectrum multiplied by 100:

$$T(\lambda) = 100 \cdot \frac{I(\lambda)}{I_o(\lambda)} \tag{4.3}$$

.

4.4.1.1 Lamp Features

In the initial analysis of the resulting transmission as a function of wavelength, spectral features reminiscent of those found in the 300 W *Xe* arc-lamp appeared. The steps to process these transmission spectra, e.g. those in 4.4.1, should compensate for the features in the *Xe* arc-lamp, but did not. To try to understand what was going on, a new analysis on the kieserite samples was conducted. This process utilizes the dark current inherent to the spectrometer and is subtracted in proportion to the exposure time from each spectrum. The results were indeed similar to the analysis conducted before, where spectral artifacts remained.

These features could likely be attributed to temperature variations of the external environment when collecting the data. Spectrometers are sensitive to fluctuations in temperature, that if not accounted for could pose issues in the analysis. The offset and hence the dark current can be raised or lowered depending on ambient temperature, however this would not produce the resulting features in the transmission spectra. These features likely represent a shift in wavelength between the data collected for the samples and their associated incident radiation without the sample present ('Lights'). If the temperature decreases, the slits in the diffraction grating shrink in size, conversely, if temperature increases, the slits in the diffraction grating increase in size. A decrease in temperature results in a higher spectral resolution, meaning the spectral range decreases and shrinks from the blaze wavelength. An

increase in temperature results in a lower spectral resolution, meaning the spectral range increases and widens from the blaze wavelength.

The Maya 2000 Pro spectrometers used here are not thermally insulated and without a record of the ambient temperature, these artifacts could not be reconciled. As such, the spectra have been cleared of the resulting artifacts by incorporating a box-car smoothing routine to filter out the offending signals. If this work is to be published in a peer-reviewed journal, it is recommended to fully work out the issues introduced by non-uniform ambient temperatures.

4.5 Alignment and Known Response

The mini-goniometer has many degrees of freedom: there are four linear micrometer stages (two on the sending (mirror) end and two on the receiving (telescope) end), the mirror is also placed on kinematic mount to allow tip and tilt adjustments, and the telescope can be adjusted vertically and laterally. This can be a source for erroneous data collection, so a process by which to ensure proper alignment needed to be established.

To do so, light was sent through the system in the reverse direction, that is, sent from the telescope onto the sample stage. A calibration target is placed on the sample stage at the same vertical height a sample would be placed. The light from the telescope is collimated and produces an illuminated circle filling the calibration target. The breadboard is rotated, if the apparatus is properly aligned, the collimated light from the telescope will stay within the calibration target. If the apparatus is not aligned properly, adjustments to the linear stages

are made, and alignment is checked again. This process is repeated until the collimated light from the telescope stays within the calibration target.

To ensure the mirror is placed accordingly, a ground-glass diffuser is run through the system as it has a known response. The mirror is properly aligned once the peak intensity is at zenith and the transmittance matches the known response. These alignment measures are taken after every 2 (regolith) or 3 (rock) samples have been processed or whenever a significant period of time lapsed between collection (days to weeks). There was a period in which 15 runs were completed over one weekend, in this instance, the alignment measure was preformed before and after all runs were complete, no misalignment was detected.

The alignment is done by placing a 220 grit ThorLabs N-BK7 Ground-Glass Diffuser on the sample stage. The ground-glass diffuser disperses light in the forward direction in a gaussian profile as shown as the red curve in Figure 4.6, the data are from the specification sheet provided by ThorLabs and are measured at a wavelength of 780 nm.

The transmission spectra for the ground-glass diffuser is collected the same way as a regolith or rock sample would be. That is zenith angles ranging from 0°-30° from normal, favoring angles closer to zenith and a full 360° in azimuth in 20° increments for each elevation angle. The data is then averaged azimuthally, normalized and plotted against the data provided by the ThorLabs specification sheet.

An example of a calibration run can be seen in Figure 4.6, which shows the normalized transmission profile versus emission angle collected on March 15, 2016. The red line represents the profile given by ThorLabs while the black dots are the azimuthally averaged data

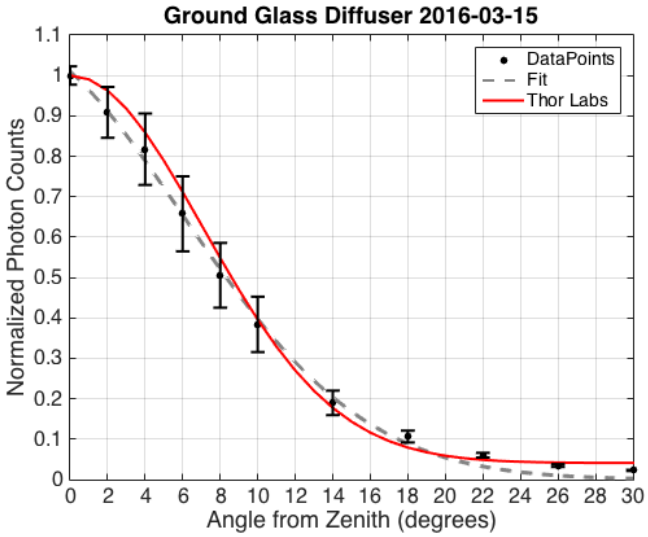

Figure 4.6: ***Ground-Glass Diffuser Calibration***

Comparison between measured (black points) and ThorLabs specification sheet (red line) for the light flux variations with zenith angle. The points were fit to a Gaussian (grey dashed line). The goodness of the fit is $R^2 = 0.9983$.

collected. The grey line fits the experimental data to a Gaussian function shown in the plot with an $R^2 = 0.9983$. The peak is centered at 0° and the experimental and known responses match within experimental error, ensuring that the mirror is indeed aligned properly.

4.6 Sample Preparation: Regolith versus Rocks

Chapters 5 and 6 give the results and analysis for two classes of materials run through the mini-goniometer transmission setup, namely martian regolith analogs and crystalline rocks. The procedure for collecting data remains the same as detailed above, but the two materials do require a different method to prepare the samples.

4.6.1 Regolith

The regolith simulant consists of crushed up rock (from Earth) made to match the spectral, chemical and mineralogical properties of the regolith found on Mars, and hence vary in their grain size and composition. The simulants used in this study are JSC Mars-1, basalt, cheto bentonite and kieserite acquired from Doug Ming (Johnson Space Center) and Andrew Schuerger (University of Florida).

Samples are placed in an aluminum template of varying thickness: 0.5, 1.0, and 2.0 mm and run through the mini-goniometer setup. The operator is responsible for preparing the samples, with instructions to remove and re-prepare the sample fully between runs of the same sample and thickness. This is done to randomize the particles in hopes of being able to collect transmission spectra for a general sample of this material.

The operator is instructed to fill the aluminum template with enough simulated regolith to be flush with the top of the template. This process involves physically packing the regolith into the template with the flat edge of a rectangular piece of aluminum. This reduces the porosity of the sample. The operator then places the sample over the light beam, to check their work. If any voids allowing light to escape without interacting with the sample were observed, more material is to be added and repacked.

4.6.2 Rocks

The catalog of crystalline rock samples that have been curated vary in their shock state (porosity), and composition. These rock slices were prepared by and used in a study to

assess the potential habitability of impact generated glasses for endolithic lifeforms (Pontefract et al., 2014) and have been donated to the laboratory pre-sliced into 0.5, 1.0, 2.0 mm thicknesses.

Many of the rock slices are narrower than the diameter of incident light in the setup detailed above. As such, it was necessary to reduce the diameter of incoming radiation by introducing an aperture, 1 cm in diameter, between the incoming beam and the rock sample. All methods remain the same; however, this time, the aperture stays in place for the 'lights', 'darks', and the ground-glass diffuser runs. This allows the rocks to be directly compared to one another.

The difference in size between the aperture and the rock samples themselves allowed most samples to be run through the mini-goniometer setup for three different locations on the rock sample to obtain an average transmission spectrum for the rock sample. Some rocks slices were too small to do multiple runs, in such cases, transmission spectra were still collected to test consistency.

4.7 Data Reduction

This project is interested in understanding the UVA, UVB and PAR transmission though the various samples at varying emission angles. The collection of data may produce thousands of spectra per sample. As such, we have decided to reduce the data from three dimensional space to a two dimensions by averaging the spectra azimuthally. Once the spectra are averaged azimuthally, they are calibrated using Equation 4.1, and then the transmission is

determined by taking the ratio of the azimuthally averaged spectra to the incoming radiation as determined by Equation 4.2.

The following two chapters discuss the transmittance of the regolith and rock samples. These results include the normal transmission (perpendicular to the sample) as a function of wavelength, as well as the cumulative transmission of UVA, UVB and PAR radiation as a function of emission angle. The cumulative transmission is calculated by summing up the total DN per wavelength band in the azimuthally averaged spectra and dividing by the total sum of DN per wavelength band from the calibrated total incoming radiation, for each zenith angle, multiplied by 100, e.g. Equation 4.3.

4.8 Numerical Models

The datasets were initially collected to derive Hapke parameters that define the physical characteristics of the samples, however, this proved to be impossible. The observed transmission through the samples were compared with numerical models of reflectance in an attempt to fit the Hapke parameters. The numerical models require reflectance measurements to fit the Hapke parameters and fitting these to martian analogs is common in the literature (Johnson et al., 2003; Pommerol et al., 2013; Sgavetti et al., 2006).

One of the most thorough mathematical models describing the reflectance spectrum is known as the Hapke bidirectional reflectance distribution function (BRDF) (Hapke, 1993, 2002, 2012a,b). The BRDF is the ratio of the power reflected off a surface to that of the power incident the surface.

Many mathematical models exist to characterize reflectance spectroscopy, but few can be applied to the transmission spectrum. Li (2008) reviews several models and concludes that Hapke's model does not work for transmission spectroscopy. The work into this project, done by myself, confirmed this assertion. As such, a model developed by (Sobolev, 1956, 1975), and expanded upon by Kokhanovsky (2002, 2004), for the transmission function of optically thin materials is examined here and applied to experimental data collected for a ground glass diffuser.

Both models begin by solving the radiative transfer equations, but do so by making different assumptions. The following sections will detail the two models and give examples in which the models do reproduce observational data.

4.8.1 Hapke Bidirectional Reflectance Distribution Function

Through inversion, it is possible to correlate Hapke's model to reflectance data to retrieve the single scattering albedo, ω, the width and intensity of the shadow hiding opposition effect (SHOE), h and B_0, the macroscopic roughness of the scattering medium $\bar{\theta}$, and the fitting parameters that define the 2-term Henyey-Greenstein scattering phase function, b and c.

The geometry and notation of the bidirectional reflectance measurements are detailed in Hapke (2012b) and reproduced here for completeness. Collimated light is incident on a scattering medium (atmospheric dust, rock samples, planetary surface). The incident irradiance makes an angle, i, to the normal of the scattering medium. The irradiance interacts with the scattering medium, some irradiance is absorbed, some is transmitted into the medium

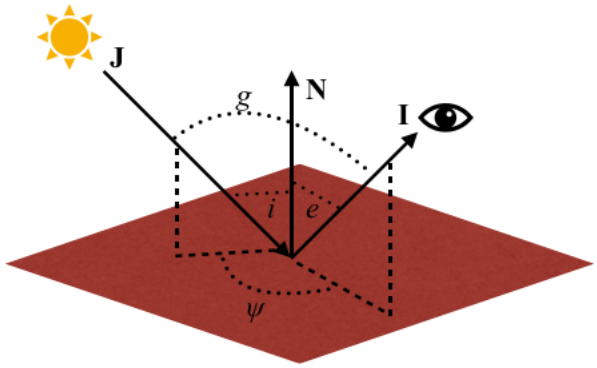

Figure 4.7: *Hapke Reflectance Geometry*

A sketch of the geometry for reflectance measurements. The surface is considered to be flat, the incident radiation, in this case the Sun, makes an angle i with respect to the normal of the surface. The light is emitted at an angle, e with respect to the normal of the surface, that is received by an observer. If i and e are in the same plane, the scattering angle, g is the sum of the angles i and e. ψ is the azimuth angle between planes of incidence and emergence, if $\psi = 0^\circ$ or 180° it is said to be in the principal scattering plane.

and some is reflected back into the hemisphere above the medium. An observer measures the amount of reflected light at an angle, e, to the normal of the scattering medium. The scattering plane, ψ, is the azimuthal angle between the incident irradiance and the observed emitted irradiance. When $\psi = 0°$ or $180°$ the scattering plane is called the principal plane. When the principle plane is used, g is the sum of the angles of incidence and emittance and is the scattering angle. See Figure 4.7 for an illustration of the reflectance geometry.

The mathematical model of bidirectional reflectance derived by Hapke (2012) is a function of i, e, and g. A useful substitution defines the cosines of the emitted and incident angles, μ and μ_0 respectively, as:

$$\mu = \cos(e) \tag{4.4}$$

$$\mu_0 = \cos(i) \tag{4.5}$$

The Isotropic Multiple Scattering Approximation (IMSA) of Hapke's model is examined in this dissertation for its ability to characterize the transmission properties of the martian regolith and crystalline rock samples. The BRDF of this model is written as:

$$BRDF(i, e, g) = \frac{\omega}{4\pi} \frac{\mu_0}{\mu_0 + \mu} \left\{ [1 + B(g)] \cdot p(g) + H(\mu_0) H(\mu) - 1 \right\} \tag{4.6}$$

Where $B(g)$ describes the SHOE, $p(g)$ is the phase function, and $H(x)$ is the Ambartsumian-Chandrasekhar H function.

The SHOE is a function of the scattering angle, g, and is parameterized by the width and intensity of the opposition surge, h and B_o, respectively as:

$$B(g) = \frac{B_0}{1 + (1/h) \tan g/2} \tag{4.7}$$

The phase function is assumed to be a two-term Henyey-Greenstein function, following the preferred method of Hapke (2012) the phase function takes the form:

$$p(g) = \frac{(1-b^2)}{2}\left[\frac{(1+c)}{(1-2b\cos g+b^2)^{3/2}} + \frac{(1-c)}{(1+2b\cos g+b^2)^{3/2}}\right] \tag{4.8}$$

were, b and c, describe the forward and backwards lobes of the phase function.

The Ambartsumian-Chandrasekhar H function is parameterized by the single scattering albedo, ω, and is a function of the cosine of the incident or emission angle. It can be approximated as (Hapke 2012):

$$H(x) = \left(1 - \omega x[r_0 + \frac{1-2r_0x}{2}\ln\left(\frac{1+x}{x}\right)]\right)^{-1} \tag{4.9}$$

Where r_0 is the diffusive reflectance, defined by: $r_0 = (1-\gamma)/(1+\gamma); \gamma = \sqrt{1-\omega}$. This approximation of the Ambartsumian-Chandrasekhar H function differs by less than 1% from the full analytical solution.

The way to make use of Hapke's models is via an inversion technique. Given a set of reflectance measurements, the parameters can be solved for in such a way that minimizes the differences between the model and the data. The exact process in which this is done varies in each paper, but a common approach uses a particle swarm optimization (PSO) routine (e.g. Pommerol et al. (2013)). This routine chooses an initial population of fit parameters, finds the populations that best fit the data, and refines its guesses, fitting a new population. The process continues in this way until a user-specified tolerance is met for the fit data.

4.8.1.1 Verification of Hapke's Model

I implemented the numerical IMSA BRFD model of Hapke into Matlab as a series of functions collectively referred to as the York Reflectance Fitting (YRF) model. To verify the model was put together correctly, Hapke parameters calculated for reflectance measurements of various JSC Mars-1 surfaces from Pommerol et al. (2013) were used to compare the reflectance factor as a function of viewing angle between my model and Pommerol et al. (2013). The measurements in Pommerol et al. (2013) were collected using the PHIRE-2 (PHysikalisches Institut Radiometric Experiment - 2) instrument in which light is incident to the surface of the sample and is collected at various emission angles with geometry similar to that in Figure 4.7. Pommerol et al. (2013) then use an iterative method to solve for the Hapke parameters using their own model in which the goodness of a fit is characterized by the total and reduced chi-square, χ^2 and χ^2_ν as:

$$\chi^2_\nu = \frac{1}{\nu}\chi^2 = \frac{1}{\nu}\sum_N \frac{(Measure - Model)^2}{\sigma^2} \tag{4.10}$$

Where ν is the number of degrees of freedom, e.g. the number of measurement points subtracted by the number of fitting parameters, and σ is the standard deviation of the measurements. In this method, a $\chi^2_\nu = 1$ indicates a perfect fit. $\chi^2_\nu > 1$ implies discrepancies between model and data, while $\chi^2_\nu < 1$ implies over-fitting.

The six Hapke parameters Pommerol et al. (2013) report on are: the single scattering albedo, ω, the width and intensity of the shadow hiding opposition effect, h_s and B_s, the macroscopic roughness parameter, θ in degrees, and the b and c parameters that characterize the two-term Henyey-Greenstein phase function and are reproduced in Table 4.1. Note that

	ω	h_s	B_s	$\bar{\theta}$	b	c	χ^2_ν
Surface A	0.526	0.083	1.0	13.3	0.187	0.273	1.4
Surface B	0.549	0.056	0.921	16.3	0.179	0.806	2.0
Surface C	0.603	0.043	0.936	14.1	0.189	0.452	1.9
Surface D	0.499	0.071	0.962	17.4	0.167	1.282	2.6

Table 4.1: *Hapke Parameters Retrieved PHIRE-2 Reflectance Measurements*

Parameters retrieved for four different JSC Mars-1 surfaces studied by Pommerol et al. (2013) in which reflectance measurements were taken, see Pommerol et al. (2013) for full details.

their χ^2_ν values are all over 1, implying that there are still some discrepancies between the model and the data.

These parameters were used as input into YRF to generate the reflectance factor as a function of emission angle for various incidence angles ($i = [0°, 30°, 60°]$). These incidence angles match those measurements reported.

4.8.1.2 Hapke modeling for Transmission

It was initially thought that the numerical models developed by Hapke (Hapke, 1993, 2002, 2012a) to characterize the bidirectional reflectance distribution function would be beneficial to characterizing the bidirectional transmission distribution function of martian regolith and

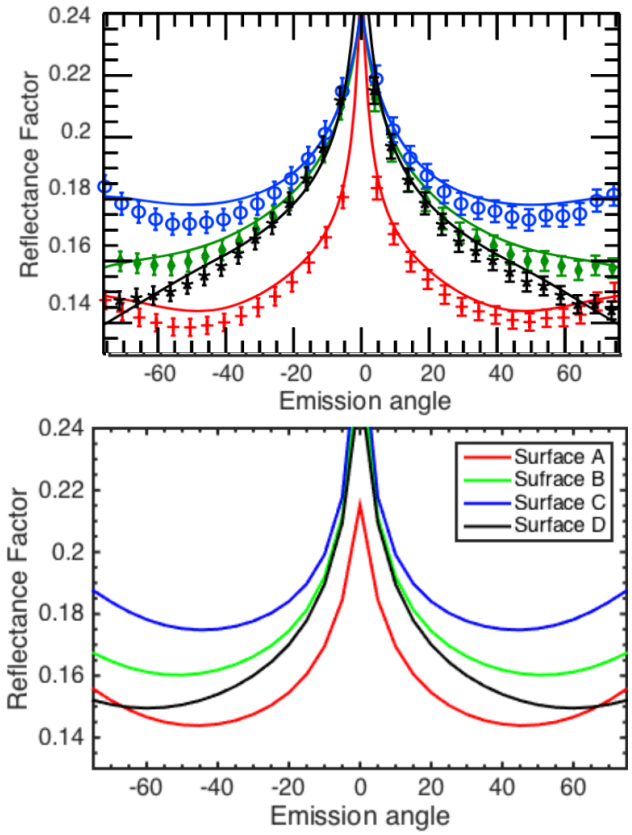

Figure 4.8: ***Hapke Reflectance Factor: Data and Numerical Model***

Top: Data-points (symbols) for the measured reflectance factor of four surfaces of JSC Mars-1 compared to the mathematical model (lines) that fit the data with the Hapke parameters in Table 4.1, plot taken from Pommerol et al. (2013). Bottom: The reflectance factor computed using the values in Table 4.1 for four surfaces of JSC Mars-1 using the YRF.

the thin slices of crystalline rocks. The intention was that if we wanted to characterize how light transmitted through the samples, we would only need to change the basis, allowing the angle of incidence to be -90°.

This effort was unsuccessful, perhaps due to the nature of the model attempting to fit the parameters that characterize the opposition surge, however, one would expect that the equivalent, say transmission surge, would be fit by these parameters. Given that a Hakpe model did not succeed at modeling transmission, the Sobolev-Kokhanovsky (Kokhanovsky, 2004) method was attempted. We validated their transmission distribution function for optically thin films in the case of the ground-glass diffuser, as seen in the next section.

It is also possible to simulate multiple particle scattering using a numerical simulation that tracks the photons as they scatter off a bed of particles. This is examined in some depth in Appendix C in an attempt to better understand the results obtained from the experiments involving the mini-goniometer.

4.8.2 Sobolev-Kokhanovsky

Much like Hapke's model, the method developed by Sobolev and Kokhanovsky begins with solving radiative transfer equations to model parameters of interest. In this dissertation, the thin-layer approximation is considered to see how well the models can reproduce the transmission spectra of a ground glass diffuser. The geometry of the Sobolev-Kokhanovsky problem is similar to Hapke's. However, here the received radiation is not confined to reflectance angles as emittance angles greater than 90° that characterize transmission are

allowed in this model.

The Sobolev-Kokhanovsky method and Hapke's model differ in parameter space. The thin-layer approximation of Sobolev-Kokhanovsky solves for: ω, τ, and $p(g)$ leaving three of Hapke's parameters (θ, B_0, and h) unknown. This may not be a hinderance as the single scattering albedo, opacity, and the phase function are a great start to characterizing the optical properties of a material.

The derivation following Kokhanovsky (2002) begins with a simplified version of the radiative transfer equations, after works like, Ishimaru (1978), among others, stating:

$$\sigma_{ext}^{-1}(\vec{n}, \vec{\nabla}) I_t(\vec{r}, \vec{n}) = -I_t(\vec{r}, \vec{n}) + \frac{\omega_o}{4\pi} \int_{4\pi} p(\vec{n}, \vec{n}') I_t(\vec{r}, \vec{n}') \, \mathrm{d}\Omega' + B_o(\vec{r}, \vec{n}) \tag{4.11}$$

Where the extinction coefficient multiplied by the single scattering albedo equals the scattering coefficient, i.e. $\sigma_{ext} \cdot \omega = \sigma_{sca}$, $p(\vec{n}, \vec{n}')$ is the phase function, and $\vec{n}$ and $\vec{r}$ are the vectors from the illumination point to the observer and the direction of the incident radiation I_t respectively. $B_o(\vec{r}, \vec{n})$ are the internal sources of radiation, assumed to be zero.

This equation further simplifies for plane parallel light coming from a collimated beam (Chandrasekhar, 1950; Sobolev, 1956; van de Hulst, 1980) to:

$$\cos\vartheta \frac{\mathrm{d}I(\tau, \vartheta, \vartheta_o, \phi)}{\mathrm{d}\tau} = -I(\tau, \vartheta, \vartheta_o, \phi) + B(\tau, \vartheta, \vartheta_o, \phi) \tag{4.12}$$

Where the source function:

$$B(\tau, \vartheta, \vartheta_o, \phi) = \frac{\omega}{4\pi} \int_0^{2\pi} \mathrm{d}\phi' \int_0^{\pi} I(\tau\vartheta, \vartheta_o, \phi) p(\theta') sin(\vartheta') \, \mathrm{d}\vartheta' + \frac{\omega I_o}{4} p(g) e^{-\tau/\cos\vartheta_o} \tag{4.13}$$

Where ϑ_o is the angle of incident radiation, and ϑ, and ϕ are the elevation and azimuth

of the observation point. $p(g)$, ω, and τ are as before and πI_o is the net flux per unit area incident the sample. For optically thin layers, $\tau \to 0$, and the analytical solution to the source function reduces to:

$$B(\tau, \vartheta, \vartheta_o, \phi) = \frac{I_o \omega p(g)}{4} e^{-\tau/\xi} \tag{4.14}$$

Where ξ is the magnitude of the cosine of the angle of the incident radiation.

Further, if the diffuse upward and downward intensities are defined for a homogeneous layer, in Sobolev (1956) as:

$$I_{\uparrow}^{d} = \frac{\omega I_o \xi}{4(\mu + \xi)} \{1 - e^{-\tau_o(1/\mu + 1/\xi)}\} p(g) \tag{4.15}$$

$$I_{\downarrow}^{d} = \frac{\omega I_o \xi}{4(\mu - \xi)} \{e^{-\tau_o/\mu} - e^{-\tau_o/\xi}\} p(g) \tag{4.16}$$

when $\mu \neq \xi$ and as

$$I_{\downarrow}^{d} = \frac{\omega I_o \tau_o}{4\mu} e^{-\tau_o/\mu} p(g) \tag{4.17}$$

when $\mu = \xi$. Where μ is the cosine of the emission angle. Then, the reflection and transmission functions for thin films can be written as: $R = I_{\uparrow}^{d}/(\xi I_o)$ and $T = I_{\downarrow}^{d}/(\xi I_o)$, such that:

$$R(\tau_o, \mu, \xi, \phi) = \frac{\omega p(g)}{4(\mu + \xi)} \{1 - e^{-(1/\mu + 1/\xi)\tau}\} \tag{4.18}$$

$$T(\tau_o, \mu, \xi, \phi) = \frac{\omega p(g)}{4(\mu - \xi)}\{e^{-\tau/\mu} - e^{-\tau/\xi}\} \tag{4.19}$$

As was the case with the Hapke BRDF, it is common to retrieve the fit parameters in the Sobolev-Kokhanovsky equations through inversion using a PSO routine.

4.8.2.1 Sobolev-Kokhanovsky Trasmittance of Optically Thin Films

Using a particle swarm optimization (PSO) code, I was able to retrieve ω, τ and the parameters b and c for the 2-term HG phase function for the Sobolev-Kokhanovsky transmittance distribution function for the case of the optically thin ground-glass diffuser. The PSO code arrives at consistent solution for the ground-glass diffuser data set, and achieves an $R^2 = 0.9987$. Figure 4.9 compares the observed and modeled data, while Figure 4.10 shows the 2-term HG phase function.

The PSO outputs: $\omega = 1$, $\tau = 7.9181$, $b = 0.81326$, and $c = -1.0022$. These are calculated for a 20 nm waveband centered at $\lambda = 780$ nm. $\omega \to 1$ is expected as it makes sense for a diffuser to scatter all the incoming light as opposed to absorbing any. The high value of τ is due to the nature of the ground-glass diffuser as well, as it is designed to interact with and scatter as much incoming radiation as possible. $b = 0.81326$ implies that the shape of the phase function lobes is narrow as values closer to $b = 0$ imply a more isotropic scattering phase function. $c = -1.0022$ suggest the ground-glass diffuser is highly forward scattering, which is to be expected. The asymmetry parameter for this phase function is $< \cos g >= -bc = -0.8150$.

While the investigation using the ground-glass diffuser is promising, this simplified model

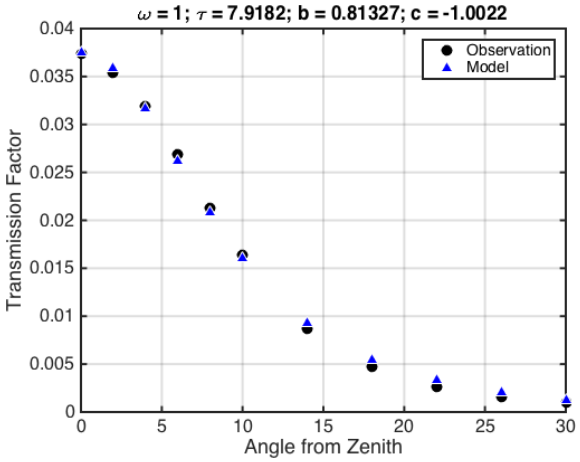

Figure 4.9: ***Sobolev-Kokhanovsky Transmission: Ground-Glass Diffuser***

Comparison between the data and the Sobolev-Kokhanovsky thin film transmittance model for the ground-glass diffuser. The models' quality of fit is: $R^2 = 0.9987$. *The modeled parameters are shown at the top.*

was unable to retrieve the parameters for our dataset as the martian regolith analogs and crystalline rock samples can not be treated as thin films. The majority of the light incident on all the samples in the catalog at the thicknesses observed is reflected into the lower hemisphere, an area inaccessible to the mini-goniometer.

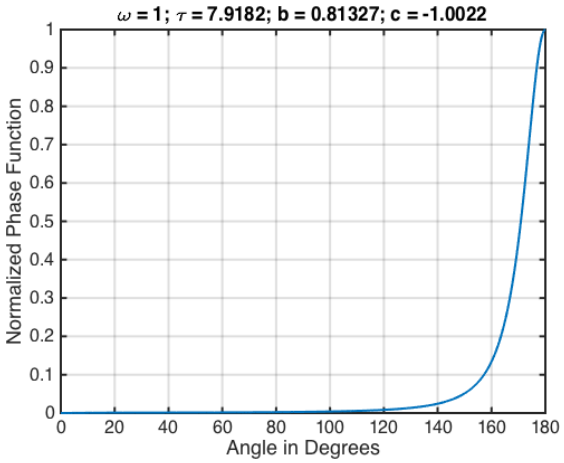

Figure 4.10: ***Sobolev-Kokhanovsky Phase Function: Ground-Glass Diffuser***

Two term Henyey-Greenstein Phase Function for the ground-glass diffuser with $b = 0.81326$ *and* $c = -1.0022$*, from Sobolev-Kokhanovsky equations. The peak at* 180° *means the ground-glass diffuser is highly forward scattering.*

5 Transmission of Radiation through Regolith

The catalog of martian regolith analogs belonging to the Planetary Volatiles Laboratory far outnumber the samples assessed in this project. Many of the thinnest samples were too optically thick to distinguish a transmission signal over noise even with a 300 W arc-lamp and highly sensitive spectrometers. Nevertheless, five different regolith analogs have been assessed to understand how radiation propagates as a function of scattering angle.

This chapter discusses the results obtained from this study for basalt, calcite, cheto bentonite, kieserite and JSC Mars-1, as well as provide a discussion on the implications of these findings. For a complete list of samples, grain sizes and observations see Appendix D Section D.1. See Figures 5.1 and 5.2 for images of the regolith analogs included in this study. The results for each analog is shown as the percent transmittance as a function of wavelength (in the case of zenith transmittance) and as a function of scattering angle for UVA (315 - 400 nm), UVB (280 - 315 nm) and the photosynthetically active region (PAR; 400 - 700 nm) wavelengths.

The transmittance is defined as the ratio of the amount of radiation emitted from the sample to the amount of radiation incident the sample, multiplied by 100, to obtain a percent. Transmittance as a function of wavelength, for nadir observations, are determined

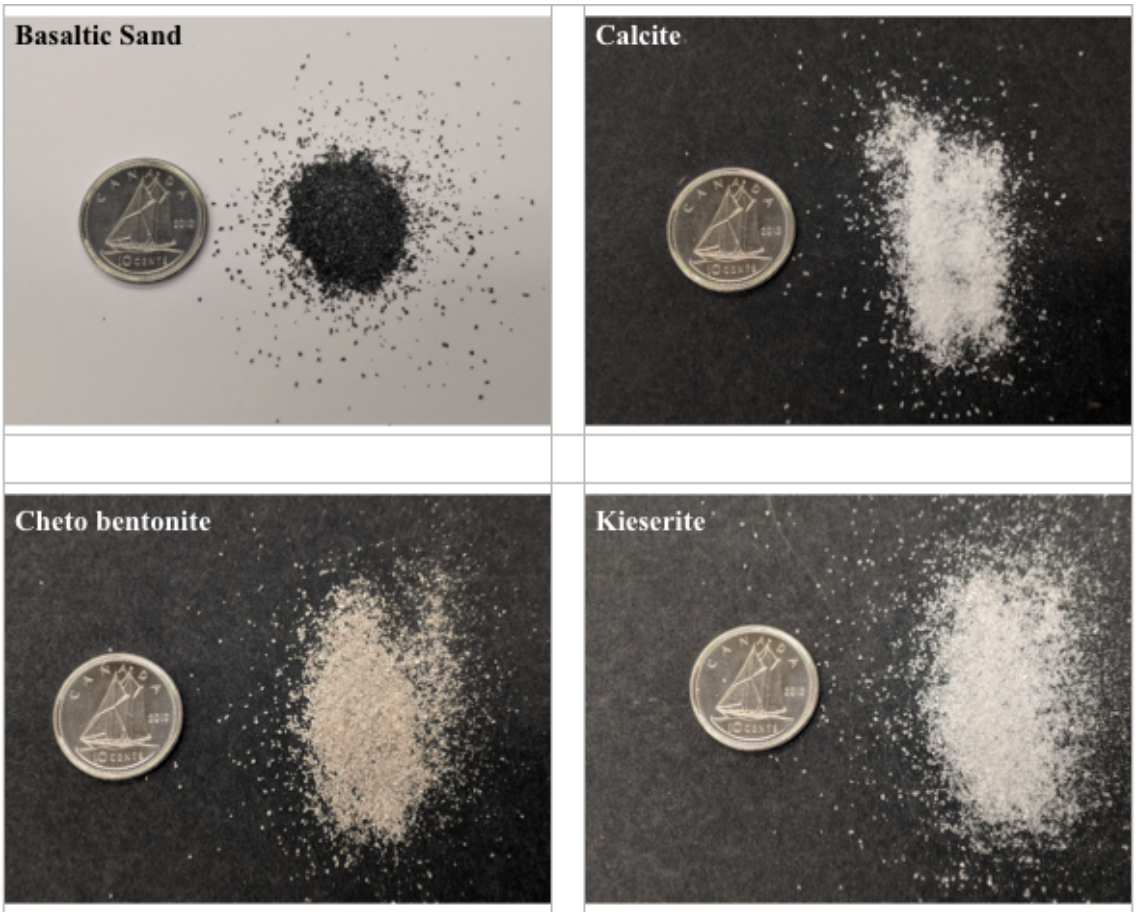

Figure 5.1: ***Non-JSC Mars-1 Analogs***

Piles of basaltic sand (top left), calcite (top right), cheto benotnite (bottom left) and kieserite (bottom right) are placed next to a Canadian dime. These images are shown to give the reader a visual of the analogs assessed in this body of work. Background color was chosen to enhance visibility of the analogs.

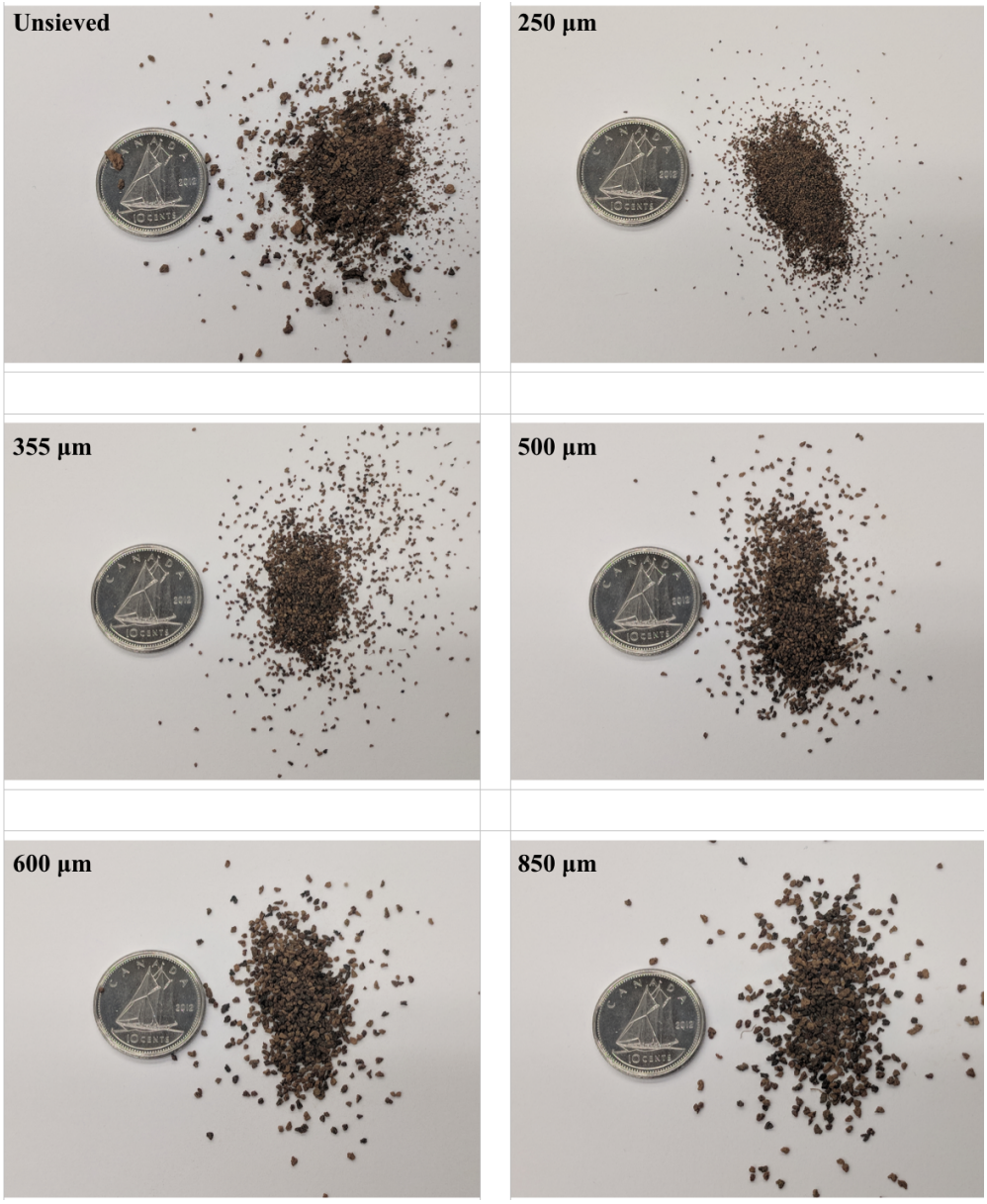

Figure 5.2: ***JSC Mars-1 Analogs***

Piles of JSC Mars-1 at several grain sizes: unsieved (top left), 250 µm (top right), 355 µm (middle left), 500 µm (middle right) 600 µm (bottom left) and 850 µm (bottom right), are placed next to a Canadian dime. These images are shown to give the reader a visual of the analogs assessed in this body of work.

for the average zenith spectrum generated by taking the mean of all such observations. Transmittance as a function of scattering angle is determined by first creating an azimuthally averaged spectrum for each scattering angle. Then the ratio of the cumulative radiation received by the spectrometer is taken with respect to the cumulative radiation incident the sample for each wavelength band, for each scattering angle considered, again multiplied by 100 to obtain a percent transmittance.

A discussion will follow the results to compare and contrast any similarities or differences seen between the different regolith analogs, as well as provide additional analysis on the kieserite sample. This chapter concludes with some final thoughts on how this experiment can be modified to increase the number of analogs capable of being studied with this setup.

5.1 Results

5.1.1 Basalt

The catalog of martian regolith analogs in the laboratory include pulverizing basaltic rocks, herein referred to as basaltic sands. These basaltic sands come in two broadly defined grain size fractionations, fine grain and medium grain, as well as an unsieved variant. Only the medium grain size sample of basaltic sand was capable of being assessed by the mini-goniometer setup and only at a thickness of 0.5 mm. The fine grain and unsieved varieties of basaltic sand proved to be too optically thick at the thinnest sample size preparation, producing a signal that could not be discerned from noise. Likewise, at a thickness of 1.0 mm, the medium grain basaltic sand sample was too optically thick to assess.

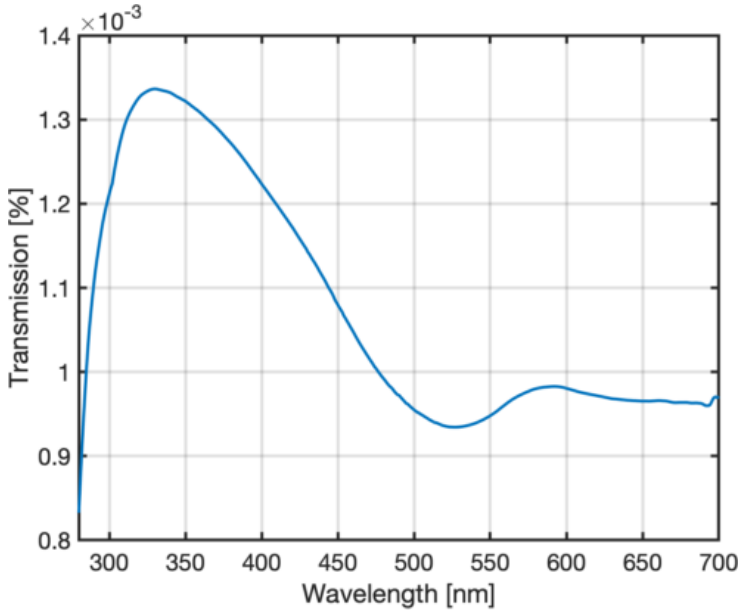

Figure 5.3: ***Basaltic Sand: Transmission as a Function of Wavelength***

Average zenith transmission through a thickness of 0.5 mm of basaltic sand as a function of wavelength.

The average zenith transmission spectrum as a function of wavelength for medium grain basaltic sand at a thickness of 0.5 mm can be seen in Figure 5.3. From the plot it is evident that this grain size of basaltic sand is more transparent to UV wavelengths compared to visible wavelengths. Also of note is the strange behavior at around 575 nm. This is where the data from the two spectrometers meet, and it appears they behave slightly differently for this sample. At first this was worrisome, foreshadowing an error in the analysis, however all other samples show a smooth transition from the UV to the NIR spectrometer in this region.

UVA, UVB and PAR transmittance as a function of scattering angle can be seen in Figure

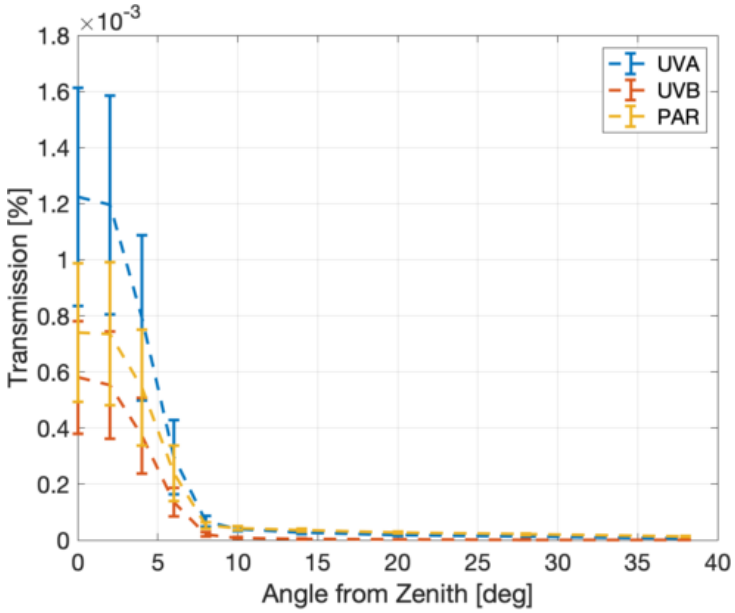

Figure 5.4: ***Basaltic Sand: Transmission versus Scattering Angle***

UVA, UVB and PAR transmittance of basaltic sand shown as a function of scattering angle from zenith for a sample thickness of 0.5 mm. Error bars are the 95% confidence interval.

5.4. All three wavelength bandpasses show a similar profile, akin to the opposition surge seen in reflectance data. Here, it can be thought of as the majority of radiation scattering through the a sample of medium grain basaltic sand is scattered in forward directions.

5.1.2 Calcite

The catalog of martian regolith analogs in the laboratory has one sample of calcite, which is classified as medium grain. This sample, like those before it was unable to provide useable data at a thickness of 1.0 mm and has hence only been assessed at 0.5 mm in thickness.

The average zenith transmission spectrum of calcite can be seen in Figure 5.5 as a function

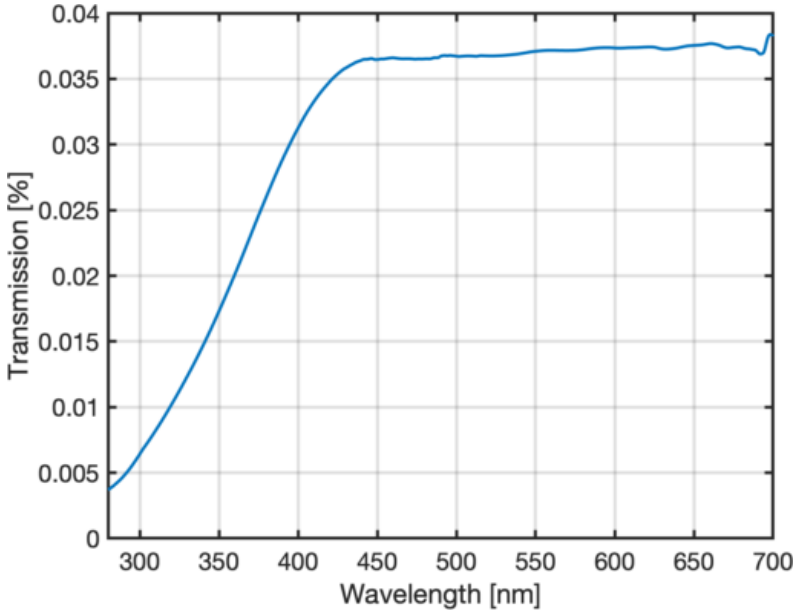

Figure 5.5: ***Calcite: Transmission as a Function of Wavelength***

Average zenith transmission through a thickness of 0.5 mm of Calcite as a function of wavelength.

of wavelength. The PAR transmittance is relatively constant throughout the wavelength bandpass, while an exponential decrease in the transmittance is seen for wavelengths in the UVA and UVB bandpasses.

UVA, UVB and PAR transmittance as a function of scattering angle can be seen in Figure 5.6. PAR transmittance is roughly 3× that of UVB transmittance for all scattering angles, and the transmittance in all three wavelength bandpasses does not vary wildly with an increased scattering angle.

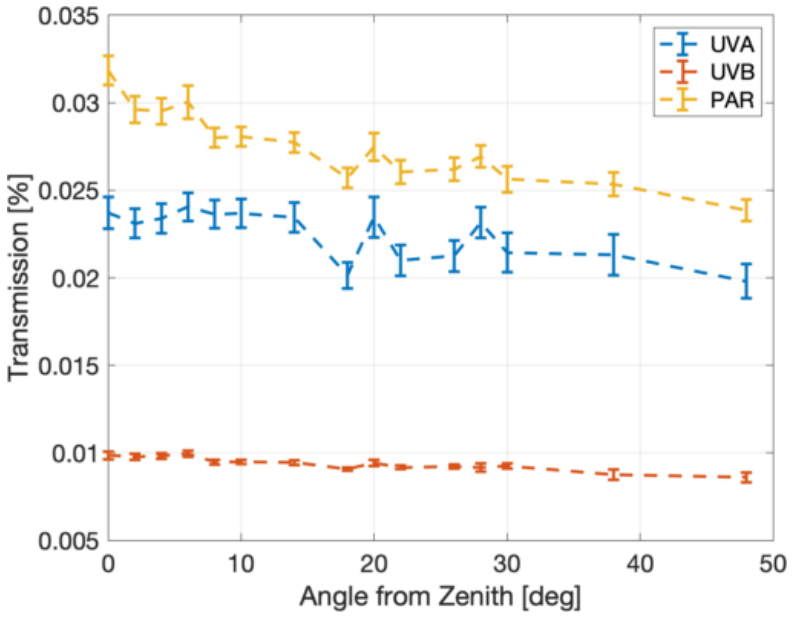

Figure 5.6: ***Calcite: Transmission versus Scattering Angle***

UVA, UVB and PAR transmittance of calcite shown as a function of scattering angle from zenith for a sample thickness of 0.5 mm. Error bars are the 95% confidence interval.

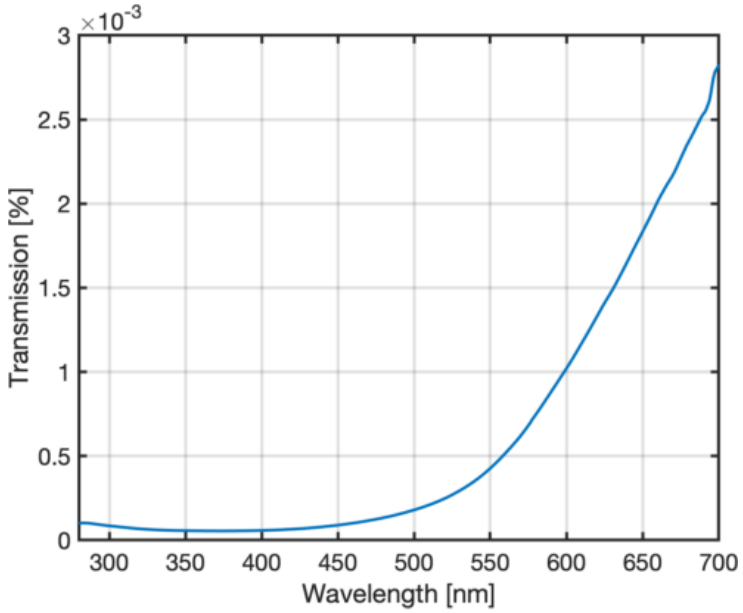

Figure 5.7: ***Cheto bentonite: Transmission as a Function of Wavelength***

Average zenith transmission through a thickness of 0.5 mm of Cheto bentonite as a function of wavelength.

5.1.3 Cheto bentonite

The catalog of martian regolith analogs in the laboratory only has one sample of cheto bentonite, which is classified as medium grain. This sample, like the basaltic sand was unable to provide useable data at 1.0 mm in thickness and has hence only been assessed for a sample prepared at a thickness of 0.5 mm.

The average zenith transmission spectrum of cheto bentonite can be seen in Figure 5.7 as a function of wavelength. Here, the concerning transition behavior seen with the basaltic sand where the data from both spectrometers meet, is absent, and the transmittance exponentially increases with increasing wavelength.

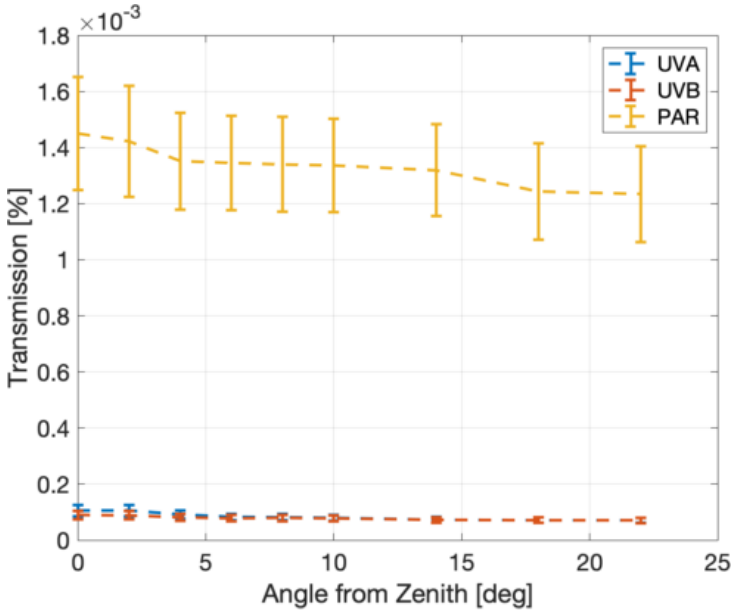

Figure 5.8: ***Cheto bentonite: Transmission versus Scattering Angle***

UVA, UVB and PAR transmittance of cheto bentonite shown as a function of scattering angle from zenith for a sample thickness of 0.5 mm. Error bars are the 95% confidence interval.

UVA, UVB and PAR transmittance as a function of scattering angle can be seen in Figure 5.8. As potentially expected from the zenith transmittance, the UVA and UVB transmittance is very low at all scattering angles considered in comparison to the PAR transmittance. Additionally, the transmittance of UVA, UVB and PAR radiation do not appear to taper off rapidly with scattering angle. PAR transmission is roughly 7× greater than those of UVA and UVB.

5.1.4 JSC Mars-1

Observations from Viking Lander 1 were used to create JSC Mars-1 using material collected from Puu Nene on the Island of Hawaii. JSC Mars-1 shares a similar reflectance spectrum, chemical composition, mineralogy, grain size, specific gravity and magnetic properties to what was observed at VL-1 site Allen et al. (1998).

Our collection of JSC Mars-1 includes samples sieved to grain sizes of: 45 μm, 90 μm, 150 μm, 250 μm, 355 μm, 500 μm, 600 μm, and 850 μm in radius as well as roughly 20 kg of unsieved, raw JSC Mars-1. However, due to the limitations of our setup, not all size fractionations were assessed. The very fine ($\leq$ 150 μm), opaque JSC Mars-1 samples were so optically thick that the spectrometers were not able to detect any transmission of radiation through the sample at a 0.5 mm thickness. See Table 5.1 for the grain sizes and sample thicknesses used in this study.

The grain sizes of JSC Mars-1 in this study are much larger than those of the other analogs and proved to be more difficult to work with. The large grain sizes made it possible for light to enter the telescope without scattering off the JSC Mars-1, this is, in retrospect, very regrettable, and was discovered after the fact. It was noticed that some of the samples that were twice as thick required twice the optical depth on the telescope for similar integration times, this can only make sense if there were regions in the prepared sample that allowed light to pass through the system without interacting with the sample first.

Contrary to the results shown for basalt, calcite, cheto bentonite and kieserite, in which all runs were compiled to produce an average spectrum, the results displayed for JSC Mars-1

JSC Mars-1	Sample Thickness		
Grain Size	0.5 mm	1.0 mm	2.0 mm
unsieved	✓		
250 μm	✓	✓	
355 μm	✓	✓	
500 μm		✓	✓
600 μm		✓	✓
850 μm		✓	✓

Table 5.1: *JSC Mars-1 Grain Size and Sample Thickness*

JSC Mars-1 grain size and sample thickness assessed with the mini-goniometer setup. Checkmarks indicate successful data retrieval.

are not averaged over all runs at the same grain size and thickness. Instead, the data from each individual run are shown which may yield some insightful observations.

5.1.4.1 JSC Mars-1: Unsieved

There were three runs for the unsieved sample of JSC Mars-1 at 0.5 mm in thickness. When collecting the data, the operator needed to use opacities of 0, 0.2 or 2.5 to not over saturate the spectrometer. This means that one run needed to attenuate the light by roughly $10^{-2.5}$ between a similar material at the same thickness. The variation in peak transmittance between the three samples cover over four orders of magnitude. Even if we discount the sample that needed 2.5 optical depth between the sample and the telescope, the difference between the transmittance seen in the samples requiring 0 and 0.2 is still two orders of magnitude. See Figure 5.9 which shows UVA, UVB, and PAR transmittance as a function of scattering angle for the three runs of the unsieved JSC Mars-1 at 0.5 mm in thickness. Note the vertical axis to see how different the total transmission through each sample varies.

Though the transmittance between the samples varies considerably, there are some commonalities seen here and with other JSC Mars-1 specimens. Notice that UVA transmits through all three samples at a rate of 2-3× more than UVB and PAR radiation for angles close to zenith. The UVB and PAR transmittance is also very similar to one another in two of the three runs. Two samples had peak transmission off of zenith – which might point one to assume that there may have been an alignment issue, but this is not observed in the relevant ground glass diffuser runs. It most likely is an effect of different packing efficiencies

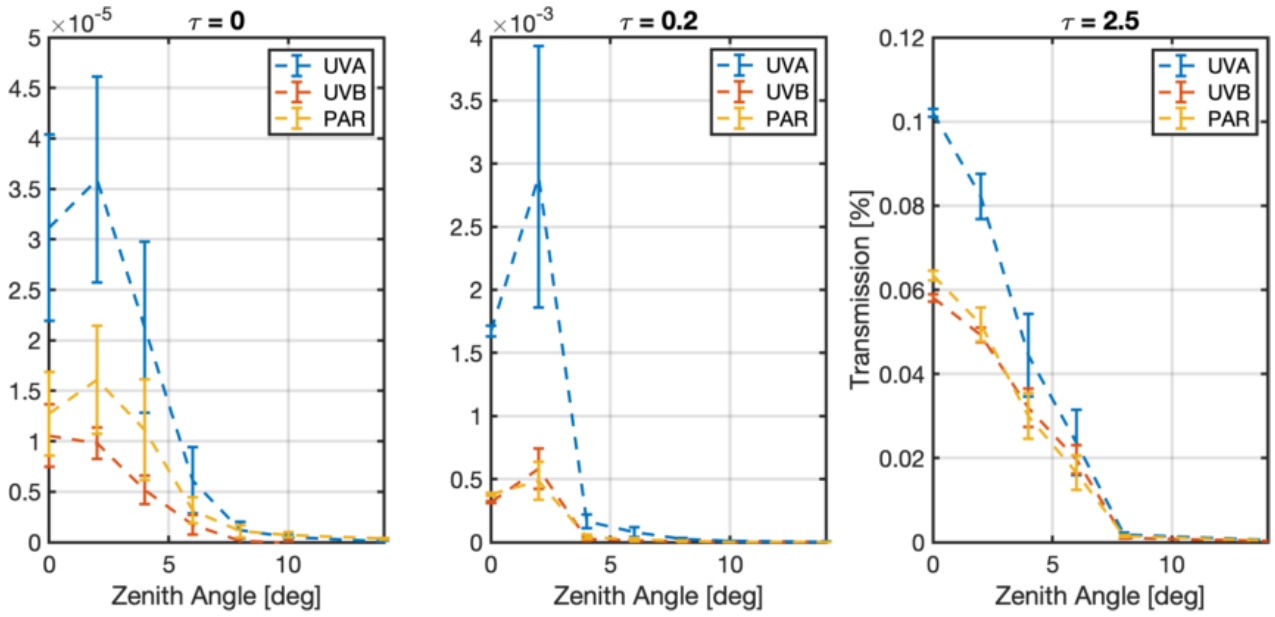

Figure 5.9: ***JSC Mars-1 (Unsieved): Transmission versus Scattering Angle***

UVA, UVB and PAR transmittance for three runs of the unsieved variety of JSC Mars-1 at 0.5 mm in thickness shown as a function of scattering angle from zenith. Note the large discrepancies between the transmittance for the same sample prepared different ways, but also note how all three show a similar profile and that UVA transmittance is much larger than UVB and PAR for angles near zenith. Error bars are the 95% confidence interval.

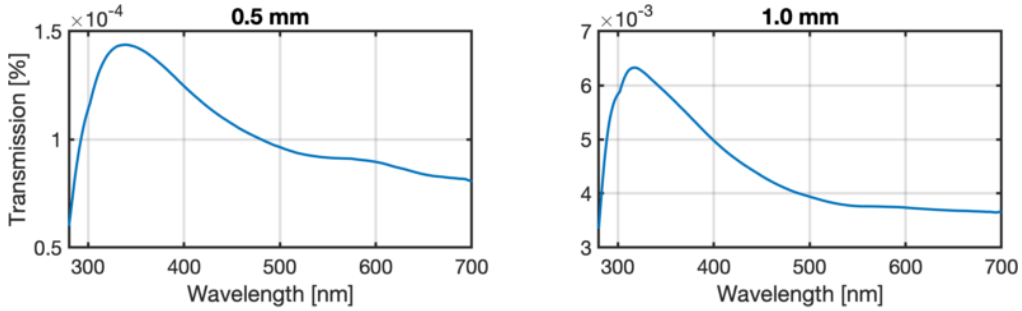

Figure 5.10: ***JSC Mars-1 (250 μm): Transmission as a Function of Wavelength***

Average zenith transmission through JSC Mars-1 (250 μm) as a function of wavelength for sample thicknesses of 0.5 mm and 1.0 mm.

between the three runs. Nevertheless, all three samples exhibit a near-gaussian transmission function with respect to scattering angle, suggesting that regardless of the total amount of light transmitting the sample, it is mostly in the forward direction.

5.1.4.2 JSC Mars-1: 250 μm

There are a total of six datasets for the 250 μm grain size JSC Mars-1. Three conducted at each thickness of 0.5 mm and 1.0 mm. The transmittance as a function of wavelength for the average zenith spectra is computed and shown in Figure 5.10 for the two sample thicknesses. Notice the vertical axis, implies that by doubling the sample thickness, two orders of magnitude more light is allowed to pass through the sample.

This clearly suggests a flaw in the procedures to prepare the samples and highlights the necessity to both increase the number of runs done at each thickness and to conceive of a more uniform way to prepare the packed regolith samples in order to achieve an average

spectrum that is characteristic of JSC Mars-1 at these larger grain sizes and thicknesses.

The UVA, UVB and PAR transmittance as a function of scattering angle is shown in Figure 5.11 for each individual run, note how the transmittance ranges by 4 orders of magnitude for the 1.0 mm sample, while the samples at a thickness of 0.5 mm only differ by about 1 order of magnitude.

5.1.4.3 JSC Mars-1: 355 μm

There are a total of six datasets for the 355 μm grain size JSC Mars-1. Three conducted at each thickness of 0.5 mm and 1.0 mm. These samples also exhibited the seemingly paradoxical positive relationship between transmission and sample thickness, with the 1.0 mm sample showing some of the largest transmission seen thus far in this study.

The data is treated the same way as the 250 μm data, with Figure 5.12 showing the zenith transmission as a function of wavelength and Figure 5.13 showing UVA, UVB, and PAR transmittance as a function of scattering angle.

What is interesting here is that as shown in Figure 5.12 the zenith transmittance profiles do not exhibit the same shape between the two thicknesses, which was mostly consistent between the sample thicknesses for the 250 μm JSC Mars-1 as seen in Figure 5.10. Also note the large spikes in transmittance at $\sim$430 nm and $\sim$550 nm, these are due to exposure times on this sample exceeding several seconds and are artifacts of the lighting conditions within the laboratory at the time the spectra were collected.

Figure 5.13 shows that the UVA, UVB and PAR transmittance with angle is much more

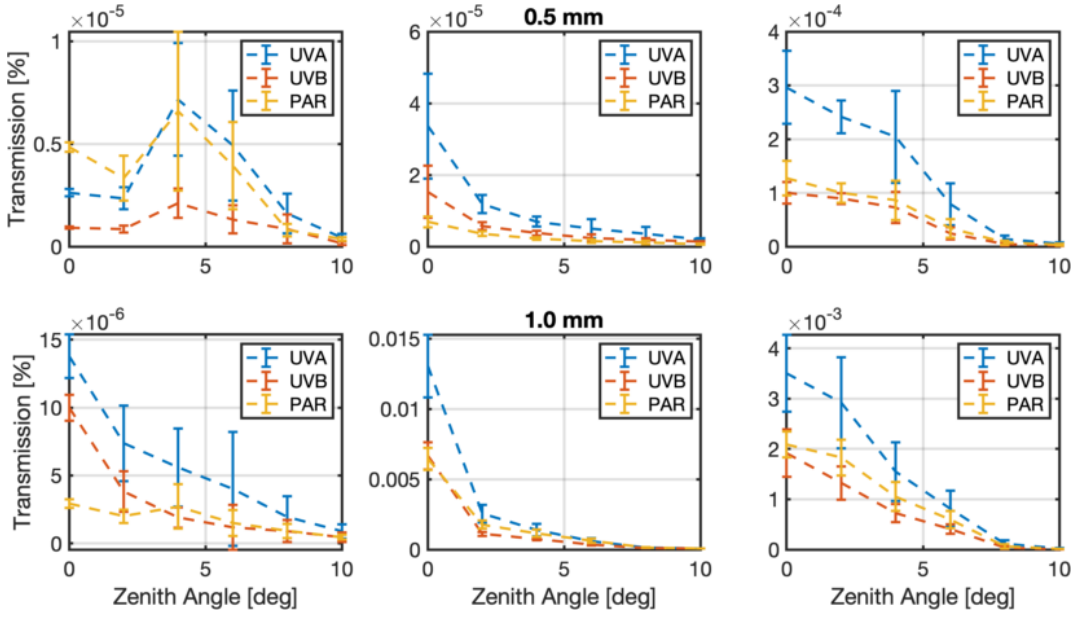

Figure 5.11: ***JSC Mars-1 (250 μm): Transmission versus Scattering Angle***

UVA, UVB and PAR transmittance for 6 runs of the 250 μm grain size of JSC Mars-1 at 0.5 mm (top row) and 1.0 mm (bottom row) in thickness shown as a function of scattering angle from zenith. Note the large discrepancies between the transmittance for the same sample prepared different ways, but also notice how the six plots show a similar profile and that UVA transmittance is much larger than UVB and PAR for angles near zenith for five of the six samples. Error bars are the 95% confidence interval.

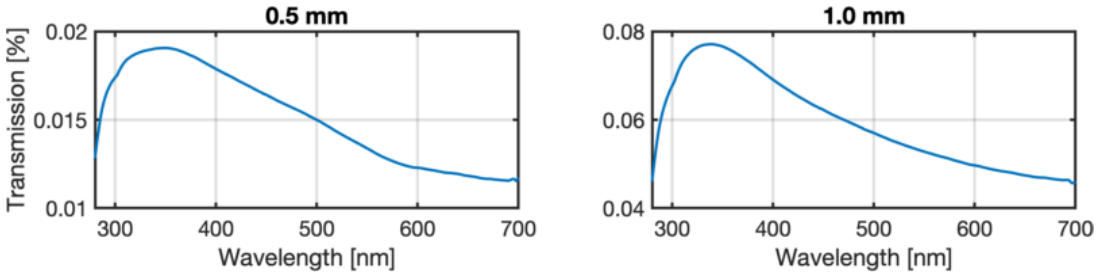

Figure 5.12: ***JSC Mars-1 (355 μm): Transmission as a Function of Wavelength***

Average zenith transmission through JSC Mars-1 (355 μm) as a function of wavelength for sample thicknesses of 0.5 mm and 1.0 mm.

uniform between the runs in the 1.0 mm case as compared to that of the 0.5 mm samples, which is somewhat similar to that seen in the 250 μm JSC Mars-1.

5.1.4.4 JSC Mars-1: 500, 600, 850 μm

The largest grain sizes in the study were only examined multiple times at a thickness of 1.0 mm. These grain sizes exhibited uniform zenith transmittance as a function of wavelength, as well as some of the smallest variations in transmittance between samples of identical same grain size, with variations of around 2×, 6×, and 2× for the 500, 600 and 850 μm grain sizes respectively.

The mean zenith transmittance as a function of wavelength for the three grain size fractionations can be seen in Figure 5.14 and the UVA, UVB and PAR transmission with respect to scattering angle can be seen in Figure 5.15.

In all instances, the UVA transmittance is greatest near zenith, and UVB and PAR transmittance tend to be similar to one another in all trials. The shape of the transmission

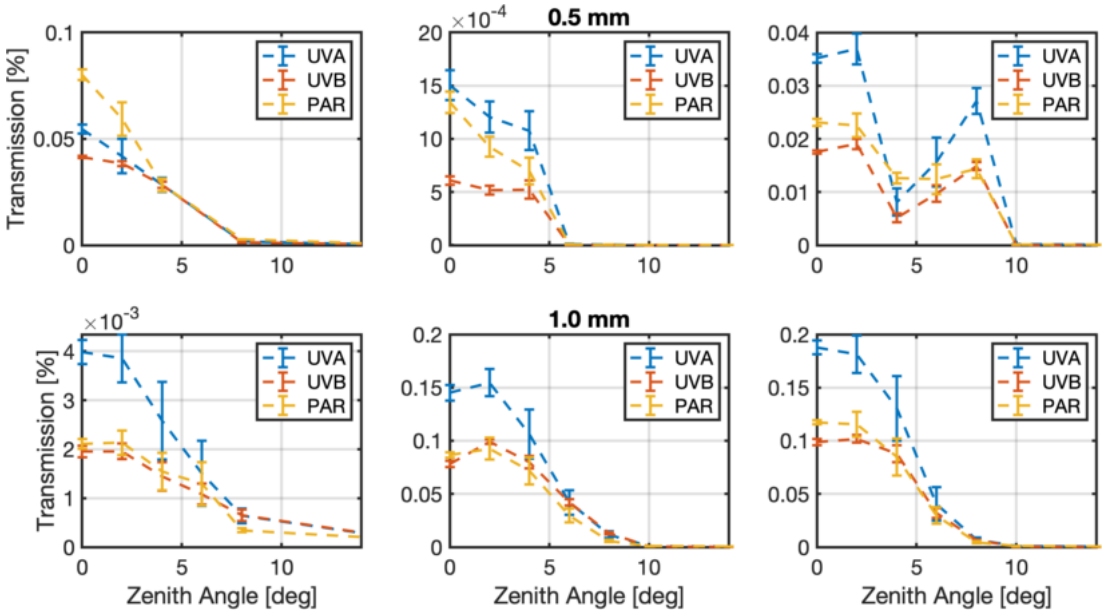

Figure 5.13: ***JSC Mars-1 (355 μm): Transmission versus Scattering Angle***

UVA, UVB and PAR transmittance for 6 runs of the 355 μm grain size of JSC Mars-1 at 0.5 mm (top row) and 1.0 mm (bottom row) in thickness shown as a function of scattering angle from zenith. Note the large discrepancies between the transmittance for the same sample prepared different ways, but also notice how five out of the six plots show a similar profile and that UVA transmittance is much larger than UVB and PAR for angles near zenith for five of the six samples. Error bars are the 95% confidence interval.

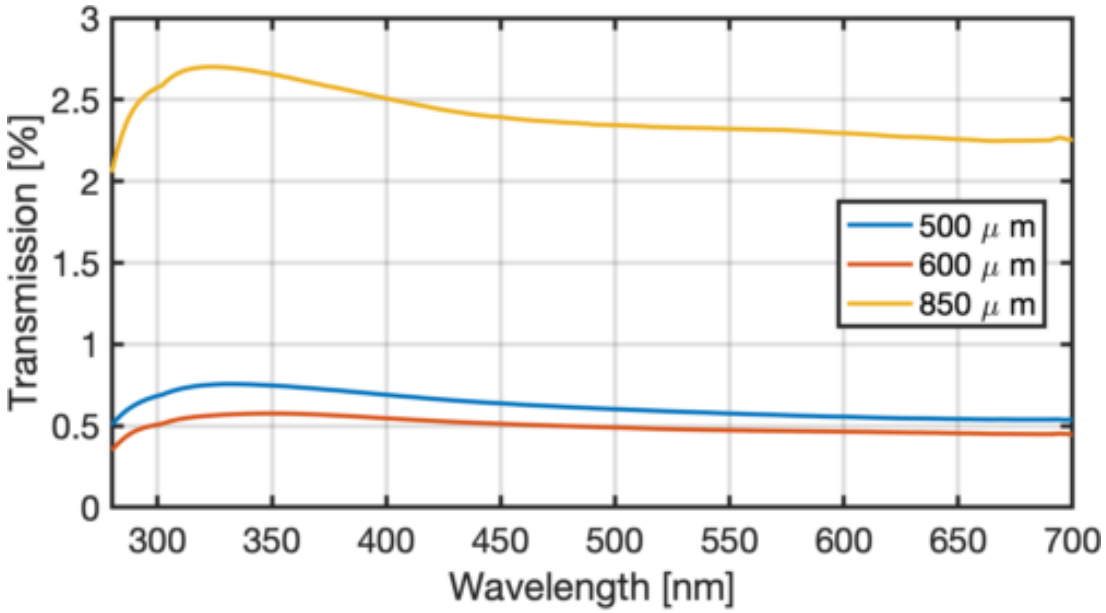

Figure 5.14: ***JSC Mars-1 ($\geq$ 500 μm): Transmission as a Function of Wavelength***

Average zenith transmission through JSC Mars-1: 500 μm, 600 μm, 850 μm as a function of wavelength for sample thicknesses 1.0 mm. While the profiles look similar to one another it is curious that the 600 μm sample was less than the 500 μm samples.

profiles are also much more uniform than previous grain sizes. This could be due the larger size of the grains making it all but impossible to create a 1.0 mm layer of material that inhibit photons to be received by the telescope without interacting with the sample materials.

Not shown here are the runs conducted at a thickness of 2.0 mm. There was only one run done for each grain size and as expected the transmittance decreased as sample thickness increased. Since variations existed in the 1.0 mm thick samples, its plausible to assume that variations would also be seen in the 2.0 mm thick samples, as such, it is not appropriate to attempt investigations describing the extinction of UVA, UVB and PAR radiation into these samples.

5.1.5 Kieserite

The catalog of martian regolith analogs in the laboratory only has one sample of kieserite, which is classified as medium grain. Kieserite is visually much more translucent than the samples before it, see Figure 5.1. The combination of its translucence and its relatively uniform grain size made it an ideal sample to analyze at two thicknesses.

The average zenith transmission spectrum of kieserite can be seen in Figure 5.16 as a function of wavelength for sample thicknesses of 0.5 mm and 1.0 mm. As expected, the transmittance as a function of wavelength between the two sample thicknesses are quite similar in shape, with the overall transmittance of the 1.0 mm sample being less than that of the 0.5 mm sample.

UVA, UVB and PAR transmittance as a function of scattering angle can be seen in Figure

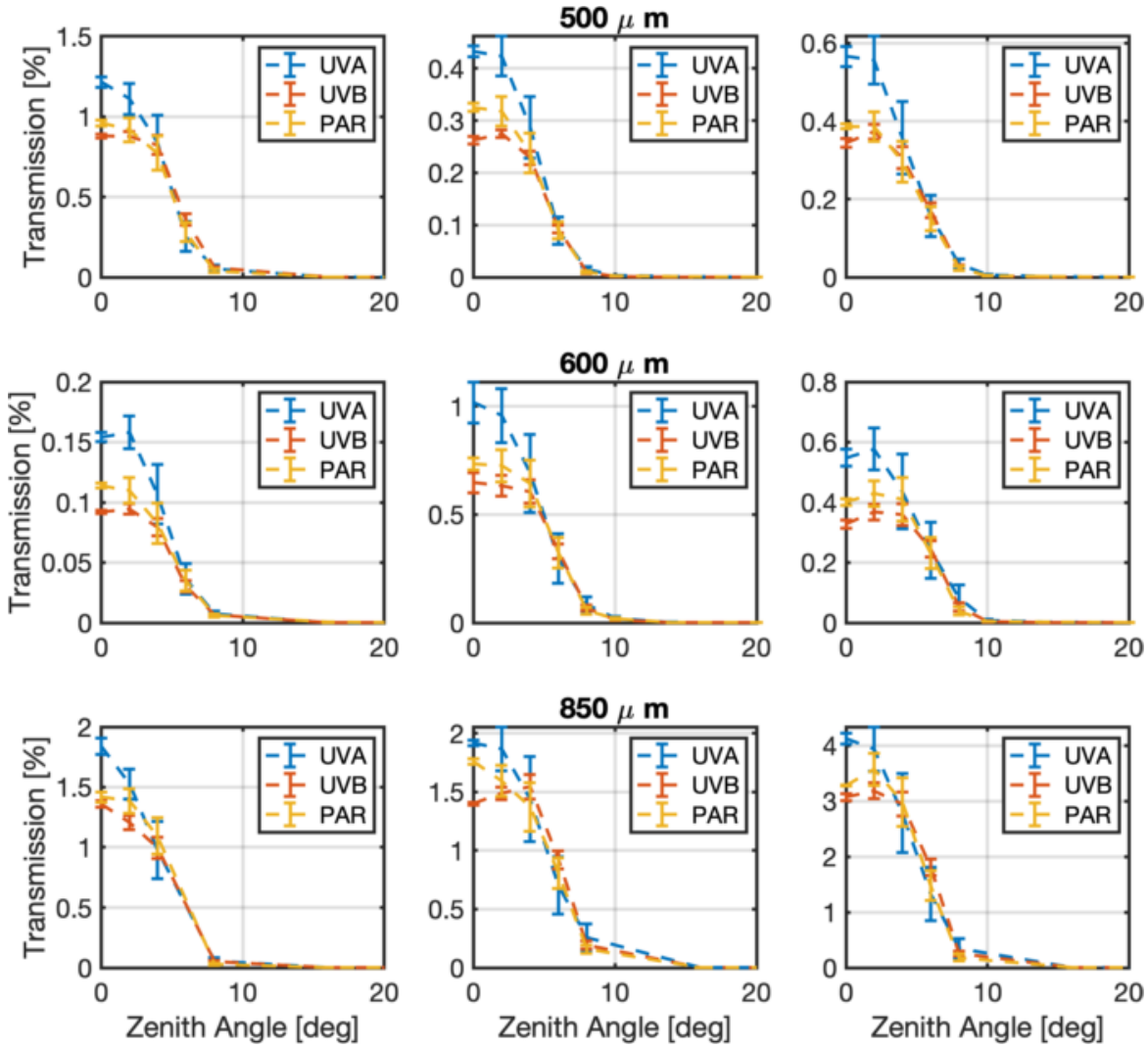

Figure 5.15: ***JSC Mars-1 (≥ 500 μm): Transmission versus Scattering Angle***

UVA, UVB and PAR transmittance for 9 runs of the larger grain sizes of JSC Mars-1 at 1.0 mm in thickness shown as a function of scattering angle from zenith. Grain sizes of: 500 μm (top row), 600 μm (middle row), and 850 μm (bottom row). Note the large discrepancies between the transmittance for the same sample prepared different ways, yet nearly all have the same transmission profile with regards to scattering angle and UVA, UVB, PAR transmittance. Error bars are the 95% confidence interval.

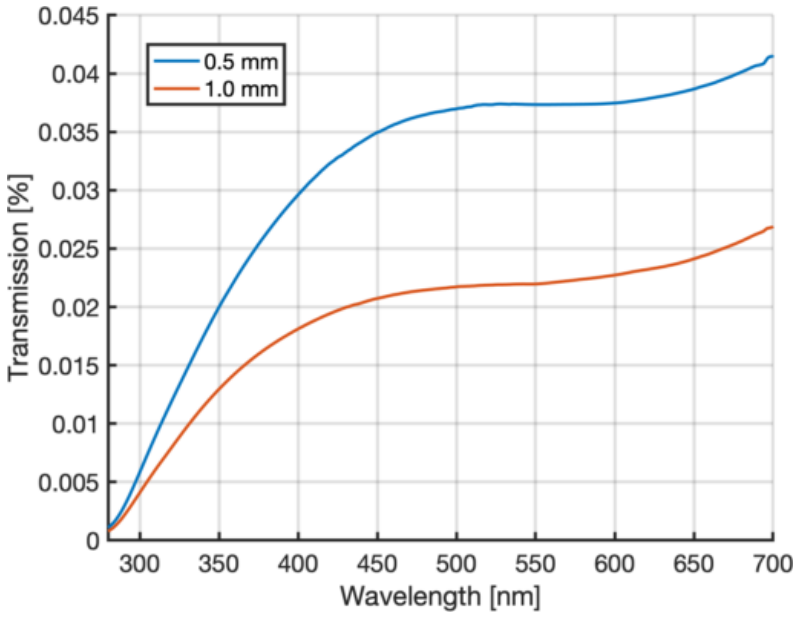

Figure 5.16: ***Kieserite: Transmission as a Function of Wavelength***

Average zenith transmission through two thicknesses of kieserite as a function of wavelength.

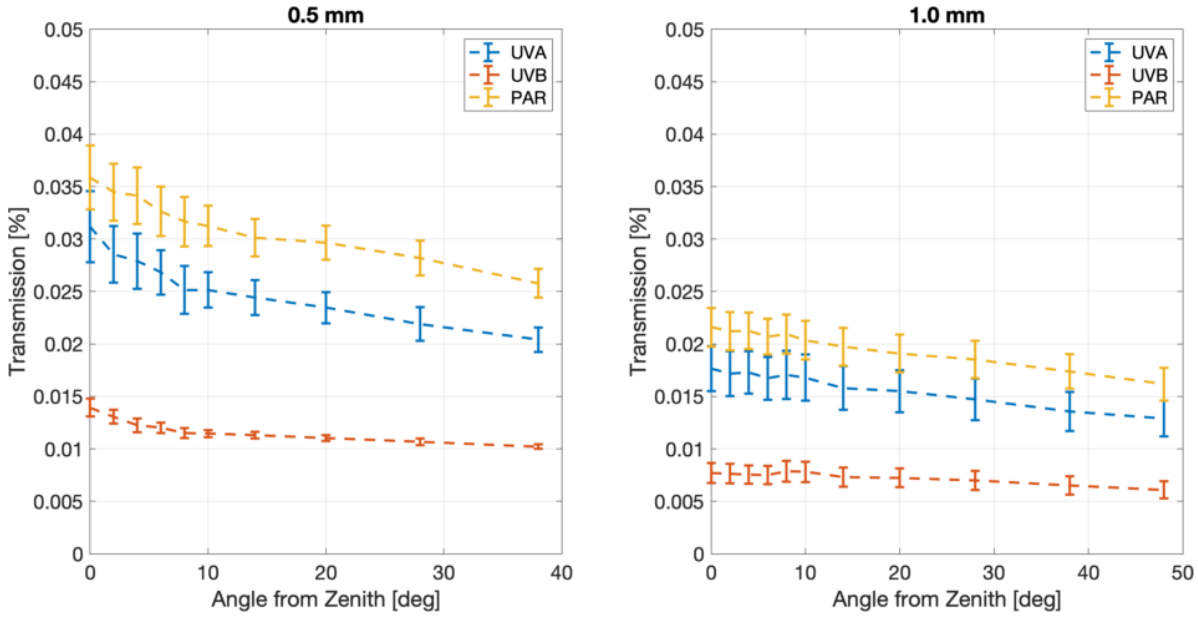

Figure 5.17: ***Kieserite: Transmission versus Scattering Angle***

UVA, UVB and PAR transmittance of kieserite shown as a function of scattering angle from zenith. The left plot is for a depth of 0.5 mm and the right plot is for a depth of 1.0 mm. Error bars are the 95% confidence interval.

5.17 for both sample thicknesses. Both samples show a near linear fall off of UVA, UVB and PAR transmittance with scattering angle, with the transmission in the 1.0 mm sample, being, as expected, more attenuated than the thinner sample preparation.

5.2 Discussion

5.2.1 Ultraviolet Radiation: Transmitters versus Quenchers

By examining the zenith transmittance as a function of wavelength, it is possible to classify the five materials into UV transmitters and UV quenchers. As the names suggests, UV

transmitters are materials that favor transmittance of UV wavelengths compared to PAR, while the UV quenchers are materials that effectively block UV radiation from propagating into the subsurface.

The basaltic sand and JSC Mars-1 materials exhibit transmission profiles that favor the transmittance of UV radiation compared to PAR. This can be seen in Figure 5.3 for basalt and in Figure 5.14, for JSC Mars-1. For both materials, the peak transmittance is seen in the 300-350 nm wavelength band with a steep drop in transmittance as wavelengths increase. The wavelength dependence between the two materials is not identical as the basaltic sand appears to begin increasing its transmittance at around 550 nm in the PAR wavelength band. This is not seen in any of the JSC Mars-1 samples, which appear to asymptotically approach a similar value as wavelength increases.

Calicte, cheto bentonite and kieserite all exhibit transmission profiles that favor the transmittance of PAR wavelengths compared to UV wavelengths, to varying degrees. This is readily seen in Figures 5.5, 5.7, and 5.16 for calcite, cheto bentonite and kieserite, respectively. The transmittance of UV photons in the calcite and kieserite samples increase rapidly with increased wavelengths, with the transmittance at 400 nm is close to 8$\times$ and 3.5$\times$ higher than the transmittance at 280 nm for the respective samples. These two samples also differ in that the calcite continues to increase its transmittance to roughly 450 nm before tapering off for larger wavelengths, whilst in the kieserite sample transmittance continues to increase with increased wavelength throughout the PAR region, albeit at a less aggressive rate than that seen in UV wavelengths.

Cheto bentonite is in a category of its own when it comes to UV quenching. This sample exhibits extremely low and nearly identical transmittances throughout the UV wavelength bandpasses whilst the transmittance exponentially increases with wavelength in the PAR wavelengths. The transmittance in cheto bentonite at 700 nm is roughly 30× than that at 400 nm.

5.2.2 Forward versus Isotropic Scatterers

The transmittance as a function of scattering angle for the five samples presented here can be categorized into two groups. Those that primarily scatter in the forward direction and those that tend to scatter more uniformly with increased observation angles.

Basaltic sand and the JSC Mars-1 appear to favor forward scattering, this can be seen in Figure 5.4 for basalt and Figure 5.15, for JSC Mars-1. For both materials, peak transmittance occurs near zenith and a sharp fall-off of transmittance is seen as the scattering angle approaches 10° off of zenith. This behavior is reminiscent of the opposition surge seen in reflectance measurements occurring at a scattering angle of 180°. Since the majority of the radiation transmitting through basalt and JSC Mars-1 is in the forward direction, the zenith transmittance is a good estimate of the total amount of light scattered into these samples.

Conversely, a more isotropic scattering phase function is seen for calcite, cheto bentonite and kieserite, Figures 5.6, 5.8, and 5.17, respectively. For these materials, the peak transmittance is still at zenith, like the basaltic sand and JSC Mars-1, however as the scattering angle increases, the transmittance falls off much less rapidly. As an example, the transmit-

tances of kieserite differ by roughly 40% between peak transmittance at 0° and 48° for the 1.0 mm sample. It is fair to say that for these samples, the zenith transmittance is not a good estimate of the total amount of light scattered into these samples, as transmitting radiation is scattered into the entire forward hemisphere and not just points close to zenith.

5.2.3 Extinction in Kieserite

Having data for two thicknesses means it is possible to assess how light is attenuated with depth as a function of wavelength in kieserite. Figure 5.18 shows an approximated extinction coefficient as a function of wavelength from 0.5 mm to 1.0 mm in thickness.

Mathematically, this is achieved by examining the Beer-Lambert Law, which defines the transmittance as:

$$T = \frac{I}{I_o} = e^{-\tau} \tag{5.1}$$

Where I, I_o are the transmitted and incident radiation respectively, and τ is the opacity of the sample. The transmittance of the two thicknesses is thus defined as:

$$T_{0.5mm} = \frac{I_{0.5mm}}{I_o} = e^{-\tau_{0.5mm}} \tag{5.2}$$

and

$$T_{1.0mm} = \frac{I_{1.0mm}}{I_o} = e^{-\tau_{1.0mm}} \tag{5.3}$$

Recalling that the opacity is a function of thickness, that is: $\tau = \int_0^l \alpha(x)\,\mathrm{d}x$, where l is the thickness of the material and $\alpha(x)$ is the extinction coefficient with depth. If we assume

uniform extinction with depth, then $\tau = \alpha l$. Equations 5.2 and 5.3 can thus be rewritten as:

$$T_{0.5mm} = e^{-\alpha(0.5mm)} \tag{5.4}$$

and

$$T_{1.0mm} = e^{-\alpha(1.0mm)} \tag{5.5}$$

It is possible to write Equation 5.5 in terms of Equation 5.4 as:

$$T_{1.0mm} = e^{-2(\alpha(0.5mm))} = T_{0.5mm} \cdot e^{-\alpha(0.5mm)} \tag{5.6}$$

Solving for the extinction coefficient, α, yields:

$$\alpha = -\frac{1}{0.5mm} \cdot ln\frac{T_{1.0mm}}{T_{0.5mm}} \tag{5.7}$$

The average extinction for UVA, UVB and PAR wavelengths are: 0.8853 mm^{-1}, 0.6967 mm^{-1}, and 1.0090 mm^{-1}. If these values are constant with depth, it is possible to describe how the UVA, UVB, and PAR radiation are attenuated throughout a sample of any thickness. This is shown in Figure 5.19 which shows the percent transmittance as a function of depth for a direct beam of radiation into a kieserite surface. The amount of transmitted light at 1.0 mm in depth in this plot deviates slightly from the values seen in Figure 5.17 for the 1.0 mm samples, this is due to the simplicity of the model where the average extinction coefficients is used, instead of assigning the proper weighting function to the wavelengths in question.

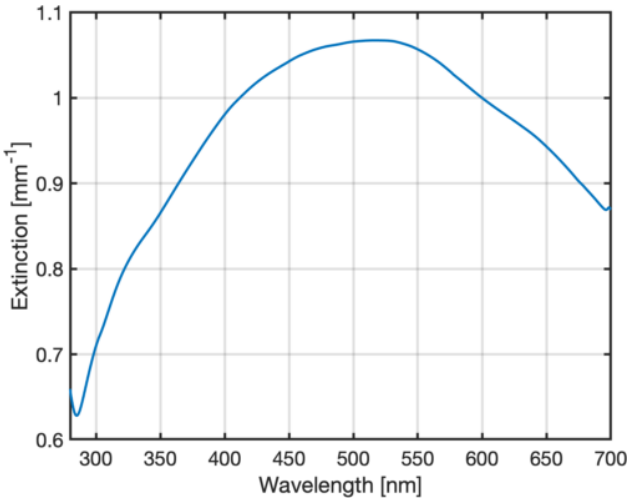

Figure 5.18: ***Kieserite: Extinction Coefficient***

The extinction coefficient for a direct beam of radiation through kieserite, shown as a function of wavelength. This was derived by comparing the direct beam transmittance between two samples of kieserite at thicknesses of 0.5 mm and 1.0 mm.

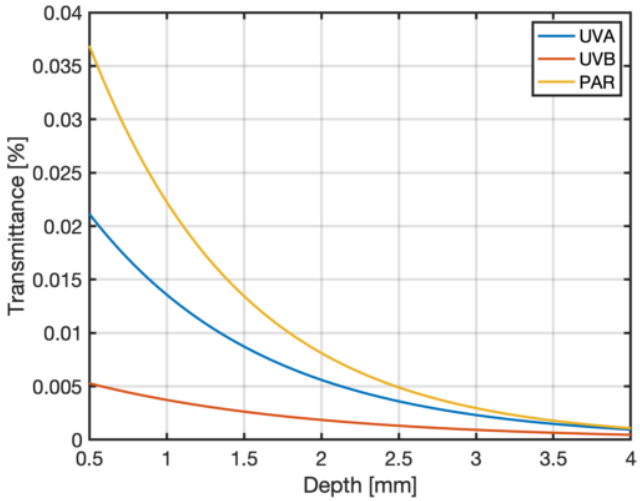

Figure 5.19: ***Kieserite: Transmittance with Depth***

Percent transmittance for UVA, UVB and PAR radiation as a function of thickness within kieserite. This is a simple exponential model that takes into account the average extinction coefficient for each of the wavelength bands.

5.3 Summary

Of the martian regolith samples analyzed, it appears that the mini-goniometer setup in its current form is most reliable for finer grained, semi-opaque samples. Samples that had a larger grain size allowed too many variation in the packing efficiency when the samples were produced. This is mostly evident in the JSC Mars-1 samples that showed a positive correlation between transmission and sample thickness. This non-uniformity makes any assessment of extinction within JSC Mars-1 as sample thickness increases unreliable. An assessment of this nature will depend on future iterations of this experiment to be able to create a more cohesive method of producing uniformly packed samples of larger grain size materials.

Additionally, if sample thicknesses less than 0.5 mm can be prepared, the smaller grain size JSC Mars-1 and other fine grain opaque samples belonging to the laboratory can be added to the catalog of materials capable of being assessed with the mini-goniometer. At larger grain sizes, increased sample thickness ($>$ 2.0 mm) would, in theory, prevent non-interacting radiation from being received by the telescope, which would potentially resolve the paradoxical transmission with depth seen in the 250 μm and 355 μm grain sizes for JSC Mars-1.

In contrast, samples with a smaller grain size allowed for little variation in the packing efficiency. These samples were easier to prepare as individual grains were more uniform as well and their size allowed multiple layers of material to be stacked on top of one another.

6 Crystalline Rocks: Results and Analysis

The rock samples assessed in this study were collected from the Haughton impact structure on Devon Island, Nunavut, in the Canadian High Arctic archipelago (Osinski et al., 2005). This impact structure is thought to have been formed between 22 ± 2.0 million years ago (Mya) and 39 ± 2 Mya (Sherlock et al., 2005; Young et al., 2013). Samples of shocked gneiss were collected from impact melt rock hills located in and around the crater (Pontefract et al., 2014) and are presumed to be representative of rocks found within impact craters on other planetary bodies. These rock samples may not be perfect analogs for rock types found on Mars, as Mars has no gneiss or granitic rocks. They are used here simply because they were available and will allow an assessment of how porosity and shock effect their transmission properties. For images of the specific thin slices of rock, see Figure 6.1.

The samples are assessed for their shock level (Singleton et al., 2011) which relates to the porosity, as detailed in Pontefract et al. (2014), shown in Table 1.1. For a complete list of rock samples, shock states, and observations see Appendix D Section D.2. As a general rule, as porosity increases one would expect that the transmission of radiation though the rocks would increase (for similar rock types). Increased porosity also increases the number of scattering centers within the rock sample for radiation to interact with.

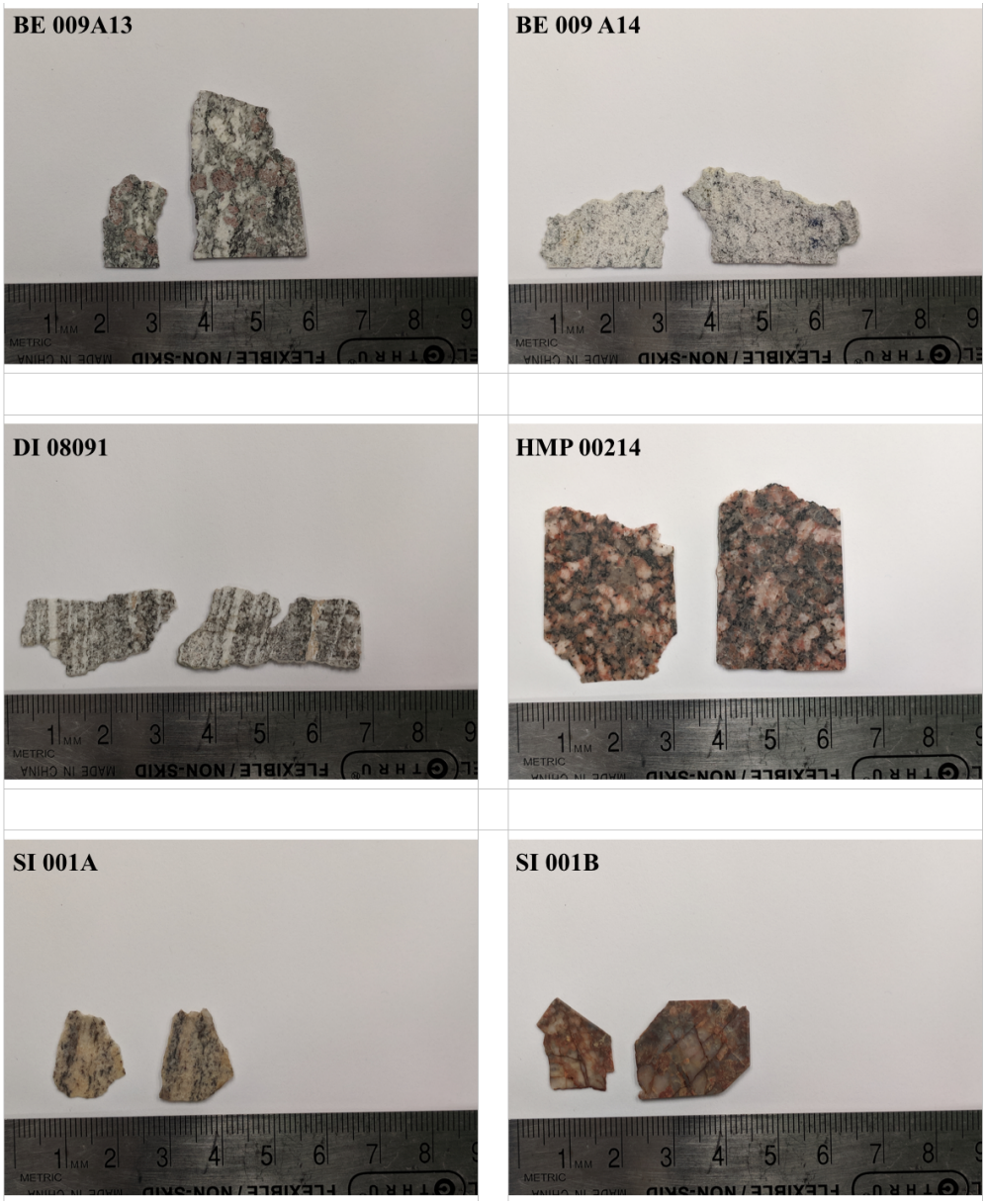

Figure 6.1: ***Crystalline Rock Samples***

The six samples of rock slices obtained from Devon Island, NU and detailed in Pontefract et al. (2014). For each image, the 0.5 mm slice is to the left and the 1.0 mm slice is to the right.

Each identified sample will be analyzed for their zenith transmittance as a function of wavelength and the transmittance of UVA, UVB, and PAR wavelengths with respect to scattering angle. The rock samples as a whole are a more cohesive dataset as all samples reported on here are assessed at two thicknesses and at a larger range of scattering angles, compared to some of the regolith analogs of the previous chapter.

This chapter will detail the results for six such samples and will conclude with a discussion of the implications of these findings.

6.1 Results

The results for the rock samples are strikingly similar to one another, unlike the regolith analogs from Chapter 5. As such, this section will primarily feature the transmission function displayed as a function of wavelength and scattering angle for both thicknesses of the individual sample. A different result is seen in sample DI 08091 and will be discussed in this section as it is not consistent with the results seen in the other rock nor regolith samples.

6.1.1 BE 009 A13

This rock had a low shock stage between 1 and 2, which corresponds to an averaged porosity of about 1%. The average zenith transmission spectrum of specimen BE 009 A13 can be seen in Figure 6.2 as a function of wavelength at thicknesses of 0.5 and 1.0 mm. As expected, the transmission is lower at all wavelengths in the thicker sample. The transmittance in the UV wavelengths is relatively flat and a steady increase in transmittance is seen in PAR

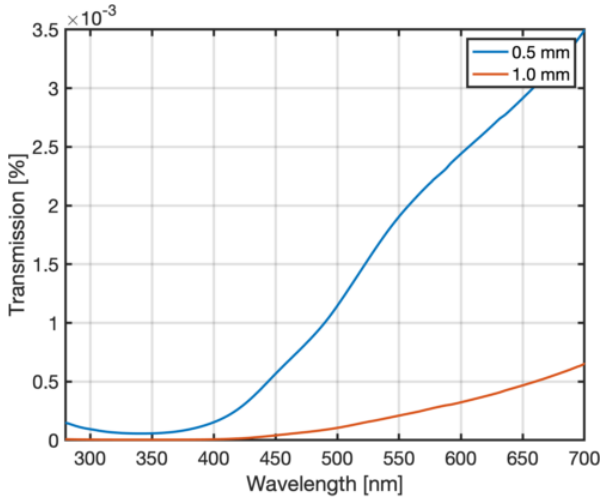

Figure 6.2: ***BE 009 A13: Transmission as a Function of Wavelength***

Average zenith transmission through thicknesses of 0.5 mm and 1.0 mm of rock specimen BE 009 A13 as a function of wavelength.

wavelengths.

UVA, UVB and PAR transmittance as a function of scattering angle can be seen in Figure 6.3 at thicknesses of 0.5 and 1.0 mm. The transmittance of PAR wavelengths is much greater than that of UVA and UVB, and the transmittance is seen to slowly taper off with increased scattering angle. This sample is highly isotropic at both thicknesses, scattering light nearly equally over the range of 30° assessed here.

6.1.2 BE 009 A14

This rock had a high shock stage between 5 and 6, which corresponds to an averaged porosity between 18.5 and 44%. The average zenith transmission spectrum of specimen BE 009 A14 can be seen in Figure 6.4 as a function of wavelength at thicknesses of 0.5 and 1.0 mm.

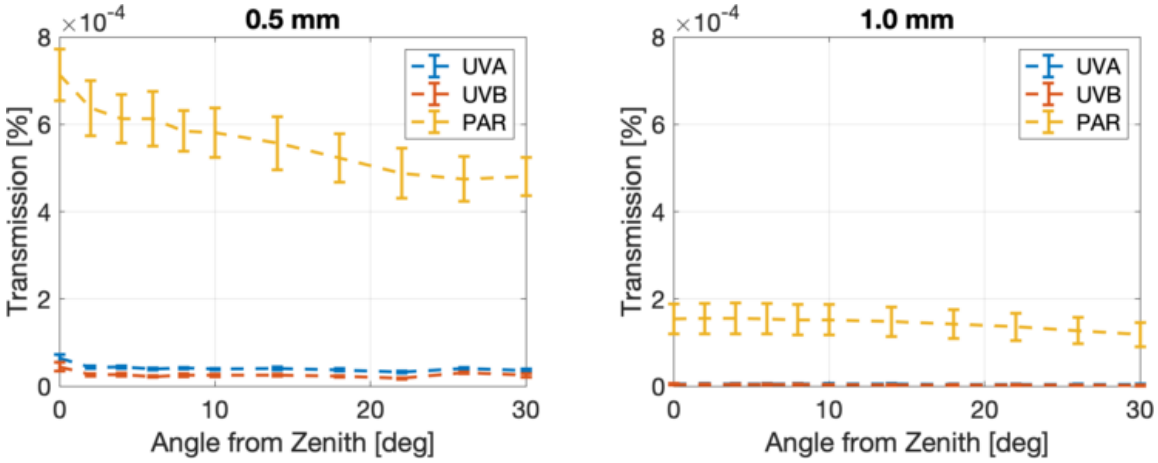

Figure 6.3: ***BE 009 A13: Transmission versus Scattering Angle***

UVA, UVB and PAR transmittance of rock specimen BE 009 A13 shown as a function of scattering angle from zenith for a sample thicknesses of 0.5 mm (left) and 1.0 mm (right). Error bars are the 95% confidence interval.

As expected, the transmission is lower at all wavelengths in the thicker sample and both thicknesses exhibit a relatively flat transmission spectrum across all wavelengths.

UVA, UVB and PAR transmittance as a function of scattering angle can be seen in Figure 6.5 at thicknesses of 0.5 and 1.0 mm. Here, the UVA, UVB and PAR transmission with respect to scattering angle are near identical to one another, also of note, this sample scatters most effectively in the forward direction with near zero transmission seen at scattering angles greater than 10°. At 1.0 mm this sample exhibits elevated transmission at 6° and 18°, which could be due to the high level of shock present.

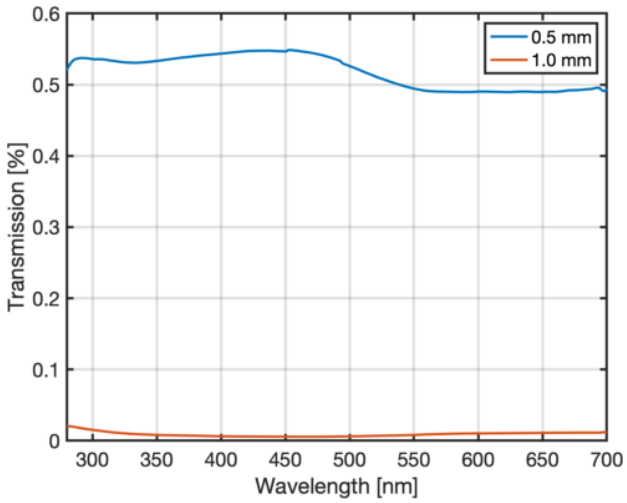

Figure 6.4: ***BE 009 A14: Transmission as a Function of Wavelength***

Average zenith transmission through thicknesses of 0.5 mm and 1.0 mm of rock specimen BE 009 A14 as a function of wavelength.

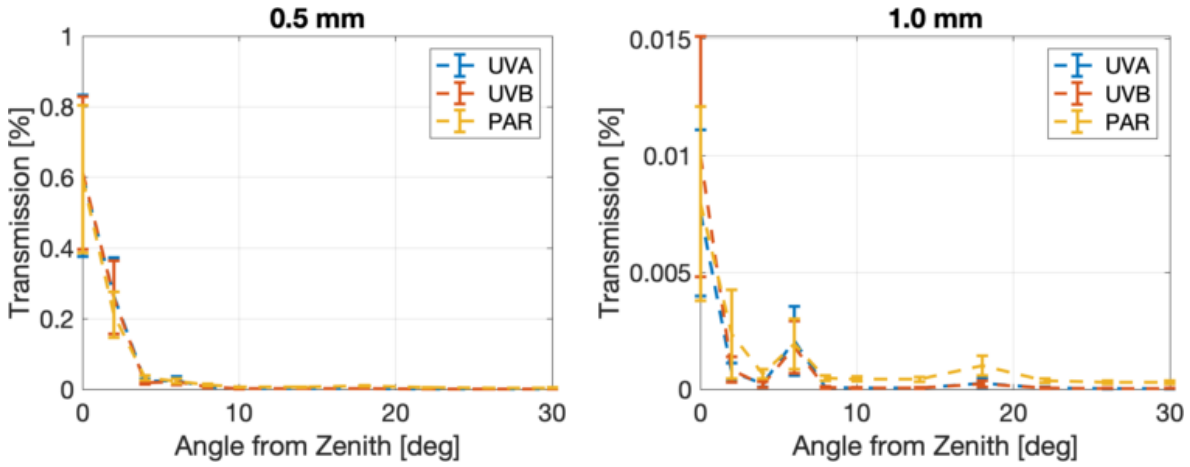

Figure 6.5: ***BE 009 A14: Transmission versus Scattering Angle***

UVA, UVB and PAR transmittance of rock specimen BE 009 A14 shown as a function of scattering angle from zenith for a sample thicknesses of 0.5 mm (left) and 1.0 mm (right). Error bars are the 95% confidence interval.

6.1.3 DI 08091

This rock had a medium shock stage of around 4, which corresponds to an averaged porosity of about 10.5%. The average zenith transmission spectrum of specimen DI 08091 can be seen in Figure 6.6 as a function of wavelength at thicknesses of 0.5 and 1.0 mm. Here, the concerning transition behavior seen with the basaltic sand where the data from both spectrometers meet is present in both sample thicknesses. Not only that, but the behavior between the two sample thicknesses is radically different with the 0.5 mm sample having a peak transmission at a wavelength around 450 nm. The transmission in the 1.0 mm sample looks similar to other rock samples assessed in this study, with very low transmission in the UV wavelengths and a gradual increase of transmission as wavelengths increase.

UVA, UVB and PAR transmittance as a function of scattering angle can be seen in Figure 6.7 at thicknesses of 0.5 and 1.0 mm. The profile observed here is somewhat of a mix between the forward scattering nature of the basaltic sand the isotropic profile seen in the kieserite. Relatively strong peaks are seen at 0° for the 0.5 mm sample and a slow but steady decrease with scattering angle is seen past 2°. Peaks at 0° are seen in the 1.0 mm sample, but not nearly as strong as they are in the 0.5 mm sample.

Upon review of the results from the other rock samples, this sample behaves in a unique way. Further investigation into the individual spectra and runs themselves yielded nothing insightful, they were all collected using typical opacities and the integration times are normal. Figure 6.1 shows images of the 0.5 and 1.0 mm sample of DI 08091, nothing in particular makes this rock sample uniquely different than the others.

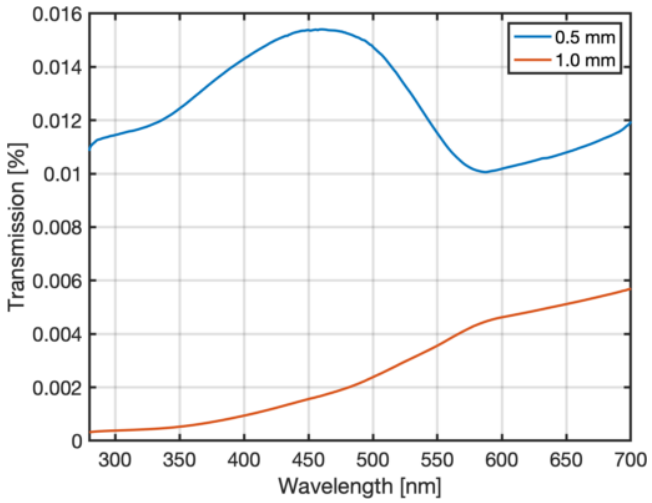

Figure 6.6: ***DI 08091: Transmission as a Function of Wavelength***

Average zenith transmission through thicknesses of 0.5 mm and 1.0 mm of rock specimen DI 08091 as a function of wavelength.

Aside from the operator making a mistake that is unaccounted for, it appears these two samples are not as identical as they should be, given they were sliced from the same larger original specimen. As such, this sample will be left out of any further analysis.

6.1.4 HMP 00214

This rock had a low shock stage between 1 and 2, which corresponds to an averaged porosity of about 1%. The average zenith transmission spectrum of specimen HMP 00214 can be seen in Figure 6.8 as a function of wavelength for thicknesses of 0.5 and 1.0 mm. Here, the UVA and UVB transmittance is small, but not nearly as flat as the other rock samples examined, the increase in transmission with an increased wavelength is not as steep as in other samples.

UVA, UVB and PAR transmittance as a function of scattering angle can be seen in Figure

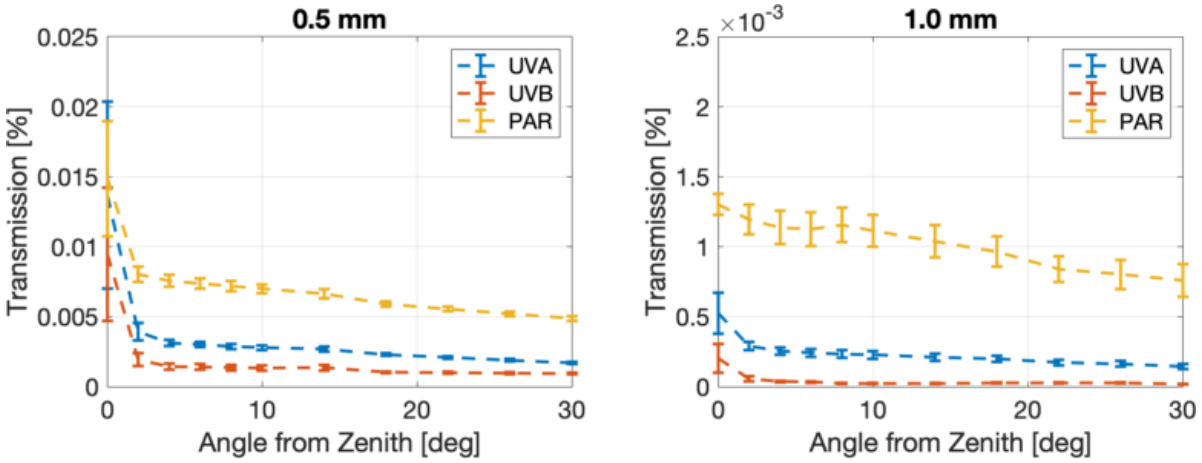

Figure 6.7: ***DI 08091: Transmission versus Scattering Angle***

UVA, UVB and PAR transmittance of rock specimen DI 08091 shown as a function of scattering angle from zenith for a sample thicknesses of 0.5 mm (left) and 1.0 mm (right). Error bars are the 95% confidence interval.

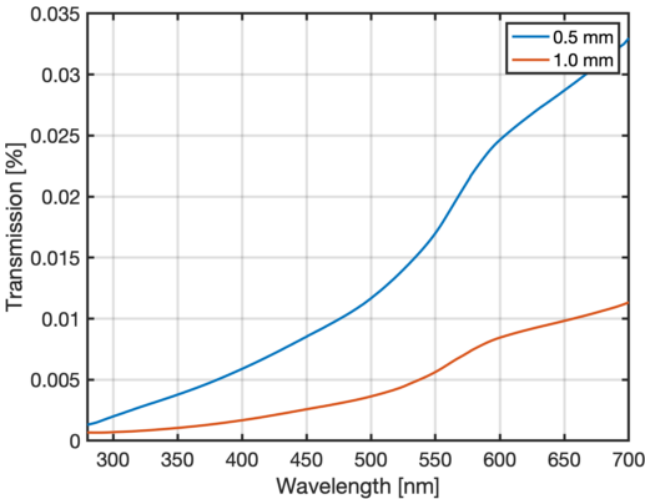

Figure 6.8: ***HMP 00214: Transmission as a Function of Wavelength***

Average zenith transmission through thicknesses of 0.5 mm and 1.0 mm of rock specimen HMP 00214 as a function of wavelength.

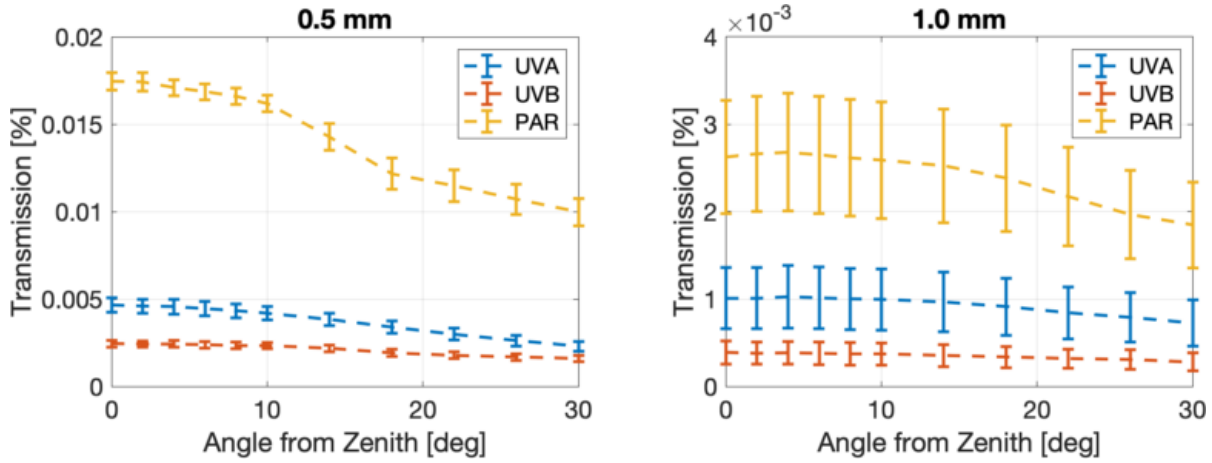

Figure 6.9: ***HMP 00214: Transmission versus Scattering Angle***

UVA, UVB and PAR transmittance of rock specimen HMP 00214 shown as a function of scattering angle from zenith for a sample thicknesses of 0.5 mm (left) and 1.0 mm (right). Error bars are the 95% confidence interval.

6.9 at thicknesses of 0.5 and 1.0 mm. The transmittance of PAR wavelengths is much greater than that of UVA and UVB, and the transmittance is seen to slowly taper off with increased scattering angle. This sample is highly isotropic at both thicknesses, scattering light nearly equally over the range of 30° assessed here.

6.1.5 SI 001A

This rock had a low shock stage between 2 and 3, which corresponds to an averaged porosity of about 1.5%. The average zenith transmission spectrum of specimen SI 001A can be seen in Figure 6.10 as a function of wavelength at thicknesses of 0.5 and 1.0 mm. As expected, the transmission is lower at all wavelengths in the thicker sample and both thicknesses exhibit

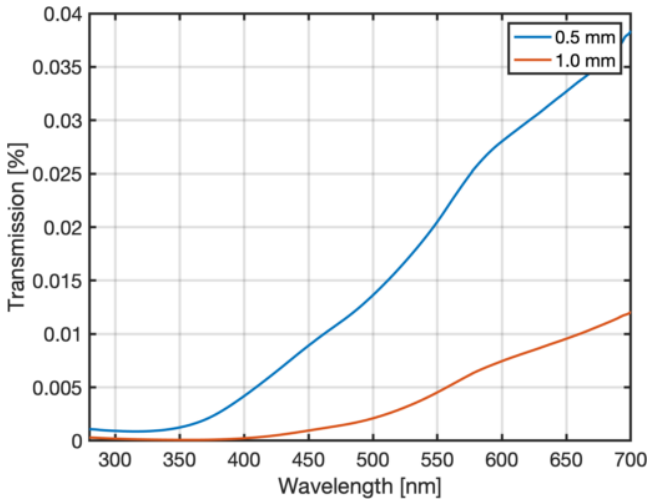

Figure 6.10: ***SI 001A: Transmission as a Function of Wavelength***

Average zenith transmission through a thicknesses of 0.5 mm and 1.0 mm of rock specimen SI 001A as a function of wavelength.

a relatively flat transmission spectrum across all wavelengths.

UVA, UVB and PAR transmittance as a function of scattering angle can be seen in Figure 6.11 at thicknesses of 0.5 and 1.0 mm. The transmittance of PAR wavelengths is much greater than that of UVA and UVB, and the transmittance is seen to slowly taper off with increased scattering angle. This sample is highly isotropic at both thicknesses, scattering light nearly equally over the range of 30° assessed here.

6.1.6 SI 001B

This rock had a low shock stage between 1 and 2, which corresponds to an averaged porosity of about 1%. UVA, UVB and PAR transmittance as a function of scattering angle can be seen in Figure 6.11 at thicknesses of 0.5 and 1.0 mm. The transmittance of PAR wavelengths

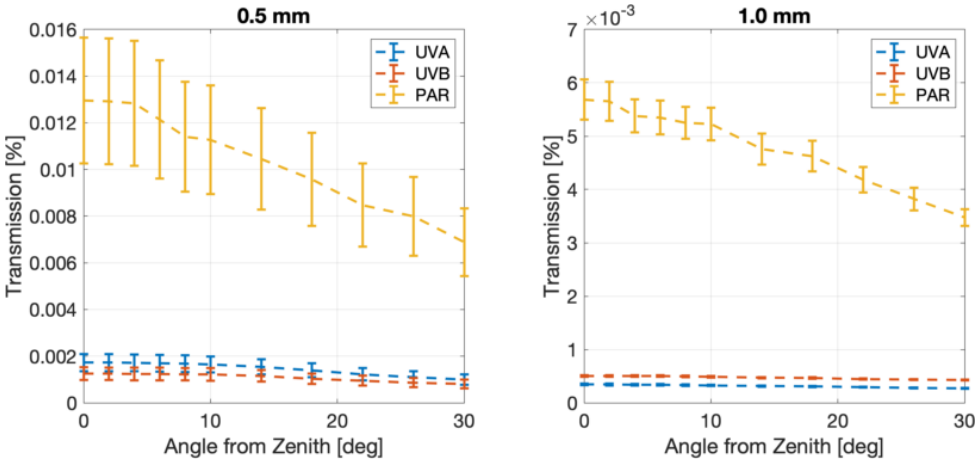

Figure 6.11: ***SI 001A: Transmission versus Scattering Angle***

UVA, UVB and PAR transmittance of rock specimen SI 001A shown as a function of scattering angle from zenith for a sample thicknesses of 0.5 mm (left) and 1.0 mm (right). Error bars are the 95% confidence interval.

is much greater than that of UVA and UVB, but a much steeper falloff in the transmittance is seen with increased scattering angle.

UVA, UVB and PAR transmittance as a function of scattering angle can be seen in Figure 6.13 at thicknesses of 0.5 and 1.0 mm. The transmittance of PAR wavelengths is much greater than that of UVA and UVB, and the transmittance is seen to slowly taper off with increased scattering angle. This sample is highly isotropic at both thicknesses, scattering light nearly equally over the range of 30° assessed here.

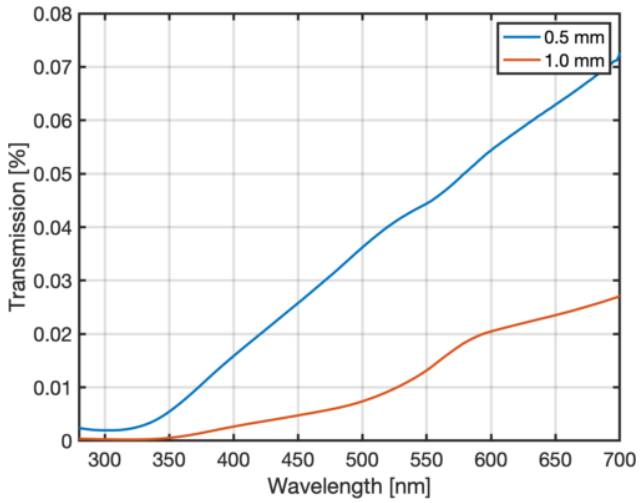

Figure 6.12: ***SI 001B: Transmission as a Function of Wavelength***

Average zenith transmission through a thicknesses of 0.5 mm and 1.0 mm of rock specimen SI 001B as a function of wavelength.

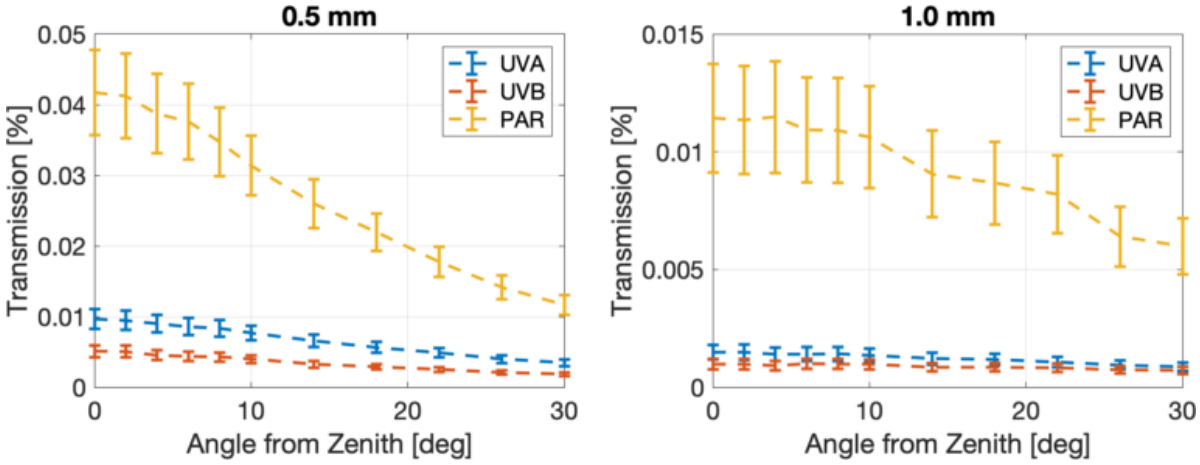

Figure 6.13: ***SI 001B: Transmission versus Scattering Angle***

UVA, UVB and PAR transmittance of rock specimen SI 001B shown as a function of scattering angle from zenith for a sample thicknesses of 0.5 mm (left) and 1.0 mm (right). Error bars are the 95% confidence interval.

6.2 Discussion

By examining the zenith transmittance as a function of wavelength, it is possible to classify the rock samples as either a UV quenching or a UV neutral material. As in Chapter 5 Section 5.2.1, a UV quenching material effectively blocks UV radiation from propagating into the subsurface, where as the UV neutral material effectively transmits uniformly with wavelength. None of the rock samples showed a strong preference to transmitting UV over PAR wavelengths.

By examining the UVA, UVB, and PAR transmittance as a function of scattering angle, it is possible to classify the rock samples as having a forward or an isotropic transmission phase function.

This discussion will focus on five of the six rock samples, leaving DI 08091 out of the analysis because its behavior changes dramatically at the two thicknesses observed and was discussed previously.

Interestingly, the UV quenching samples are also the samples that exhibit an isotropic transmission phase function. This included rock samples: BE 009 A13, HMP 00214, SI 001A, and SI 001B, which all have rather low (≤ 3) shock stages. This can be seen in Figures 6.2, 6.8, 6.10, and 6.12. With the exception of the 0.5 mm sample of HMP 00214, all other runs show a nearly flat transmission spectra for some or all of the UV wavelengths, while transmittance in the PAR wavelength looks relatively uniform in shape between all samples, gradually increasing with wavelength. Similarly, these samples all display a flat or slowly decreasing transmittance with scattering angle as seen in Figures 6.3, 6.9, 6.11, and 6.13.

The one rock sample that exhibits a UV neutral spectra also exhibits a forward scattering transmittance phase function. Rock sample BE 009 A14 exhibits a transmission profile that is seemingly constant as a function of wavelength as seen in Figure 6.4. Notably this rock sample had the highest porosity. This is the only example in the rock samples that has a forward scattering phase function, seen in Figure 6.5.

6.2.1 Extinction in UV Quenching Isotropic Rock Samples

Much like the analysis done for the kieserite sample in Chapter 5, Section 5.2.3, it is possible to assess how radiation is attenuated with respect to wavelength. This section will follow the same formulation as seen in the previous chapter for the kieserite sample, but this time the samples in question will be the four samples that exhibited UV quenching and an isotropic transmission phase function, herein referred to as UVQI, e.g. rock samples BE 009 A13, HMP 00214, SI 001A, and SI 001B.

The average UVQI zenith transmission as a function of wavelength can be seen in Figure 6.14 for thicknesses of 0.5 and 1.0 mm. The corresponding UVA, UVB, and PAR transmission as a function of scattering angle can be seen in Figure 6.15.

The extinction seen in the zenith transmission between the 0.5 and 1.0 mm samples have been calculated as a function of wavelength and are presented in Figure 6.16. Recalling Section 5.2.3 Figure 5.18, which showed the extinction as a function of wavelength seen in the kieserite sample, it is apparent that the extinction at all wavelengths is much higher in the UVQI rock types.

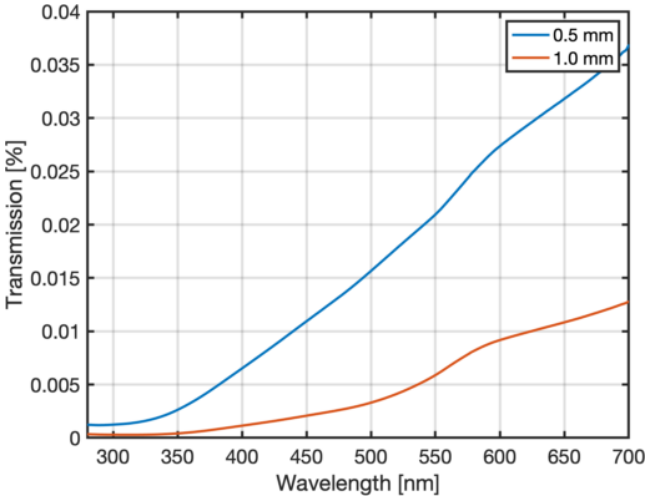

Figure 6.14: ***UVQI: Transmission as a Function of Wavelength***

Average zenith transmission through a thicknesses of 0.5 mm and 1.0 mm rock specimens exhibiting UVQI as a function of wavelength.

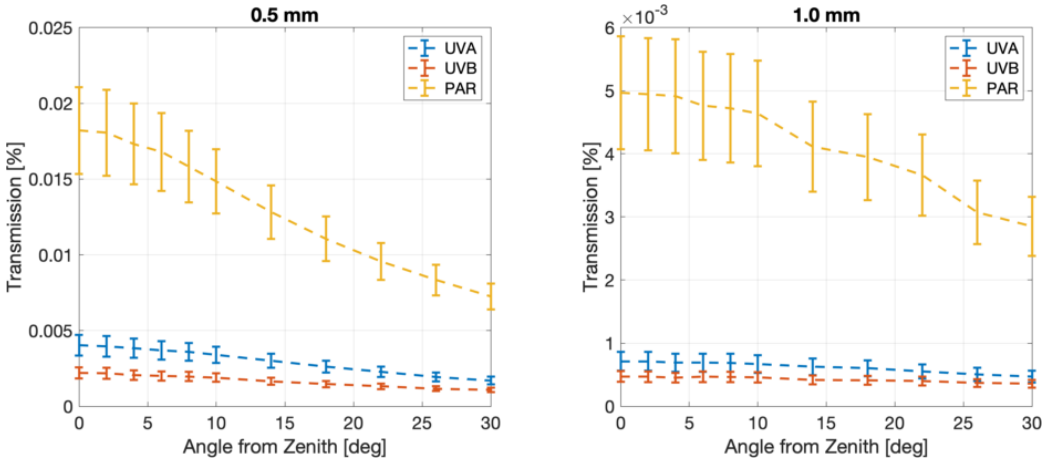

Figure 6.15: ***UVQI Transmission versus Scattering Angle***

UVA, UVB and PAR transmittance of rock specimens exhibiting UVQI shown as a function of scattering angle from zenith for a sample thicknesses of 0.5 mm (left) and 1.0 mm (right). Error bars are the 95% confidence interval.

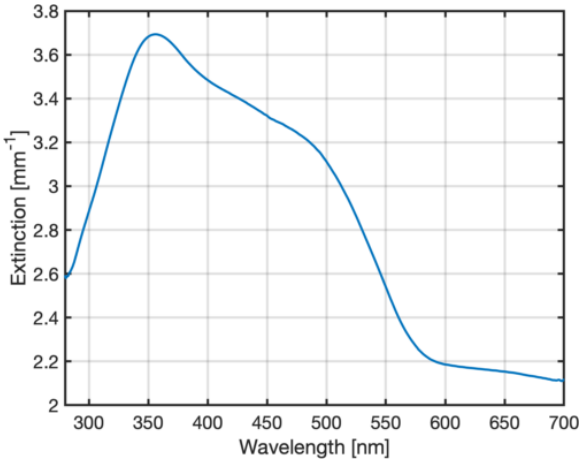

Figure 6.16: ***UVQI: Extinction versus Wavelength***

The extinction coefficient as a function of wavelength shown for the UVQI rock types assessed in this experiment.

6.3 Summary

It is shown that the samples in the lower shock stages are better at attenuating UV wavelengths and produce a more isotropic transmission phase function compared to the high shock samples. This will play a key role for the implications of endolithic habitability, as lower shock stages typically correspond to fewer points of entry into the subsurface for microorganism (Pontefract et al., 2014). Additionally, it was seen with the higher shock rock that the transmission as a function of scattering angle resembled that of the JSC Mars-1 samples in that it favored forward scattering. This is likely due to the increased porosity allowing radiation to pass straight through the samples without interacting with a scattering center.

7 Habitability of Martian Subsurface and Endolithic Environments

This chapter will test the limits of UV radiation dosages in which radioresistant or radiation-resistant extremophiles can thrive in martian subsurface and endolithic environments. In essence this study is looking for locations on Mars that will allow a 10% survivability rate for microorganism populations subject to martian UV conditions. This condition is termed, LD_{90}, or the lethal dosage required to reduce a population size by 90%. This is a purely theoretical exercise that combines martian insolation values, radiation penetration depths for martian analog materials, and LD_{90} values obtained from the literature. Such a low rate of survival was chosen simply because it is unknown what may exist on Mars, for example, the most radioresistant organism seen on earth, *Deinococcus radiodurans*, has been seen to grow when subjected to 6 kilorads/hour radiation environment (Makarova et al., 2001). Additionally, this chapter calculates the amount of PAR available as a source of energy for organism at these depths, this is not necessarily needed. The inclusion of PAR assumes a process similar to photosynthesis on Earth as an energy source, however, if life has found a way to adapt to the extreme UV environment on Mars, it has likely found a suitable source

of energy.

7.1 Doubling and Adding Radiative Transfer Insolation Values

A doubling and adding radiative transfer code (Griffith et al., 2012) was used to calculate the zonal mean insolation at 10° increments in latitude and solar longitude for Mars in Moores et al. (2017). These values represent the total energy per square meter received by an unobscured flat martian surface and are used as the incident radiation in this model.

Their model incorporates the Solar 2000 ASTM Standard Extraterrestrial Spectrum Reference E-490-001 scaled to the distance to Mars per solar longitude as a top-of-atmosphere solar flux. They include Montabone et al. (2015) aerosol optical depths for MY25-32 which were scaled to 880 nm. Additionally, they assume the dust particles in the atmosphere responsible for those opacities are composed of cylinders with a length to diameter ratio of unity with an effective radius of 1.4 μm. For a full description of the model the reader is referred to Moores et al. (2017).

Figure 7.1 shows the interpolated dataset as a function of Solar Longitude, where the latitude is on the vertical axis for UVA, UVB and PAR wavelengths. The color axis represents the insolation, given in kilo-Joules per square meter. Note how the insolation is reminiscent of the global opacity seen in Figure 1.2, this is due to the critical role dust plays in the martian atmospheres' energy budget.

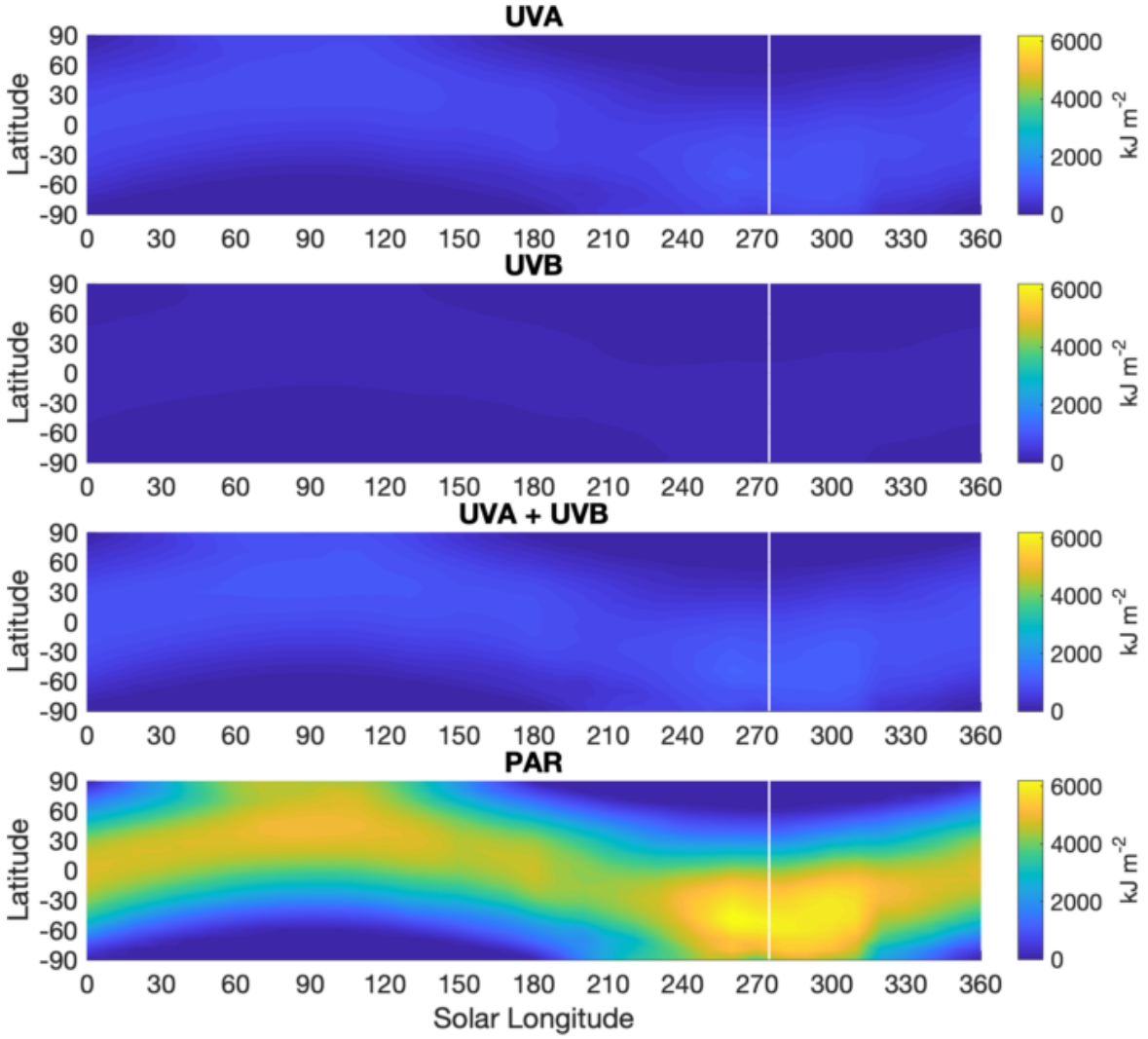

Figure 7.1: ***UVA, UVB, UVA+B, and PAR on Mars' Surface***

The UVA, UVB, UVA+B and PAR energies per square meter displayed as a function of solar longitude and latitude on the vertical axis. Modified from Moores et al. (2017).

7.2 Penetration Depths of Martian Analogs

This study includes the martian analogs that were classified as isotropic scatterers in the forward direction that had multiple depth measurements. This includes kieserite as a regolith analog, and the so called UV quenching isotropic rock samples, e.g. BE 009 A13, HMP 00214, SI 001A, and SI 001B.

The kieserite data has already been assessed for the way in which UVA, UVB and PAR wavelengths are attenuated with depth in Chapter 5 Section 5.2.3 and will be used here. Similarly, the UVQI rock samples have been assessed in the same fashion in Chapter 6 Section 6.2.

The most obvious difference between the absorption in kieserite and the UVQI rock samples is that the rock samples attenuate much more of the UV than the kieserite sample does.

Since these samples are being treated as isotropic scatterers, the amount of transmitted radiation into the subsurface is calculated as the integral of the transmittance as a function of scattering angle over the 2π steradians of the downward hemisphere. Since the data collected for the kieserite and rock samples does not include the entire hemisphere, this value is approximated by the integral over the angles within the dataset, multiplied by two. Dividing these values by the amount of radiation transmitted perpendicular through the sample yields the amount of light scattered into the sample over the whole hemisphere, for each wavelength band.

Multiplying the absorption curve with the integrated subsurface transmittance gives an

approximation for the transmittance of UVA, UVB, and PAR if direct and diffuse light is considered.

7.3 Radioresistant Extremophiles

Three known radioresistant extremophiles are considered in this study. Two of which are tardigrades, *Paramacrobiotus richtersi* and *Ramazzottius oberhaeuseri*, and the third *Bacillus subtilis*. It should be noted that these specific organisms do not derive their energy requirements from photosynthesis, they require complex organic material as an energy source, not PAR, which is examined in this study.

These three organisms have been observed to survive the harsh vacuum of space, the high UV radiation of low earth orbit, and seem adept to survive long periods of time in a desiccated state (Altiero et al., 2011; Schuerger et al., 2003, 2006; Wood et al., 2015), and hence make good candidates for this theoretical exercise.

Tardigrades are small, sub millimeter, animals found in terrestrial, marine and freshwater environments the world over (Nelson, 2002) and *B. subtilis* is an anaerobic bacterium found in soil and in the gastrointestinal tract of humans. Images of a tardigrade and *B. subtilis* can be seen in Figure 7.2.

Altiero et al. (2011) shows that the two tardigrades are observed to have an LD_{90} between 74.82 and 87.72 kJ m^{-2}. That work included minimal amounts of UVC (240-280 nm; 0.09 W m^{-2}, around 2% the total UV dosage in the study). Since the penetration depths of only UVA, UVB, and PAR could be assessed in this dissertation, the larger LD_{90} value will be

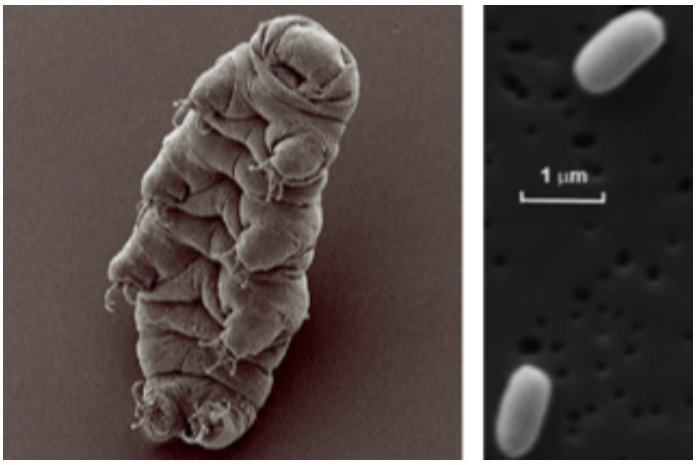

Figure 7.2: *Image of Tardigrade and* B. subtilis

Right: Water bear (tardigrade), Hypsibius dujardini, scanning electron micrograph by Bob Goldstein and Vicky Madden. UNC Chapel Hill. Left: The Bacterium Bacillus subtilis *taken with Scanning Electron Microscopy, adapted from (Deng et al., 2006) under Creative Commons License (CC BY-NC-ND 2.5; https://creativecommons.org/licenses/by-nc-nd/2.5/).*

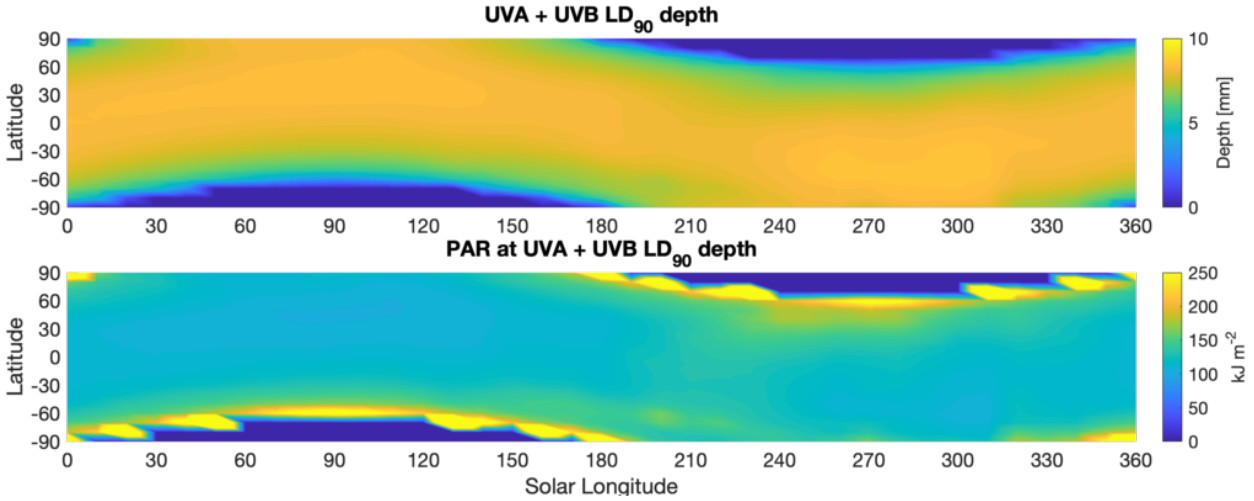

Figure 7.3: ***Kieserite, Tardigrade: LD_{90} Depth and PAR Insolation***

Depth (color axis) at which UVA+UVB LD_{90} occurs for tardigrades given Mars is covered in a bed of granular kieserite as functions of longitude and solar longitude. (top). PAR (color axis) reaching the depths to achieve LD_{90} for the combination of UVA and UVB as a function of latitude and solar longitude.

used.

For *B. subtilis*, Wood et al. (2015), review the literature and find LD_{90} values ranging from 7.8 and 101.5 kJ m^{-2} and note that such a large range can exist due to varying amounts UVA to UVB to UVC radiation used in the various experiments, different sample preparations, and other factors. Wood et al. (2015), conclude that in their study an observed LD_{90} of 48 kJ m^{-2} for *B. subtilis* was found. Their study included only dosages of UVA and UVB which makes their value suitable for this study.

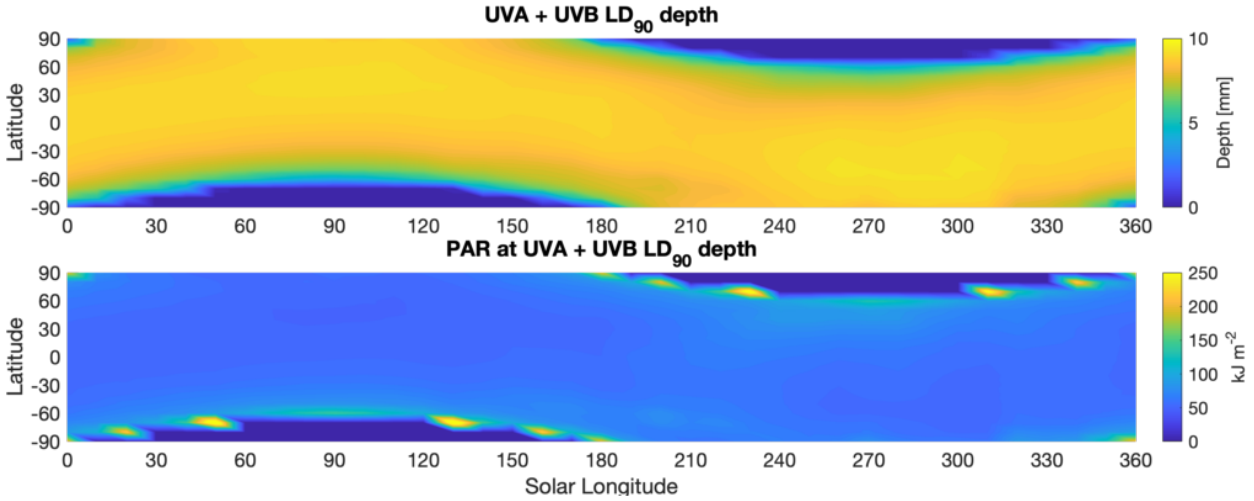

Figure 7.4: *Kieserite,* B. subtilis*: LD_{90} Depth and PAR Insolation*

Depth (color axis) at which UVA+UVB LD_{90} occurs for B. subtilis *given Mars is covered in a bed of granular kieserite as functions of longitude and solar longitude. (top). PAR (color axis) reaching the depths to achieve LD_{90} for the combination of UVA and UVB as a function of latitude and solar longitude.*

7.4 Results

Combining martian insolation values, radiation penetration depths for martian analog materials, and LD_{90} values obtained from the literature for tardigrades and *B. subtilis* yields penetration depths at which LD_{90} occurs.

7.4.1 Kieserite

Figure 7.3 shows the penetration depth per latitude necessary to achieve LD_{90} for the tardigrades given a martian surface comprised of fine kieserite (top) and the amount of PAR

available per latitude at those depths (bottom) as a function of solar longitude. Depths up to 8.6 mm are needed to shield the tardigrades from lethal amounts of UVA and UVB radiation. Notice nearer the poles, during their respective winters, it may be possible for tardigrades to live in near surface environments and even possibly on the surface itself, though they will receive little in the way of PAR as a source of energy.

Figure 7.4 shows the penetration depth per latitude necessary to achieve LD_{90} for the *B. subtilis* given a martian surface comprised of fine kieserite (top) and the amount of PAR available per latitude at those depths (bottom) as a function of solar longitude. Depths up to 9.2 mm are needed to shield the *B. subtilis* from lethal amounts of UVA and UVB radiation. Notice nearer the poles, during their respective winters, it may be possible for *B. subtilis* to live in near surface environments and even possibly on the surface itself, though they will receive little in the way of PAR as a source of energy.

7.4.2 UVQI Rocks

If, instead, the surface of Mars is comprised of the average UVQI rock sample, similar diagrams depicting the depth necessary to shield tardigrade and *B. subtilis* can be derived, see Figure 7.5 and 7.6.

For the tardigrade populations, a minimum depth of 2.1 mm is needed to receive less than lethal dosages of UVA and UVB. Similarly, for *B. subtilis*, a minimum depth of 2.3 mm is needed.

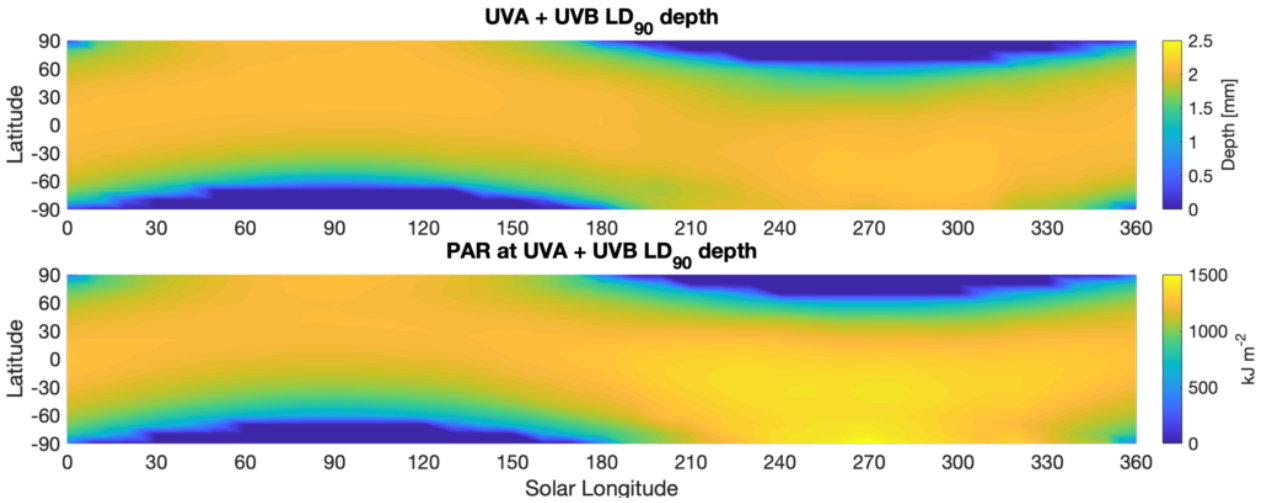

Figure 7.5: *UVQI, Tardigrade: LD_{90} Depth and PAR Insolation*

Depth (color axis) at which UVA+UVB LD_{90} occurs for tardigrades given Mars is covered in UVQI type rocks, as functions of longitude and solar longitude. (top). PAR (color axis) reaching the depths to achieve LD_{90} for the combination of UVA and UVB as a function of latitude and solar longitude.

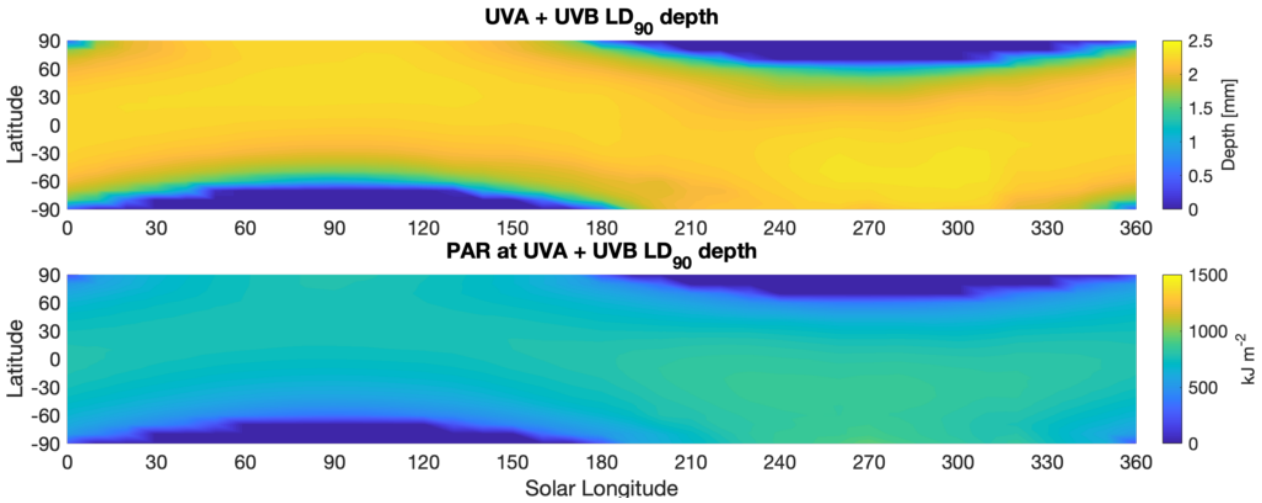

Figure 7.6: *UVQI,* B. subtilis*: LD_{90} Depth and PAR Insolation*

Depth (color axis) at which UVA+UVB LD_{90} occurs for B. subtilis *given Mars is covered in UVQI type rocks, as functions of longitude and solar longitude. (top). PAR (color axis) reaching the depths to achieve LD_{90} for the combination of UVA and UVB as a function of latitude and solar longitude.*

7.5 Discussion

These depths may be too shallow and should be considered the minimum depth required to shield any putative subsurface or endolithic microorganisms considered here. The results above show the depth at which LD_{90} is achieved on a particular sol, with no regard to how the population will survive the next day. The depths presented here continuously kill off 90% of the population every sol. Values for the prolonged survival of *B. subtilis* have been noted in the literature, suggesting that a surviving population can sustain itself under such conditions for approximately 2 months (the duration of their study). So it may be possible for a population to continue to survive at these depths, if only UVA and UVB radiation are taken into account.

If a less aggressive dosage is taken into account, e.g. Altiero et al. (2011) suggest that $LD_{20} = 23.22$ kJ m^{-2} for the tardigrades. This means that 80% of the population survives at this UV dosage. If LD_{20} can be considered an equilibrium point, a point at which the reproduction rate of the population is able to equal the death rate, establishing a stable population sol after sol, the habitable regions are farther into the subsurface than shown above.

This is shown in Figure 7.7 for the case of kieserite and Figure 7.8 for the case of the UVQI rock surface. In both cases, the depth is around 20% deeper into the respective surface. 10.2 mm for the kieserite and 2.5 mm for the UVQI type rocks.

It remains to be seen if these depths are conducive to life. This study did not assess for anything other than UVA and UVB radioresistants. Unlike on Earth, UVC does reach the

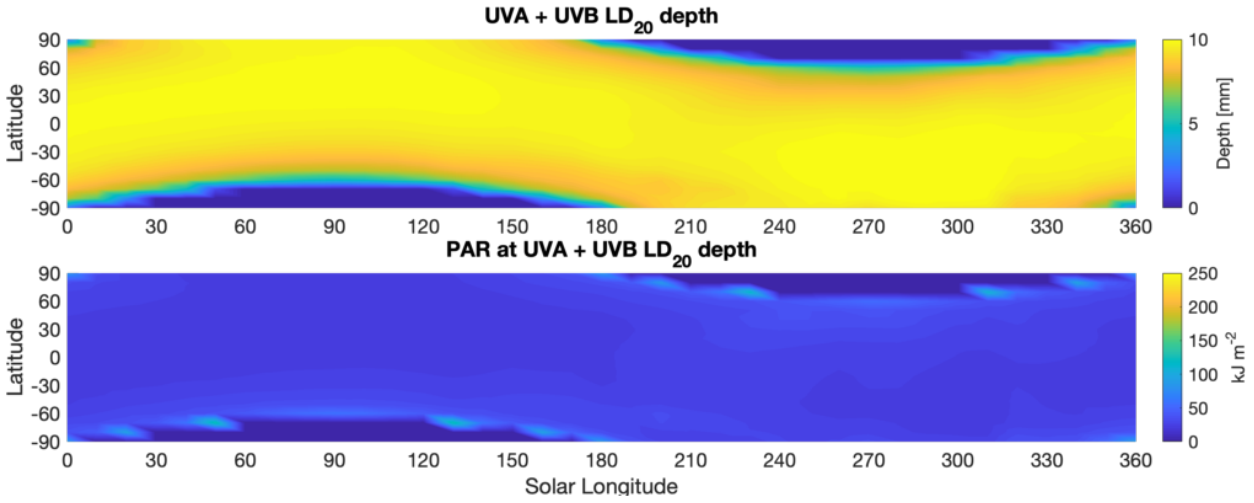

Figure 7.7: ***Kieserite, Tardigrade: LD_{20} Depth and PAR Insolation***

Depth (color axis) at which UVA+UVB LD_{20} occurs for tardigrades given Mars is covered in a bed of granular kieserite as functions of longitude and solar longitude. (top). PAR (color axis) reaching the depths to achieve LD_{20} for the combination of UVA and UVB as a function of latitude and solar longitude.

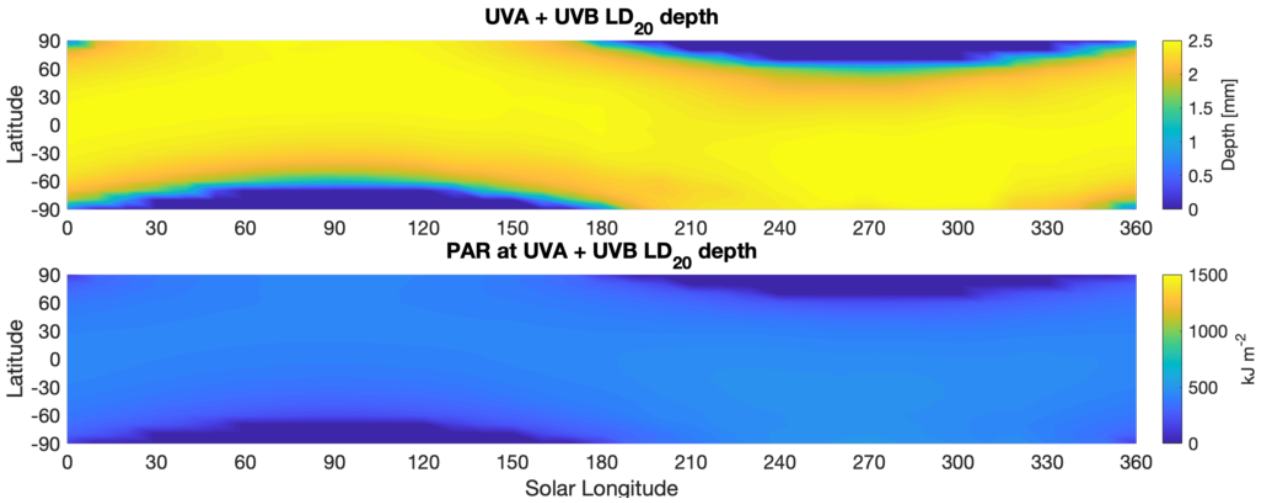

Figure 7.8: *UVQI, Tardigrade: LD_{20} Depth and PAR Insolation*

Depth (color axis) at which UVA+UVB LD_{20} occurs for tardigrades given Mars is covered in UVQI type rocks, as functions of longitude and solar longitude. (top). PAR (color axis) reaching the depths to achieve LD_{20} for the combination of UVA and UVB as a function of latitude and solar longitude.

surface of Mars and will likely push these depths deeper into the surface.

8 Conclusions

8.1 The Dust Environment of Gale Crater

An averaged value for the line-of-sight extinction coefficient was derived through Mars-based images taken by the Mars Science Laboratory rover, Curiosity. The values reported in this dissertation are an updated representation of the dust loading environment in the lower atmosphere of Gale Crater than the values reported on in the previous literature by Moores et al. (2015) and Moore et al. (2016). The reason for this is three-fold: 1. A much larger area of the crater rim is examined in each image allowing the LOS-Ext to be reported in spatial resolution. 2. The images are geographically rectified, minimizing any ill effects of due to observing different portions of the crater rim between images. And 3. A non-subjective way to determine the distance between the rover and the crater rim is implemented to give the best approximation for the LOS-Ext coefficients.

The LOS-Ext seen within Gale Crater exhibits a seasonal trend over the course of observations in this study, nearly two and a half Mars years. The seasonality suggests that the topography and wind patterns responsible for the dust-loading environment of the crater remain consistent, year-over-year, or at the very least change so marginally as to not effect the

results of this study. High visibility is seen within the crater when the LOS-Ext is observed at its seasonal lows during southern autumn and winter and low visibility is seen when the LOS-Ext is observed at its seasonal highs during southern spring and summer.

The vertical distribution of dust within the crater during the most convective time of day shows dust lifting from the crater floor to higher altitudes. The dust within Gale Crater is not well mixed during the most convective time of day, as a large vertical gradient in the dust loading exists. This is seen as a lower LOS-Ext at higher altitudes compared to the LOS-Ext observed nearer the crater floor.

Two models of determining the column-averaged extinction were tested. The first method required the entire Mastcam Tau opacity to be within the PBL, while the other required the LOS-Ext to be constant within the PBL and subtracted from the Mastcam Tau opacity. The first method produced a column-averaged extinction that remains elevated compared to the LOS-Ext for nearly the entire Mars year. This strongly suggests that the atmosphere within Gale Crater is relatively devoid of dust compared to the atmospheric column. Similar values of LOS-Ext and column-averaged extinction are seen near $L_s = 300°$; though, the column-averaged extinction is still larger. This was pointed out by a reviewer of the peer-reviewed manuscript submitted to Icarus as being faulty. As such, a second method was tested and is thought to be more realistic of the dynamics of the vertical profile of dust at Gale Crater. The second method produced column-averaged extinction values that were slightly larger than the LOS-Ext for the first half of the martian year but the two were similar valued near $L_s = 135°$ and $L_s = 180°$ and the LOS-Ext overtakes the column-averaged extinction

during $L_s = 270 - 330°$. The two methods are thought to be upper and lower bounds for the column-averaged extinction.

A simple diffusion model predicts a net sedimentation rate of dust into and out of the crater. A sedimentation rate between 2.7 and 35 μm MY^{-1} is predicted pending the bounds to the column-averaged extinction. The column-averaged extinction from method two produces times of year in which lifting of dust from the crater floor is seen. We believe that this is indicative of a mixing of the atmosphere above the crater and that within the crater, suggesting Gale Crater acts as a source for atmospheric dust during this time. Furthermore, it is also suggestive of a suppressed planetary boundary layer when sedimentation into the crater is observed in the early parts of the Mars year, verifying predictions prior to the landing of MSL at Gale Crater.

8.2 Radiation Propagation in Martian Analog Materials

A mini-goniometer was built to collect transmission spectra of martian analog materials; both granular and rock samples were assessed for their transmission properties. Methods attempting to retrieve transmission parameters, similar to Hapke parameters for reflectance observations, were tested but proved to be inappropriate. Transmission properties of thin-films remained successful, but none of the materials in this study that mimic martian materials were optically thin enough to apply the formalism there.

This work shows that certain regolith and crystalline rock analogs should not be evaluated on their transmission by purely looking at perpendicular transmission measurements. Several

regolith and rock samples exhibited a lambertian scattering function of the transmitted light; this was observed as a near constant transmittance seen at increasing scattering angles. On the other hand, some samples show near zero transmission at angles greater than 10° from perpendicular; for such samples, the perpendicular transmission is a good approximation of radiation scattered into the sample.

The samples were also characterized by their UV shielding abilities. Notable examples of materials that provide excellent UV shielding include cheto bentonite and the four rock samples assessed in Chapter 7. Rocks of this type could provide habitable niches for biosignatures and microorganisms.

8.3 Habitability of the Martian Subsurface

Combining martian insolation values, radiation penetration depths for martian analog materials, and LD_{90} values obtained from the literature for tardigrades and *B. subtilis*, yields penetration depths at which LD_{90} occurs in the martian subsurface environment. The results presented in this dissertation were for analogs that exhibited a lamberitan transmission scattering function as these are thought to be more representative of the types of interactions seen in multiple surface scattering.

In this theoretical exercise, kieserite and UVQL type rocks were shown to provide UV shielding at minimal depths ranging from 2 - 11 mm to protect tardigrades and *B. subtilis* from lethal dosages of UVA and UVB radiation. Survivability increases with depth, but there will exist a depth in which a potential energy source (PAR) is attenuated too much to

be of any practical use for photosynthesis.

9 Further Studies

Observations of the line-of-sight extinction within Gale Crater are still being conducted by the Mars Science Laboratory and custodianship of these observations has changed hands since my departure from the mission. Further methods are being developed to incorporate all Navcam images taken that include the ground local to the rover, a distant object, and a patch of sky to characterize the dust loading environment in multiple directions.

As mentioned in Chapter 2 Section 2.1.2, an additional set of imaging sequences of the northern crater rim are being acquired. The aptly called Mastcam Crater Rim Extinction images contain RGB information and allow a drastic increase the vertical resolution of the crater rim. Research with these images is being conducted to better characterize the vertical profile of dust loading within the lower atmosphere in Gale Crater.

Refinements to the mini-goniometer can be made to increase the number of analogs that can be successfully cataloged. To assess finer grain size materials, it would be helpful to conceive of a way to prepare sample thicknesses below 0.5 mm as even at these thicknesses the majority of the specimens in the collection were too opaque to discern any transmission through the samples. Larger grain size materials also had their shortcomings, wherein samples at twice the thickness were exhibiting more than twice the transmission. This was

largely due to inconsistent sample preparation. Further, incorporating shorter and longer wavelengths to this study can also have a profound effect on the interpretations of the results. The transmission results can be incorporated into radiative transfer codes to model the interactions that occur at the boundary of the atmosphere and the surface environment.

If extant microbial lifeforms exits on modern day Mars, these organisms would need to be radioresistant at a minimum to UV radiation. The theoretical exercise here did not include UVC or Gamma ray radiation, both of which are much more common on the martian surface than on Earth. This exercise also neglected topography, as it treated Mars as a perfectly smooth sphere, which means that the values for the downwelling radiation used in this dissertation could be much greater than they would be in regions cast in shadows for half the sol.

References

Allen, C. C., Jager, K. M., Morris, R. V., Lindstrom, D. J., Lindtsrom, M. M., and Lockwood, J. P. (1998). Martian soil simulant available for scientific, educational study. *Eos, Transactions American Geophysical Union*, 79(34):405–409.

Altiero, T., Guidetti, R., Caselli, V., Cesari, M., and Rebecchi, L. (2011). Ultraviolet radiation tolerance in hydrated and desiccated eutardigrades. *Journal of Zoological Systematics and Evolutionary Research*, 49:104–110.

Amaral, G., Martínez-Frías, J., and Vázquez, L. (2007). Uv shielding properties of jarosite vs. gypsum: Astrobiological implications for mars. *World Applied Sciences*, 2(2):112–116.

Andrews-Hanna, J. C., Zuber, M. T., and Banerdt, W. B. (2008). The borealis basin and the origin of the martian crustal dichotomy. *Nature*, 453(7199):1212.

Arvidson, R. E., Squyres, S. W., Anderson, R. C., Bell, J. F., Blaney, D., Brueckner, J., Cabrol, N. A., Calvin, W. M., Carr, M. H., Christensen, P. R., et al. (2006). Overview of the spirit mars exploration rover mission to gusev crater: Landing site to backstay rock in the columbia hills. *Journal of Geophysical Research: Planets*, 111(E2).

Benardini, J. N., La Duc, M. T., Beaudet, R. A., and Koukol, R. (2014). Implementing planetary protection measures on the mars science laboratory. *Astrobiology*, 14(1):27–32.

Borlina, C. S., Ehlmann, B. L., and Kite, E. S. (2015). Modeling the thermal and physical evolution of mount sharp's sedimentary rocks, gale crater, mars: Implications for diagenesis on the msl curiosity rover traverse. *Journal of Geophysical Research: Planets*, 120(8):1396–1414.

Bridges, N. T. and Ehlmann, B. L. (2018). The mars science laboratory (msl) bagnold dunes campaign, phase i: Overview and introduction to the special issue. *Journal of Geophysical Research: Planets*, 123(1):3–19.

Cantor, B. A. (2007). Moc observations of the 2001 mars planet-encircling dust storm. *Icarus*, 186(1):60–96.

Cantor, B. A., James, P. B., Caplinger, M., and Wolff, M. J. (2001). Martian dust storms: 1999 mars orbiter camera observations. *Journal of Geophysical Research: Planets*, 106(E10):23653–23687.

Cavicchioli, R. (2002). Extremophiles and the search for extraterrestrial life. *Astrobiology*, 2(3):281–292.

Chandrasekhar, S. (1950). Radiative transfer.

Clancy, R., Lee, S., Gladstone, G., McMillan, W., and Rousch, T. (1995). A new model for mars atmospheric dust based upon analysis of ultraviolet through infrared observations from mariner 9, viking, and phobos. *Journal of Geophysical Research: Planets*, 100(E3):5251–5263.

Clancy, R. T., Wolff, M. J., and Christensen, P. R. (2003). Mars aerosol studies with the mgs tes emission phase function observations: Optical depths, particle sizes, and ice cloud types versus latitude and solar longitude. *Journal of Geophysical Research: Planets*, 108(E9).

Cloutis, E. A., Mann, P., Izawa, M. R., Applin, D. M., Samson, C., Kruzelecky, R., Glotch, T. D., Mertzman, S. A., Mertzman, K. R., Haltigin, T. W., et al. (2015). The canadian space agency planetary analogue materials suite. *Planetary and Space Science*, 119:155–172.

Cockell, C. S. and Lee, P. (2002). The biology of impact craters–a review. *Biological Reviews*, 77(3):279–310.

Cockell, C. S. and Raven, J. A. (2004). Zones of photosynthetic potential on mars and the early earth. *Icarus*, 169(2):300–310.

Collis, R. and Russell, P. (1976). Lidar measurement of particles and gases by elastic backscattering and differential absorption. In *Laser monitoring of the atmosphere*, pages 71–151. Springer.

Deng, X., Shi, J., and Kong, M. G. (2006). Physical mechanisms of inactivation of bacillus subtilis spores using cold atmospheric plasmas.

Dickinson, C., Komguem, L., Whiteway, J., Illnicki, M., Popovici, V., Junkermann, W., Connolly, P., and Hacker, J. (2011). Lidar atmospheric measurements on mars and earth. *Planetary and Space Science*, 59(10):942–951.

Drube, L., Leer, K., Goetz, W., Gunnlaugsson, H. P., Haspang, M. P., Lauritsen, N., Madsen, M., Sørensen, L., Ellehoj, M., Lemmon, M., et al. (2010). Magnetic and optical properties of airborne dust and settling rates of dust at the phoenix landing site. *Journal of Geophysical Research: Planets*, 115(E5).

Fenton, L. K. (2003). *Aeolian processes on Mars: atmospheric modeling and GIS analysis*. PhD thesis, California Institute of Technology.

Fike, D. A., Cockell, C., Pearce, D., and Lee, P. (2002). Heterotrophic microbial colonization of the interior of impact-shocked rocks from haughton impact structure, devon island, nunavut, canadian high arctic. *International Journal of Astrobiology*, 1(4):311–323.

Fonseca, R. M., Zorzano-Mier, M.-P., and Martín-Torres, J. (2018). Planetary boundary layer and circulation dynamics at gale crater, mars. *Icarus*, 302:537–559.

Foster, T. L., Winans, L., Casey, R., and Kirschner, L. (1978). Response of terrestrial microorganisms to a simulated martian environment. *Applied and environmental microbiology*, 35(4):730–737.

Friedmann, E. I. (1980). Endolithic microbial life in hot and cold deserts. In *Limits of Life*, pages 33–45. Springer.

Gierasch, P. J. and Goody, R. M. (1972). The effect of dust on the temperature of the martian atmosphere. *Journal of the Atmospheric Sciences*, 29(2):400–402.

Gómez-Elvira, J., Armiens, C., Carrasco, I., Genzer, M., Gómez, F., Haberle, R., Hamilton, V. E., Harri, A.-M., Kahanpää, H., Kemppinen, O., et al. (2014). Curiosity's rover environmental monitoring station: Overview of the first 100 sols. *Journal of Geophysical Research: Planets*, 119(7):1680–1688.

Grant, J. A., Golombek, M. P., Wilson, S. A., Farley, K. A., Williford, K. H., and Chen, A. (2018). The science process for selecting the landing site for the 2020 mars rover. *Planetary and Space Science*.

Green, R., Taylor, D., Gustan, E., Fraser, S., and Olson, R. (1971). Survival of microorganisms in a simulated martian environment. *Space life sciences*, 3(1):12–24.

Griffith, C. A., Doose, L., Tomasko, M. G., Penteado, P. F., and See, C. (2012). Radiative transfer analyses of titans tropical atmosphere. *Icarus*, 218(2):975–988.

Gross, M. (2014). The past and future habitability of planet mars.

Grotzinger, J. P., Crisp, J., Vasavada, A. R., Anderson, R. C., Baker, C. J., Barry, R., Blake, D. F., Conrad, P., Edgett, K. S., Ferdowski, B., et al. (2012). Mars science laboratory mission and science investigation. *Space science reviews*, 170(1-4):5–56.

Guzewich, S. D., Lemmon, M., Smith, C., Martínez, G., de Vicente-Retortillo, Á., Newman, C., Baker, M., Campbell, C., Cooper, B., Gómez-Elvira, J., et al. (2018). Mars science laboratory observations of the 2018/mars year 34 global dust storm. *Geophysical Research Letters*.

Guzewich, S. D., Newman, C., Smith, M., Moores, J., Smith, C., Moore, C., Richardson, M., Kass, D., Kleinböhl, A., Mischna, M., et al. (2017). The vertical dust profile over gale crater, mars. *Journal of Geophysical Research: Planets*, 122(12):2779–2792.

Haberle, R., Renno, N., Richardson, M., Savijärvi, H., Schaeffer, J., Tyler, D., and Vasavada, A. (2012). Meteorological predictions for the rems experiment on msl. *Space Sci. Rev.*

Hagen, C., Hawrylewicz, E., and Ehrlich, R. (1964). Survival of microorganisms in a simulated martian environment i. bacillus subtilis var. globigii. *Applied microbiology*, 12(3):215–218.

Hansen, J. E. and Travis, L. D. (1974). Light scattering in planetary atmospheres. *Space science reviews*, 16(4):527–610.

Hapke, B. (1993). *Theory of reflectance and emittance spectroscopy, topics in remote sensing 3*. Cambridge, UK.

Hapke, B. (2002). Bidirectional reflectance spectroscopy: 5. the coherent backscatter opposition effect and anisotropic scattering. *Icarus*, 157(2):523–534.

Hapke, B. (2012a). Bidirectional reflectance spectroscopy 7: The single particle phase function hockey stick relation. *Icarus*, 221(2):1079–1083.

Hapke, B. (2012b). *Theory of reflectance and emittance spectroscopy*. Cambridge university press.

Hawrylewicz, E., Gowdy, B., and Ehrlich, R. (1962). Micro-organisms under a simulated martian environment. *Nature*, 193(4814):497.

Hong, S.-Y. and Pan, H.-L. (1996). Nonlocal boundary layer vertical diffusion in a medium-range forecast model. *Monthly weather review*, 124(10):2322–2339.

Hunt, G. E., Mitchell, E. A., and Peterfreund, A. R. (1980). The opacity of some local martian dust storms observed by the viking irtm. *Icarus*, 41(3):389–399.

Imshenetsky, A., Kouzyurina, L., and Jakshina, V. (1973). On the multiplication of xerophilic micro-organisms under simulated martian conditions. *Life sciences and space research*, 11:63–66.

Ishimaru, A. (1978). *Wave propagation and scattering in random media*. Academ. Press.

James, P. B., Clancy, T., Lee, S. W., Martin, L. J., Singer, R. B., Smith, E., Kahn, R. A., and Zurek, R. (1994). Monitoring mars with the hubble space telecope: 1990-1991 observations.

Johnson, J. R., Grundy, W. M., and Lemmon, M. T. (2003). Dust deposition at the mars pathfinder landing site: Observations and modeling of visible/near-infrared spectra. *Icarus*, 163(2):330–346.

Johnson, J. R., Sohl-Dickstein, J., Grundy, W. M., Arvidson, R. E., Bell, J., Christensen, P., Graff, T., Guinness, E. A., Kinch, K., Morris, R., et al. (2006). Radiative transfer modeling of dust-coated pancam calibration target materials: Laboratory visible/near-infrared spectrogoniometry. *Journal of Geophysical Research: Planets*, 111(E12).

Kahanpää, H., Newman, C., Moores, J., Zorzano, M.-P., Martín-Torres, J., Navarro, S., Lepinette, A., Cantor, B., Lemmon, M. T., Valentín-Serrano, P., et al. (2016). Convective vortices and dust devils at the msl landing site: annual variability. *Journal of Geophysical Research: Planets*, 121(8):1514–1549.

Kinch, K. M., Sohl-Dickstein, J., Bell, J. F., Johnson, J. R., Goetz, W., and Landis, G. A. (2007). Dust deposition on the mars exploration rover panoramic camera (pancam) calibration targets. *Journal of Geophysical Research: Planets*, 112(E6).

Kleinböhl, A., Schofield, J. T., Kass, D. M., Abdou, W. A., and McCleese, D. J. (2015). No widespread dust in the middle atmosphere of mars from mars climate sounder observations. *Icarus*, 261:118–121.

Kloos, J., Moores, J., Whiteway, J., and Aggarwal, M. (2018). Interannual and diurnal variability in water ice clouds observed from msl over two martian years. *Journal of Geophysical Research: Planets*, 123(1):233–245.

Kloos, J. L., Moores, J. E., Lemmon, M., Kass, D., Francis, R., de la Torre Juárez, M., Zorzano, M.-P., and Martín-Torres, F. J. (2016). The first Martian year of cloud activity from Mars Science Laboratory (sol 0-800). *Advances in Space Research*, 57:1223–1240.

Koike, J., Hori, T., Katahira, Y., Koike, K., Tanaka, K., Kobayashi, K., and Kawasaki, Y. (1996). Fundamental studies concerning planetary quarantine in space. *Advances in Space Research*, 18(1-2):339–344.

Kokhanovsky, A. (2002). Analytical solutions of multiple light scattering problems: a review. *Measurement Science and Technology*, 13(3):233.

Kokhanovsky, A. A. (2004). *Light scattering media optics*. Springer Science & Business Media.

Komguem, L., Whiteway, J., Dickinson, C., Daly, M., and Lemmon, M. (2013). Phoenix {LIDAR} measurements of mars atmospheric dust. *Icarus*, 223(2):649 – 653.

Lemmon, M., Newman, C., Renno, N., Mason, E., Battalio, M., Richardson, M., and Kahanpää, H. (2017). Dust devil activity at the curiosity mars rover field site. In *Lunar and Planetary Science Conference*, volume 48.

Lemmon, M. T., Wolff, M. J., Bell, J. F., Smith, M. D., Cantor, B. A., and Smith, P. H. (2015). Dust aerosol, clouds, and the atmospheric optical depth record over 5 mars years of the mars exploration rover mission. *Icarus*, 251:96–111.

Lewis, K. W. and Aharonson, O. (2014). Occurrence and origin of rhythmic sedimentary rocks on mars. *Journal of Geophysical Research: Planets*, 119(6):1432–1457.

Li, Q. (2008). *Light scattering of semitransparent media*. PhD thesis, Georgia Institute of Technology.

Määttänen, A., Listowski, C., Montmessin, F., Maltagliati, L., Reberac, A., Joly, L., and Bertaux, J.-L. (2013). A complete climatology of the aerosol vertical distribution on mars from mex/spicam uv solar occultations. *Icarus*, 223(2):892–941.

Makarova, K. S., Aravind, L., Wolf, Y. I., Tatusov, R. L., Minton, K. W., Koonin, E. V., and Daly, M. J. (2001). Genome of the extremely radiation-resistant bacterium deinococcus radiodurans viewed from the perspective of comparative genomics. *Microbiology and molecular biology reviews*, 65(1):44–79.

Maki, J., Thiessen, D., Pourangi, A., Kobzeff, P., Litwin, T., Scherr, L., Elliott, S., Dingizian, A., and Maimone, M. (2012). The mars science laboratory engineering cameras. *Space Science Reviews*, 170(1):77–93.

Maki, J. N., Bell, J. F., Herkenhoff, K. E., Squyres, S. W., Kiely, A., Klimesh, M., Schwochert, M., Litwin, T., Willson, R., Johnson, A., Maimone, M., Baumgartner, E., Collins, A., Wadsworth, M., Elliot, S. T., Dingizian, A., Brown, D., Hagerott, E. C., Scherr, L., Deen, R., Alexander, D., and Lorre, J. (2003). Mars exploration rover engineering cameras. *Journal of Geophysical Research: Planets*, 108(E12):n/a–n/a. 8071.

Mancinelli, R. L. and Klovstad, M. (2000). Martian soil and uv radiation: microbial viability assessment on spacecraft surfaces. *Planetary and Space Science*, 48(11):1093–1097.

McKim, R. J. (1999). Telescopic martian dust storms: a narrative and catalogue. *Memoirs of the British Astronomical Association*, 44.

McMahon, S. K. (1996). Overview of the planetary data system. *Planetary and Space Science*, 44(1):3 – 12. Planetary data system.

Montabone, L., Forget, F., Millour, E., Wilson, R., Lewis, S., Cantor, B., Kass, D., Kleinböhl, A., Lemmon, M., Smith, M., et al. (2015). Eight-year climatology of dust optical depth on mars. *Icarus*, 251:65–95.

Moore, C. A., Moores, J. E., Lemmon, M. T., Rafkin, S. C. R., Francis, R., Pla-García, J., Haberle, R. M., Zorzano, M.-P., Martín-Torres, F. J., and Burton, J. R. (2016). A full martian year of line-of-sight extinction within Gale Crater, Mars as acquired by the MSL Navcam through sol 900. *Icarus*, 264:102–108.

Moore, C. A., Moores, J. E., Lemmon, M. T., Rafkin, S. C. R., Francis, R., Pla-García, J., Haberle, R. M., Zorzano, M.-P., Martín-Torres, F. J., and Burton, J. R. (2018). Vertical and Horizontal Heterogeneity of Atmospheric Dust Loading in Northern Gale Crater, Mars. *Icarus*, 264:102–108.

Moores, J., Smith, P., Tanner, R., Schuerger, A., and Venkateswaran, K. (2007). The shielding effect of small-scale martian surface geometry on ultraviolet flux. *Icarus*, 192(2):417–433.

Moores, J. E., Lemmon, M. T., Kahanpää, H., Rafkin, S. C. R., Francis, R., Pla-Garcia, J., Bean, K., Haberle, R., Newman, C., Mischna, M., Vasavada, A. R., de la Torre Juárez, M., Rennó, N., Bell, J., Calef, F., Cantor, B., Mcconnochie, T. H., Harri, A.-M., Genzer, M., Wong, M. H., Smith, M. D., Martín-Torres, F. J., Zorzano, M.-P., Kemppinen, O., and McCullough, E. (2015). Observational evidence of a suppressed planetary boundary layer in northern Gale Crater, Mars as seen by the Navcam instrument onboard the Mars Science Laboratory rover. *Icarus*, 249:129–142.

Moores, J. E., Schieber, J., Kling, A. M., Haberle, R. M., Moore, C. A., Anderson, M. S., Katz, I., Yavrouian, A., Malin, M. C., Olson, T., et al. (2016). Transient atmospheric effects of the landing of the mars science laboratory rover: The emission and dissipation of dust and carbazic acid. *Advances in Space Research*, 58(6):1066–1092.

Moores, J. E., Smith, C. L., and Schuerger, A. C. (2017). Uv production of methane from surface and sedimenting idps on mars in light of rems data and with insights for tgo. *Planetary and Space Science*, 147:48–60.

Napier, W. and Clube, S. (1979). A theory of terrestrial catastrophism. *Nature*, 282(5738):455.

Nelson, D. R. (2002). Current status of the tardigrada: evolution and ecology. *Integrative and Comparative Biology*, 42(3):652–659.

Newman, C. E., Gómez-Elvira, J., Marin, M., Navarro, S., Torres, J., Richardson, M. I., Battalio, J. M., Guzewich, S. D., Sullivan, R., de la Torre, M., et al. (2017). Winds measured by the rover environmental monitoring station (rems) during the mars science laboratory (msl) rover's bagnold dunes campaign and comparison with numerical modeling using marswrf. *Icarus*, 291:203–231.

Nicholson, W. L., Schuerger, A. C., and Setlow, P. (2005). The solar uv environment and bacterial spore uv resistance: considerations for earth-to-mars transport by natural processes and human spaceflight. *Mutation Research/Fundamental and Molecular Mechanisms of Mutagenesis*, 571(1):249–264.

Ordonez-Etxeberria, I., Hueso, R., Sánchez-Lavega, A., Millour, E., and Forget, F. (2019). Meteorological pressure at gale crater from a comparison of rems/msl data and mcd modelling: Effect of dust storms. *Icarus*, 317:591–609.

Osinski, G. R., Lee, P., Parnell, J., Spray, J. G., and Baron, M. (2005). A case study of impact-induced hydrothermal activity: The haughton impact structure, devon island, canadian high arctic. *Meteoritics & Planetary Science*, 40(12):1859–1877.

Packer, E., Scher, S., and Sagan, C. (1963). Biological contamination of mars ii. cold and aridity as constraints on the survival of terrestial microorganisms in simulated martian environments. *Icarus*, 2:293–316.

Pikuta, E. V., Hoover, R. B., and Tang, J. (2007). Microbial extremophiles at the limits of life. *Critical reviews in microbiology*, 33(3):183–209.

Piqueux, S., Byrne, S., Kieffer, H. H., Titus, T. N., and Hansen, C. J. (2015). Enumeration of mars years and seasons since the beginning of telescopic exploration. *Icarus*, 251:332–338.

Pollack, J. B., Colburn, D., Kahn, R., Hunter, J., Van Camp, W., Carlston, C., and Wolf, M. (1977). Properties of aerosols in the martian atmosphere, as inferred from viking lander imaging data. *Journal of Geophysical Research*, 82(28):4479–4496.

Pommerol, A., Thomas, N., Jost, B., Beck, P., Okubo, C., and McEwen, A. (2013). Photometric properties of mars soils analogs. *Journal of Geophysical Research: Planets*, 118(10):2045–2072.

Pontefract, A., Osinski, G. R., Cockell, C. S., Moore, C. A., Moores, J. E., and Southam, G. (2014). Impact-generated endolithic habitat within crystalline rocks of the haughton impact structure, devon island, canada. *Astrobiology*, 14(6):522–533.

Rafkin, S. C., Haberle, R. M., and Michaels, T. I. (2001). The mars regional atmospheric modeling system: Model description and selected simulations. *Icarus*, 151(2):228–256.

Rafkin, S. C., Pla-Garcia, J., Kahre, M., Gomez-Elvira, J., Hamilton, V. E., Marín, M., Navarro, S., Torres, J., and Vasavada, A. (2016). The meteorology of gale crater as determined from rover environmental monitoring station observations and numerical modeling. part ii: Interpretation. *Icarus*, 280:114–138.

Rennó, N. O., Burkett, M. L., and Larkin, M. P. (1998). A simple thermodynamical theory for dust devils. *Journal of the atmospheric sciences*, 55(21):3244–3252.

Richardson, M. I., Toigo, A. D., and Newman, C. E. (2007). Planetwrf: A general purpose, local to global numerical model for planetary atmospheric and climate dynamics. *Journal of Geophysical Research: Planets*, 112(E9).

Rodrigo, R., Garcia-Alvarez, E., López-González, M., and López-Moreno, J. (1990). A nonsteady one-dimensional theoretical model of mars' neutral atmospheric composition between 30 and 200 km. *Journal of Geophysical Research: Solid Earth*, 95(B9):14795–14810.

Schuerger, A. C., Mancinelli, R. L., Kern, R. G., Rothschild, L. J., and McKay, C. P. (2003). Survival of endospores of bacillus subtilis on spacecraft surfaces under simulated martian environments:: implications for the forward contamination of mars. *Icarus*, 165(2):253–276.

Schuerger, A. C., Richards, J. T., Newcombe, D. A., and Venkateswaran, K. (2006). Rapid inactivation of seven bacillus spp. under simulated mars uv irradiation. *Icarus*, 181(1):52–62.

Seelos, K. D., Seelos, F. P., Viviano-Beck, C. E., Murchie, S. L., Arvidson, R. E., Ehlmann, B. L., and Fraeman, A. A. (2014). Mineralogy of the msl curiosity landing site in gale crater as observed by mro/crism. *Geophysical Research Letters*, 41(14):4880–4887.

Sgavetti, M., Pompilio, L., and Meli, S. (2006). Reflectance spectroscopy (0.3–2.5 μm) at various scales for bulk-rock identification. *Geosphere*, 2(3):142–160.

Shaw, A., Daly, M., Cloutis, E., Basic, G., Hamilton, D., Tait, K., Hyde, B., Lymer, E., and Balachandran, K. (2016). Reflectance properties of grey-scale spectralon® as a function of viewing angle, wavelength, and polarization. *International Journal of Remote Sensing*, 37(11):2510–2523.

Sherlock, S. C., Kelley, S. P., Parnell, J., Green, P., Lee, P., Osinski, G. R., and Cockell, C. S. (2005). Re-evaluating the age of the haughton impact event. *Meteoritics & Planetary Science*, 40(12):1777–1787.

Singleton, A. C., Osinski, G. R., McCAUSLAND, P. J., and Moser, D. E. (2011). Shock-induced changes in density and porosity in shock-metamorphosed crystalline rocks, haughton impact structure, canada. *Meteoritics & Planetary Science*, 46(11):1774–1786.

Smith, M. D. (2004). Interannual variability in tes atmospheric observations of mars during 1999–2003. *Icarus*, 167(1):148–165.

Smith, M. D. (2009). Themis observations of mars aerosol optical depth from 2002–2008. *Icarus*, 202(2):444–452.

Smith, M. D., Zorzano, M.-P., Lemmon, M., Martin-Torres, J., and de Cal, T. M. (2016). Aerosol optical depth as observed by the mars science laboratory rems uv photodiodes. *Icarus*, 280:234–248.

Sobolev, V. (1956). Transfer of radiative energy in the atmospheres of stars and planets. *GITTL, Moscow*.

Sobolev, V. (1975). Light scattering in planetary atmospheres, vol. 76, international series of monographs in natural philosophy.

Squyres, S., Arvidson, R., Bell, J. F., Brückner, J., Cabrol, N., Calvin, W., Carr, M., Christensen, P., Clark, B., Crumpler, L., et al. (2004). The opportunity rover's athena science investigation at meridiani planum, mars. *science*, 306(5702):1698–1703.

Squyres, S. W., Arvidson, R. E., Bollen, D., Bell III, J. F., Brueckner, J., Cabrol, N. A., Calvin, W. M., Carr, M. H., Christensen, P. R., Clark, B. C., et al. (2006). Overview of the opportunity mars exploration rover mission to meridiani planum: Eagle crater to purgatory ripple. *Journal of Geophysical Research: Planets*, 111(E12).

Taylor, P. A., Li, P., Michelangeli, D. V., Pathak, J., and Weng, W. (2007). Modelling dust distributions in the atmospheric boundary layer on mars. *Boundary-layer meteorology*, 125(2):305–328.

Toigo, A. D., Lee, C., Newman, C. E., and Richardson, M. I. (2012). The impact of resolution on the dynamics of the martian global atmosphere: Varying resolution studies with the marswrf gcm. *Icarus*, 221(1):276–288.

Tomasko, M., Doose, L., Lemmon, M., Smith, P., and Wegryn, E. (1999). Properties of dust in the martian atmosphere from the imager on mars pathfinder. *Journal of Geophysical Research: Planets*, 104(E4):8987–9007.

Toulmin, P., Baird, A., Clark, B., Keil, K., Rose Jr, H., Christian, R., Evans, P., and Kelliher, W. (1977). Geochemical and mineralogical interpretation of the viking inorganic chemical results. *Journal of Geophysical Research*, 82(28):4625–4634.

Tyler, J. D. and Barnes, J. (2013). Mesoscale modeling of the circulation in the gale crater region: an investigation into the complex forcing of convective boundary layer depths. *International Journal of Mars Science and Exploration*, 8:58–77.

van de Hulst, H. (1980). Multiple scattering light tables. *Formulas and Applications (Academic, New York, 1980)*.

Vasavada, A., Grotzinger, J., Arvidson, R., Calef, F., Crisp, J., Gupta, S., Hurowitz, J., Mangold, N., Maurice, S., Schmidt, M., et al. (2014). Overview of the mars science laboratory mission: Bradbury landing to yellowknife bay and beyond. *Journal of Geophysical Research: Planets*, 119(6):1134–1161.

Vasavada, A. R., Chen, A., Barnes, J. R., Burkhart, P. D., Cantor, B. A., Dwyer-Cianciolo, A. M., Fergason, R. L., Hinson, D. P., Justh, H. L., Kass, D. M., et al. (2012). Assessment of environments for mars science laboratory entry, descent, and surface operations. *Space Science Reviews*, 170(1-4):793–835.

Walker, J. J. and Pace, N. R. (2007). Endolithic microbial ecosystems. *Annu. Rev. Microbiol.*, 61:331–347.

Wang, H. and Richardson, M. I. (2015). The origin, evolution, and trajectory of large dust storms on mars during mars years 24–30 (1999–2011). *Icarus*, 251:112–127.

Wang, H., Richardson, M. I., Wilson, R. J., Ingersoll, A. P., Toigo, A. D., and Zurek, R. W. (2003). Cyclones, tides, and the origin of a cross-equatorial dust storm on mars. *Geophysical Research Letters*, 30(9).

Weiss, B. P., Yung, Y. L., and Nealson, K. H. (2000). Atmospheric energy for subsurface life on mars? *Proceedings of the National Academy of Sciences*, 97(4):1395–1399.

Whiteway, J., Daly, M., Carswell, A., Duck, T., Dickinson, C., Komguem, L., and Cook, C. (2008). Lidar on the phoenix mission to mars. *Journal of Geophysical Research: Planets*, 113(E3).

Whiteway, J., Komguem, L., Dickinson, C., Cook, C., Illnicki, M., Seabrook, J., Popovici, V., Duck, T., Davy, R., Taylor, P., et al. (2009). Mars water-ice clouds and precipitation. *science*, 325(5936):68–70.

Wood, J. P., Meyer, K. M., Kelly, T. J., Choi, Y. W., Rogers, J. V., Riggs, K. B., and Willenberg, Z. J. (2015). Environmental persistence of bacillus anthracis and bacillus subtilis spores. *PloS one*, 10(9):e0138083.

Young, K. E., Soest, M. C., Hodges, K. V., Watson, E. B., Adams, B. A., and Lee, P. (2013). Impact thermochronology and the age of haughton impact structure, canada. *Geophysical Research Letters*, 40(15):3836–3840.

Zurek, R. W., Barnes, J. R., Haberle, R. M., Pollack, J. B., Tillman, J. E., and Leovy, C. B. (1992). Dynamics of the atmosphere of mars. *Mars*, pages 835–933.

A Navcam and Mastcam Images

A.1 Navcam Images

Table A.1: ***The Dust Devil Search Movie Dataset for LOS-Ext.***

Sol	Image Name	Date			Method			
		LTST	MY	L_S	A1	A2	A3	A4
100	NLA_406359501RAD_S0050104NCAM00535M1.IMG	10:15	31	208.1°	✓	✓	✓	✓
101	NLA_406455531RAD_S0050178NCAM00535M1.IMG	12:12	31	208.8°	✓	✓	✓	✓
105	NLA_406809999RAD_S0050388NCAM00535M1.IMG	12:01	31	211.3°	✓	✓	✓	✓
117	NLA_407882821RAD_S0050432NCAM00535M1.IMG	14:00	31	578.9°	✓	✓	✓	✓
119	NLA_408057640RAD_S0050432NCAM00535M1.IMG	13:15	31	220.2°	✓	✓	✓	✓
122	NLA_408321897RAD_S0050926NCAM00535M1.IMG	12:41	31	222.1°	✓	✓	✓	✓
124	NLA_408499719RAD_S0051070NCAM00535M1.IMG	12:44	31	223.4°	✓	✓	✓	✓
126	NLA_408674336RAD_S0051398NCAM00535M1.IMG	11:56	31	224.6°	✓		✓	
131	NLA_409119358RAD_S0051662NCAM00535M1.IMG	12:12	31	227.9°	✓		✓	
133	NLA_409299715RAD_S0051662NCAM00535M1.IMG	12:57	31	229.2°	✓		✓	
135	NLA_409473292RAD_S0051858NCAM00535M1.IMG	11:52	31	230.4°	✓		✓	
138	NLA_409741010RAD_S0051858NCAM00535M1.IMG	12:13	31	232.4°	✓		✓	
139	NLA_409829784RAD_S0051858NCAM00535M1.IMG	12:13	31	233.0°	✓		✓	
141	NLA_410007335RAD_S0051858NCAM00535M1.IMG	12:12	31	234.3°	✓		✓	
142	NLA_410096109RAD_S0051858NCAM00535M1.IMG	12:11	31	235.0°	✓		✓	
143	NLA_410184881RAD_S0051858NCAM00535M1.IMG	12:10	31	235.6°	✓		✓	
144	NLA_410273662RAD_S0051858NCAM00535M1.IMG	12:10	31	236.3°	✓		✓	
145	NLA_410362421RAD_S0051858NCAM00535M1.IMG	12:09	31	236.9°	✓		✓	
146	NLA_410451199RAD_S0051858NCAM00535M1.IMG	12:09	31	237.5°	✓		✓	
148	NLA_410627193RAD_S0051902NCAM00535M2.IMG	11:42	31	238.8°	✓		✓	
150	NLA_410814834RAD_S0051902NCAM00535M1.IMG	14:24	31	240.2°				
153	NLA_411067061RAD_S0051954NCAM00535M2.IMG	10:35	31	242.1°	✓		✓	
154	NLA_411160451RAD_S0051954NCAM00535M2.IMG	11:49	31	242.7°	✓		✓	
158	NLA_411527274RAD_S0051954NCAM00535M2.IMG	14:56	31	245.4°				
160	NLA_411691430RAD_S0051986NCAM00535M1.IMG	11:18	31	246.6°	✓		✓	
162	NLA_411869915RAD_S0051986NCAM00535M1.IMG	11:32	31	247.9°	✓		✓	
165	NLA_412136241RAD_S0052270NCAM00535M1.IMG	11:30	31	249.9°	✓		✓	

Methods are discussed in Ch. 2, Sec. 2.3.

Continued on next page...

Table A.1: ***The Dust Devil Search Movie Dataset for LOS-Ext, cont'd...***

Sol	Image Name	LTST	Date MY	L_S	Method A1	A2	A3	A4
166	NLA_412225016RAD_S0052270NCAM00535M1.IMG	11:30	31	250.6°	✓		✓	
167	NLA_412315447RAD_S0060000NCAM00535M1.IMG	11:56	31	251.2°	✓		✓	
167	NLA_412319447RAD_S0060000NCAM00535M1.IMG	13:00	31	251.3°				
175	NLA_413025644RAD_S0060000NCAM00535M1.IMG	11:50	31	256.4°	✓		✓	
175	NLA_413029644RAD_S0060000NCAM00535M1.IMG	12:54	31	256.4°				
177	NLA_413202423RAD_S0060000NCAM00542M1.IMG	11:36	31	257.7°	✓		✓	
179	NLA_413379083RAD_S0060000NCAM00542M1.IMG	11:21	31	259.0°	✓		✓	
181	NLA_413556634RAD_S0060000NCAM00542M1.IMG	11:19	31	260.3°	✓		✓	
183	NLA_413734491RAD_S0060000NCAM00542M1.IMG	11:23	31	261.6°	✓		✓	
185	NLA_413911731RAD_S0060000NCAM00542M1.IMG	11:16	31	262.9°	✓		✓	
187	NLA_414090159RAD_S0060000NCAM00542M1.IMG	11:29	31	264.2°	✓		✓	
189	NLA_414266828RAD_S0060000NCAM00542M2.IMG	11:14	31	265.5°	✓		✓	
193	NLA_414621927RAD_S0060000NCAM00542M1.IMG	11:11	31	268.1°	✓		✓	
227	NLB_417644847RAD_S0060000NCAM00542M1.IMG	12:03	31	289.9°	✓		✓	
232	NLB_418086180RAD_S0060000NCAM00542M1.IMG	11:19	31	293.0°	✓		✓	
271	NLB_421547041RAD_S0060000NCAM00542M1.IMG	10:44	31	316.6°	✓		✓	
274	NLB_421813912RAD_S0060068NCAM00542M2.IMG	10:53	31	318.4°	✓		✓	
283	NLB_422613465RAD_S0060082NCAM00542M1.IMG	11:01	31	323.6°	✓		✓	
288	NLB_423057880RAD_S0060082NCAM00542M1.IMG	11:09	31	326.5°	✓		✓	
296	NLB_423767044RAD_S0060116NCAM00542M2.IMG	10:53	31	331.0°	✓		✓	
300	NLB_424123610RAD_S0060308NCAM00542M3.IMG	11:17	31	333.3°	✓	✓	✓	✓
306	NLB_424663036RAD_S0060450NCAM00542M2.IMG	13:07	31	336.7°	✓	✓	✓	✓
311	NLB_425100796RAD_S0060658NCAM00542M2.IMG	11:28	31	339.4°	✓	✓	✓	✓
315	NLB_425457095RAD_S0060704NCAM00542M2.IMG	11:49	31	341.6°	✓	✓	✓	✓
319	NLB_425805675RAD_S0060804NCAM00542M1.IMG	10:03	31	343.7°	✓	✓	✓	✓
323	NLB_426161331RAD_S0060804NCAM00542M1.IMG	10:13	31	345.9°	✓	✓	✓	✓
328	NLB_426607464RAD_S0070136NCAM00542M1.IMG	10:51	31	348.6°	✓	✓	✓	✓
331	NLB_426874661RAD_S0070270NCAM00546M1.IMG	11:06	31	350.2°	✓	✓	✓	✓
339	NLB_427585501RAD_S0080610NCAM00546M1.IMG	11:18	31	354.4°	✓	✓	✓	✓
348	NLB_428379667RAD_S0100508NCAM00546M1.IMG	10:03	31	359.0°	✓	✓	✓	✓
352	NLB_428741466RAD_S0110302NCAM00546M1.IMG	11:53	32	1.1°	✓	✓	✓	✓
368	NLB_430162679RAD_S0120690NCAM00546M1.IMG	12:11	32	9.2°	✓	✓	✓	✓
374	NLB_430689336RAD_S0140000NCAM00546M1.IMG	10:36	32	12.1°	✓	✓	✓	✓
380	NLB_431225192RAD_S0141262NCAM00546M1.IMG	11:30	32	15.1°	✓	✓	✓	✓
390	NLB_432112304RAD_S0151230NCAM00546M2.IMG	11:24	32	20.0°	✓	✓	✓	✓
399	NLB_432910405RAD_S0160148NCAM00546M2.IMG	11:13	32	24.3°	✓	✓	✓	✓
408	NLB_433718770RAD_S0170000NCAM00546M1.IMG	13:49	32	28.6°	✓	✓	✓	✓
421	NLB_434871645RADLS0190000NCAM00546M1.IMG	13:34	32	34.7°	✓	✓	✓	✓
425	NLB_435220337RADLS0191066NCAM00546M1.IMG	11:51	32	36.5°	✓	✓	✓	✓
427	NLB_435402110RADLS0200000NCAM00546M1.IMG	13:01	32	37.5°	✓	✓	✓	✓
435	NLB_436111540RADLS0210000NCAM00546M1.IMG	12:51	32	41.2°	✓	✓	✓	✓
468	NLB_439040601RAD_S0230890NCAM00546M2.IMG	12:53	32	56.2°	✓	✓	✓	✓
491	NLB_441084413RAD_S0240408NCAM00546M1.IMG	13:32	32	66.6°	✓	✓	✓	✓
503	NLB_442143591RAD_S0250000NCAM00546M1.IMG	11:55	32	71.9°	✓	✓	✓	✓

Methods are discussed in Ch. 2, Sec. 2.3.

Continued on next page...

Table A.1: ***The Dust Devil Search Movie Dataset for LOS-Ext, cont'd...***

Sol	Image Name	LTST	Date MY	L_S	Method A1	A2	A3	A4
520	NLB_443651152RAD_S0251070NCAM00546M1.IMG	11:33	32	79.6°	✓	✓	✓	✓
527	NLB_444273095RAD_S0251638NCAM00546M1.IMG	11:42	32	82.7°	✓	✓	✓	✓
553	NLB_446582291RAD_S0280000NCAM00546M1.IMG	12:04	32	94.5°	✓		✓	
562	NLB_447391584RAD_S0281374NCAM00546M1.IMG	14:51	32	98.6°				
575	NLB_448538496RAD_S0300740NCAM00546M1.IMG	12:58	32	104.6°	✓	✓	✓	✓
581	NLB_449081582RAD_S0300786NCAM00546M1.IMG	15:47	32	107.5°				
590	NLB_449872847RAD_S0310000NCAM00546M1.IMG	13:44	32	111.6°	✓	✓	✓	✓
601	NLB_450846169RAD_S0310724NCAM00546M1.IMG	12:54	32	116.8°	✓		✓	
635	NLB_453860307RAD_S0320478NCAM00546M1.IMG	11:51	32	133.4°	✓	✓	✓	✓
648	NLB_455016616RAD_S0340000NCAM00546M1.IMG	12:29	32	139.9°	✓	✓	✓	✓
656	NLB_455727524RAD_S0340774NCAM00546M1.IMG	12:42	32	144.1°	✓	✓	✓	✓
659	NLB_456000958RAD_S0350238NCAM00546M1.IMG	14:37	32	145.6°				
674	NLB_457331668RAD_S0380000NCAM00546M1.IMG	14:25	32	153.5°				
710	NLB_460519876RAD_S0400366NCAM00546M1.IMG	12:26	32	173.3°	✓		✓	
720	NLB_461404078RAD_S0401378NCAM00546M1.IMG	11:29	32	179.0°	✓	✓	✓	✓
730	NLB_462296969RAD_S0401850NCAM00546M1.IMG	12:53	32	184.8°	✓	✓	✓	✓
758	NLB_464780544RAD_S0421020NCAM00546M1.IMG	12:18	32	201.6°	✓		✓	✓
766	NLB_465492935RAD_S0421020NCAM00546M1.IMG	12:52	32	206.6°	✓	✓	✓	✓
779	NLB_466647299RAD_S0430000NCAM00546M1.IMG	12:54	32	214.7°	✓	✓	✓	✓
795	NLB_468064273RAD_S0440568NCAM00546M1.IMG	11:53	32	224.9°	✓	✓	✓	✓
796	NLB_468165008RAD_S0440568NCAM00546M1.IMG	15:06	32	225.6°				
801	NLB_468599333RAD_S0441140NCAM00546M1.IMG	12:30	32	228.8°	✓		✓	
803	NLB_468775080RAD_S0441140NCAM00546M1.IMG	12:00	32	230.0°	✓		✓	
808	NLB_469216377RAD_S0441432NCAM00546M1.IMG	11:16	32	233.2°	✓	✓	✓	✓
812	NLB_469577444RAD_S0441432NCAM00546M1.IMG	12:51	32	235.9°	✓	✓	✓	✓
823	NLB_470550103RAD_S0441828NCAM00546M2.IMG	11:42	32	243.0°	✓	✓	✓	✓
835	NLB_471612686RAD_S0442062NCAM00546M2.IMG	10:50	32	250.8°	✓	✓	✓	✓
840	NLB_472059689RAD_S0442414NCAM00546M1.IMG	11:38	32	254.1°	✓	✓	✓	✓
844	NLB_472415147RAD_S0442414NCAM00546M1.IMG	11:41	32	256.7°	✓	✓	✓	✓
854	NLB_473299919RAD_S0442414NCAM00546M4.IMG	10:45	32	263.2°	✓	✓	✓	✓
864	NLB_474194362RAD_S0442958NCAM00546M1.IMG	12:27	32	269.7°	✓	✓	✓	✓
886	NLB_476145975RAD_S0450000NCAM00546M2.IMG	11:49	32	283.8°	✓	✓	✓	✓
890	NLB_476502340RAD_S0450000NCAM00546M2.IMG	12:07	32	286.4°	✓	✓	✓	✓
895	NLB_476941891RAD_S0450000NCAM00546M1.IMG	10:54	32	289.5°	✓	✓	✓	✓
907	NLB_478005967RAD_S0450450NCAM00546M1.IMG	10:29	32	297.0°	✓	✓	✓	✓
915	NLB_478720831RAD_S0450450NCAM00546M1.IMG	11:41	32	301.9°	✓	✓	✓	✓
921	NLB_479252781RAD_S0450450NCAM00546M1.IMG	11:27	32	305.6°	✓	✓	✓	✓
925	NLB_479607184RAD_S0450774NCAM00546M1.IMG	11:15	32	308.0°	✓	✓	✓	✓
926	NLB_479684459RAD_S0450774NCAM00546M1.IMG	08:07	32	308.5°				
927	NLB_479801831RAD_S0450852NCAM00546M1.IMG	15:50	32	309.3°				
929	NLB_479965633RAD_S0450852NCAM00546M2.IMG	12:08	32	310.4°	✓	✓	✓	✓
929	NLB_479980257RAD_S0450852NCAM00546M2.IMG	16:04	32	310.5°				
931	NLB_480127148RAD_S0450852NCAM00546M2.IMG	07:46	32	311.5°				
931	NLB_480141609RAD_S0450852NCAM00546M2.IMG	11:42	32	311.6°	✓	✓	✓	✓

Methods are discussed in Ch. 2, Sec. 2.3.

Continued on next page...

Table A.1: ***The Dust Devil Search Movie Dataset for LOS-Ext, cont'd...***

Sol	Image Name	LTST	Date MY	L_S	Method A1	A2	A3	A4
937	NLB_480658555RAD_S0450852NCAM00546M1.IMG	07:25	32	315.0°				
939	NLB_480854122RAD_S0450852NCAM00546M1.IMG	12:18	32	316.3°	✓	✓	✓	✓
941	NLB_481011411RAD_S0450996NCAM00546M1.IMG	06:48	32	317.4°				
943	NLB_481210968RAD_S0450996NCAM00546M1.IMG	12:46	32	318.7°	✓	✓	✓	✓
945	NLB_481382926RAD_S0451108NCAM00546M1.IMG	11:15	32	319.8°	✓	✓	✓	✓
947	NLB_481544153RAD_S0451108NCAM00546M1.IMG	06:49	32	320.9°				
949	NLB_481739499RAD_S0451108NCAM00546M1.IMG	11:38	32	322.2°	✓	✓	✓	✓
961	NLB_482806980RAD_S0461676NCAM00546M1.IMG	12:13	32	329.1°	✓	✓	✓	✓
968	NLB_483426104RAD_S0470522NCAM00546M1.IMG	11:36	32	333.0°	✓	✓	✓	✓
973	NLB_483879352RAD_S0470598NCAM00546M1.IMG	14:07	32	335.8°				
984	NLB_484840753RAD_S0471632NCAM00546M1.IMG	10:04	32	341.8°	✓	✓	✓	✓
990	NLB_485373518RAD_S0480458NCAM00546M1.IMG	10:07	32	345.0°	✓	✓	✓	✓
997	NLB_485999760RAD_S0481530NCAM00546M1.IMG	11:27	32	348.8°	✓	✓	✓	✓
1000	NLB_486264973RAD_S0481570NCAM00546M1.IMG	11:10	32	350.4°	✓	✓	✓	✓
1027	NLB_488663322RAD_S0481570NCAM00546M2.IMG	11:40	33	4.4°	✓	✓	✓	✓
1039	NLB_489730104RAD_S0481964NCAM00546M1.IMG	12:09	33	10.4°	✓	✓	✓	✓
1047	NLB_490436470RAD_S0482224NCAM00546M1.IMG	11:09	33	14.3°	✓	✓	✓	✓
1052	NLB_490879425RAD_S0482470NCAM00546M1.IMG	10:56	33	16.8°	✓	✓	✓	✓
1055	NLB_491150224RAD_S0482518NCAM00546M1.IMG	12:10	33	18.3°	✓	✓	✓	✓
1071	NLB_492570312RAD_S0490000NCAM00546M1.IMG	12:11	33	25.9°	✓	✓	✓	✓
1077	NLB_493115864RAD_S0490814NCAM00546M1.IMG	15:41	33	28.9°				
1078	NLB_493188243RAD_S0490814NCAM00546M1.IMG	11:17	33	29.2°	✓	✓	✓	✓
1086	NLB_493898203RAD_S0491798NCAM00546M1.IMG	11:16	33	33.0°	✓	✓	✓	✓
1109	NLB_495946761RAD_S0500322NCAM00546M1.IMG	13:13	33	43.7°	✓		✓	
1115	NLB_496476415RAD_S0500592NCAM00546M1.IMG	12:27	33	46.4°	✓	✓	✓	✓
1115	NLB_496476415RAD_S0500592NCAM00546M1.IMG	12:26	33	46.4°				
1128	NLB_497638970RAD_S0500676NCAM00546M1.IMG	14:48	33	52.4°				
1133	NLB_498073487RAD_S0500676NCAM00546M1.IMG	12:18	33	54.6°	✓	✓	✓	✓
1149	NLB_499507414RAD_S0501116NCAM00546M1.IMG	16:01	33	61.9°				
1154	NLB_499939326RAD_S0501624NCAM00546M1.IMG	12:50	33	64.1°	✓	✓	✓	✓
1163	NLB_500745014RAD_S0503076NCAM00546M1.IMG	14:40	33	68.1°				
1171	NLB_501460995RAD_S0510268NCAM00546M1.IMG	16:15	33	71.8°				
1173	NLB_501638216RAD_S0510874NCAM00546M1.IMG	16:11	33	72.6°				
1176	NLB_501874919RAD_S0511102NCAM00546M1.IMG	08:11	33	73.8°				
1188	NLB_502958425RAD_S0512004NCAM00546M1.IMG	13:09	33	79.3°	✓	✓	✓	✓
1194	NLB_503475424RAD_S0512322NCAM00546M1.IMG	08:56	33	81.9°				
1201	NLB_504106540RAD_S0520000NCAM00546M1.IMG	11:34	33	85.1°				
1204	NLB_504383877RAD_S0520000NCAM00546M1.IMG	14:33	33	86.6°				
1206	NLB_504552188RAD_S0520004NCAM00546M1.IMG	12:04	33	87.4°				
1210	NLB_504907902RAD_S0520004NCAM00546M1.IMG	12:14	33	89.2°				
1221	NLB_505886162RAD_S0520936NCAM00546M1.IMG	12:45	33	94.2°	✓	✓	✓	✓
1229	NLB_506599654RAD_S0521162NCAM00546M1.IMG	13:40	33	97.9°	✓	✓	✓	✓
1235	NLB_507109089RAD_S0521162NCAM00546M1.IMG	07:23	33	100.5°				
1241	NLB_507670679RAD_S0521162NCAM00546M1.IMG	15:13	33	103.5°				

Methods are discussed in Ch. 2, Sec. 2.3.

Continued on next page...

Table A.1: ***The Dust Devil Search Movie Dataset for LOS-Ext, cont'd...***

Sol	Image Name	LTST	Date MY	L_S	Method A1	A2	A3	A4
1253	NLB_508729101RAD_S0522388NCAM00546M1.IMG	13:25	33	109.0°	✓	✓	✓	✓
1254	NLB_508816618RAD_S0522388NCAM00546M1.IMG	13:04	33	109.5°	✓	✓	✓	✓
1258	NLB_509152402RAD_S0522678NCAM00546M1.IMG	07:50	33	111.2°				
1265	NLB_509776574RAD_S0530186NCAM00546M1.IMG	08:36	33	114.6°				
1272	NLB_510403365RAD_S0530636NCAM00546M1.IMG	10:04	33	117.9°				
1272	NLB_510413085RAD_S0530636NCAM00546M1.IMG	12:43	33	118.0°	✓	✓	✓	✓
1283	NLB_511401105RAD_S0531756NCAM00546M1.IMG	15:50	33	123.3°				
1292	NLB_512168936RAD_S0532298NCAM00546M1.IMG	07:26	33	127.6°				
1297	NLB_512637524RAD_S0532644NCAM00546M1.IMG	14:08	33	130.2°				
1299	NLB_512813115RAD_S0532980NCAM00546M1.IMG	13:37	33	131.1°	✓	✓	✓	✓
1302	NLB_513061884RAD_S0540000NCAM00546M1.IMG	08:52	33	132.5°				
1306	NLB_513415573RAD_S0540010NCAM00546M1.IMG	08:30	33	134.5°				
1312	NLB_513962912RAD_S0540388NCAM00546M1.IMG	12:30	33	137.6°	✓		✓	
1316	NLB_514320322RAD_S0540412NCAM00546M1.IMG	13:08	33	139.7°	✓		✓	
1328	NLB_515380962RAD_S0540746NCAM00546M1.IMG	11:55	33	145.8°	✓	✓	✓	✓
1331	NLB_515638528RAD_S0540938NCAM00546M1.IMG	09:32	33	147.3°				
1343	NLB_516703533RAD_S0540992NCAM00546M1.IMG	09:29	33	153.6°				
1347	NLB_517052474RAD_S0541490NCAM00546M1.IMG	07:50	33	155.7°				
1350	NLB_517337264RAD_S0541610NCAM00546M1.IMG	12:51	33	157.5°	✓		✓	
1355	NLB_517782202RAD_S0542202NCAM00546M1.IMG	13:09	33	160.2°	✓	✓	✓	✓
1363	NLB_518495731RAD_S0542280NCAM00546M1.IMG	14:04	33	164.6°	✓	✓	✓	✓
1363	NLB_518495731RAD_S0542280NCAM00546M1.IMG	14:03	33	164.6°				
1379	NLB_519898274RAD_S0550310NCAM00546M1.IMG	09:16	33	173.4°				
1381	NLB_520098019RAD_S0550310NCAM00546M1.IMG	15:16	33	174.7°				
1384	NLB_520338588RAD_S0550538NCAM00546M1.IMG	08:18	33	176.2°				
1400	NLB_521759118RAD_S0552098NCAM00546M1.IMG	08:21	33	185.5°				
1401	NLB_521862461RAD_S0552222NCAM00546M1.IMG	12:19	33	186.2°	✓	✓	✓	✓
1413	NLB_522910784RAD_S0560774NCAM00546M1.IMG	07:42	33	193.2°				
1413	NLB_522929160RAD_S0560774NCAM00546M1.IMG	12:41	33	193.4°	✓	✓	✓	✓
1417	NLB_523269740RAD_S0561122NCAM00546M2.IMG	08:45	33	195.7°				
1421	NLB_523642876RAD_S0561236NCAM00546M2.IMG	13:38	33	198.2°	✓	✓	✓	✓
1429	NLB_524352853RAD_S0561632NCAM00546M1.IMG	13:34	33	203.1°	✓	✓	✓	✓
1433	NLB_524693245RAD_S0562428NCAM00546M1.IMG	09:33	33	205.5°				
1440	NLB_525311983RAD_S0571020NCAM00546M1.IMG	08:49	33	209.8°				
1442	NLB_525508830RAD_S0571020NCAM00546M1.IMG	14:01	33	211.2°				
1450	NLB_526209873RAD_S0571942NCAM00546M1.IMG	11:32	33	216.2°	✓	✓	✓	✓
1470	NLB_527987638RAD_S0580264NCAM00546M1.IMG	12:01	33	229.0°	✓	✓	✓	✓
1476	NLB_528520036RAD_S0580912NCAM00546M1.IMG	11:54	33	232.9°	✓	✓	✓	✓
1481	NLB_528961756RAD_S0581248NCAM00546M2.IMG	11:17	33	236.1°	✓	✓	✓	✓
1485	NLB_529301951RAD_S0581572NCAM00546M1.IMG	07:12	33	238.6°				
1493	NLB_530040256RAD_S0582046NCAM00546M1.IMG	14:43	33	244.0°				
1499	NLB_530547342RAD_S0582046NCAM00546M1.IMG	07:45	33	247.7°				
1499	NLB_530562397RAD_S0582046NCAM00546M1.IMG	11:50	33	247.8°	✓	✓	✓	✓
1509	NLB_531448862RAD_S0590936NCAM00546M1.IMG	11:23	33	254.3°	✓	✓	✓	✓

Methods are discussed in Ch. 2, Sec. 2.3.

Continued on next page...

Table A.1: ***The Dust Devil Search Movie Dataset for LOS-Ext, cont'd...***

Sol	Image Name	Date LTST	Date MY	Date L_S	Method A1	Method A2	Method A3	Method A4
1521	NLB_532520735RAD_S0592578NCAM00546M1.IMG	13:01	33	262.2°	✓	✓	✓	✓
1529	NLB_533215521RAD_S0592830NCAM00546M1.IMG	08:45	33	267.3°				
1532	NLB_533496862RAD_S0592830NCAM00546M1.IMG	12:47	33	269.3°	✓	✓	✓	✓
1541	NLB_534293228RAD_S0592830NCAM00546M1.IMG	11:58	33	275.1°	✓	✓	✓	✓
1544	NLB_534543053RAD_S0592830NCAM00546M1.IMG	07:28	33	276.9°				
1555	NLB_535535395RAD_S0593004NCAM00546M1.IMG	11:38	33	284.0°	✓	✓	✓	✓
1559	NLB_535872343RAD_S0593016NCAM00546M1.IMG	06:41	33	286.5°				
1565	NLB_536423339RAD_S0593016NCAM00546M1.IMG	11:36	33	290.4°	✓	✓	✓	✓
1582	NLB_537931696RAD_S0600888NCAM00546M1.IMG	11:15	33	300.9°	✓	✓	✓	✓

Methods are discussed in Ch. 2, Sec. 2.3.

Table A.2: ***The North Crater Rim Extinction Dataset for LOS-Ext.***

Sol	Image Name	Date LTST	Date MY	Date L_S	Method A1	Method A2	Method A3	Method A4
1613	NRB_540690692RAD_M0610924NCAM00580M1.IMG	12:59	33	319.5°	✓	✓	✓	✓
1621	NRB_541382318RAD_M0611140NCAM00580M1.IMG	07:57	33	324.0°				
1631	NRB_542285022RAD_M0611650NCAM00580M1.IMG	11:59	33	329.8°	✓	✓	✓	✓
1641	NRB_543175394RAD_M0612472NCAM00580M1.IMG	12:42	33	335.5°	✓	✓	✓	✓
1652	NRB_544149633RAD_M0620108NCAM00580M2.IMG	12:06	33	341.5°	✓	✓	✓	✓
1658	NRB_544664517RAD_M0620108NCAM00580M1.IMG	07:19	33	344.7°				
1658	NRB_544685742RAD_M0620108NCAM00580M1.IMG	13:03	33	344.8°	✓	✓	✓	✓
1661	NRB_544952831RAD_M0620444NCAM00580M1.IMG	13:16	33	346.4°	✓	✓	✓	✓
1671	NRB_545853934RAD_M0621140NCAM00580M1.IMG	16:55	33	351.8°				
1675	NRB_546176622RAD_M0621386NCAM00580M1.IMG	08:10	33	353.7°				
1683	NRB_546912419RAD_M0622726NCAM00580M1.IMG	15:08	33	358.0°				
1692	NRB_547686238RAD_M0630100NCAM00580M1.IMG	08:23	34	2.5°				
1701	NRB_548500769RAD_M0631420NCAM00580M1.IMG	12:38	34	7.1°	✓	✓	✓	✓

Methods are discussed in Ch. 2, Sec. 2.3.

A.2 Mastcam Images

Table A.3: ***The Mastcam Crater Rim Extinction Dataset***

Sol	M34 Image Name (_DRXX.IMG)	M100 Image Name (_DRXX.IMG)	Date LTST	Date MY	Date L_S
939	0939ML0040960000403024E01	0939MR0040960000501926E01	12:16	32	316.3°
941	0941ML0041350000403074E01	0941MR0041350000501941E01	06:52	32	317.4°
943	0943ML0041450000403135E01	0943MR0041450000501993E01	12:44	32	318.7°
945	0945ML0041530000403184E01	0945MR0041530000501998E01	11:13	32	319.8°

Continued on next page...

Table A.3: ***The Mastcam Crater Rim Extinction Dataset, cont'd...***

Sol	M34 Image Name (_DRXX.IMG)	M100 Image Name (_DRXX.IMG)	Date LTST	MY	L_S
966	0966ML0042810000403968E01	0966MR0042810000502572E01	15:38	32	332.0°
971	0971ML0042860000404113E01	0971MR0042860000502722E01	10:55	32	334.7°
975	0975ML0042960000404137E01	0975MR0042960000502729E01	07:13	32	336.8°
975	0975ML0042980000404141E01	0975MR0042980000502731E01	10:22	32	336.9°
981	0981ML0043310000404307E01	0981MR0043310000502868E01	09:52	32	340.1°
985	0985ML0043470000404355E01	0985MR0043470000502957E01	11:45	32	342.4°
988	0988ML0043670000404450E02	0988MR0043670000503067E01	13:01	32	344.0°
994	0994ML0044010000404913E01	0994MR0044010000503373E01	11:55	32	347.2°

B Calculating the Distance to the Crater Rim

B.1 Virtual Image

A virtual Navcam image using the Digital Elevation Model (DEM) from HRSC onboard Mars Express is constructed on a per location basis to quantify the path length between the rover and the crater rim. Ideally, these virtual images will look similar to the landscapes portrayed by Navcam. This section will detail the process to create the virtual images, show how well the virtual images are able to recreate the Martian landscape from the rovers point-of-view.

It is possible to determine the pixel position of the rover on the DEM for every observation. Due to a resolution of 50-m/pixel for the DEM, multiple observations can be represented as the same location on the DEM. As such, a list of unique rover locations on the DEM is compiled, and henceforth referred to as zones. A virtual image is made for the entire dataset. The dataset spans 72 zones.

A subset of the DEM is read into Matlab for each zone consisting of a 45° wedge radiating to the north with the camera located at the vertex. To recreate a Navcam Image the DEM is projected onto the surface Mars and elevation data is transformed from physical size to

angular size.

The DEM is a flat projection of a curved surface. As such, the effects of Mars curvature must be considered as the landscape bends away from the point-of-view of an observer on the surface. In the north-south direction Mars polar radius, $r_{\male,p} = 3375km$, is used to correct the elevations with the following formula:

$$z_{NS}(i,:) = z(i,:) - r_{\male,p} \cdot (1 - \cos\theta_i) \tag{B.1}$$

where z is the elevation data, $(i,:)$ references the row of the DEM matrix, and the θ_i term refers to the angle made in reference to the center of Mars from the observation point to the rows in the DEM. Elevations in the East-West direction are corrected for in a similar way using:

$$z_{EW}(:,j) = z_{NS}(:,j) - r_{\male,4.6^\circ} \cdot (1 - \cos\theta_j) \tag{B.2}$$

only this time, the radius of a great circle on Mars at the MSL latitude, e.g. $r_{\male,4.6^\circ} = 3385$ km, is used, j references the columns, and hence θ_j is the angle made in reference to the center of the great circle between the observation point and the column in the DEM.

To obtain a Martian landscape that an on-the-ground observer may see, the elevation data are converted into angular size. Smaller features close to the observer may have a larger angular size than a large feature at a greater distance. The elevation data are converted to angular size calculated on a pixel-by-pixel basis using:

$$\delta(x,y) = \tan^{-1}\left(\frac{\Delta z}{d(x,y)}\right) \tag{B.3}$$

where, x and y refer to the pixel position (with the set pair $[x, y] = [1, 1]$ being the top left corner of the DEM), z is the elevation data from the DEM, Δz is the difference in elevation between the observation point (virtual camera) and the reference point, e.g. $\Delta z = \mid z(x, y) - z(x_o, y_o) \mid$, and $d(x, y)$ is the distance from the observation point to the reference point, calculated using the Pythagorean theorem and multiplying by the spatial resolution of the DEM.

The last step is to stretch the 45° wedge to fill the virtual camera frame using interpolated elevation values to fill in the gaps. Figure shows the end result, a near perfect representation of the Martian landscape and compares it to that of a Navcam image taken from the same zone. The virtual image and the Navcam image are very similar, albeit offset from one another.

B.2 Derivation of Distances

A correlation between the Navcam frames and the virtual images can be made. The point with the largest angular size within the Navcam frame matches the point with the largest angular size within the virtual image, as seen in Figure B.1 . An algorithm to determine the distance to specific pixels in the Navcam image is detailed below:

The region starts a known number of pixels below the highest point of the crater rim in the image. The highest peak in the Navcam image is the same as the highest angular size determined from the DEM. As such, to find the region of interest on the DEM, the rows of

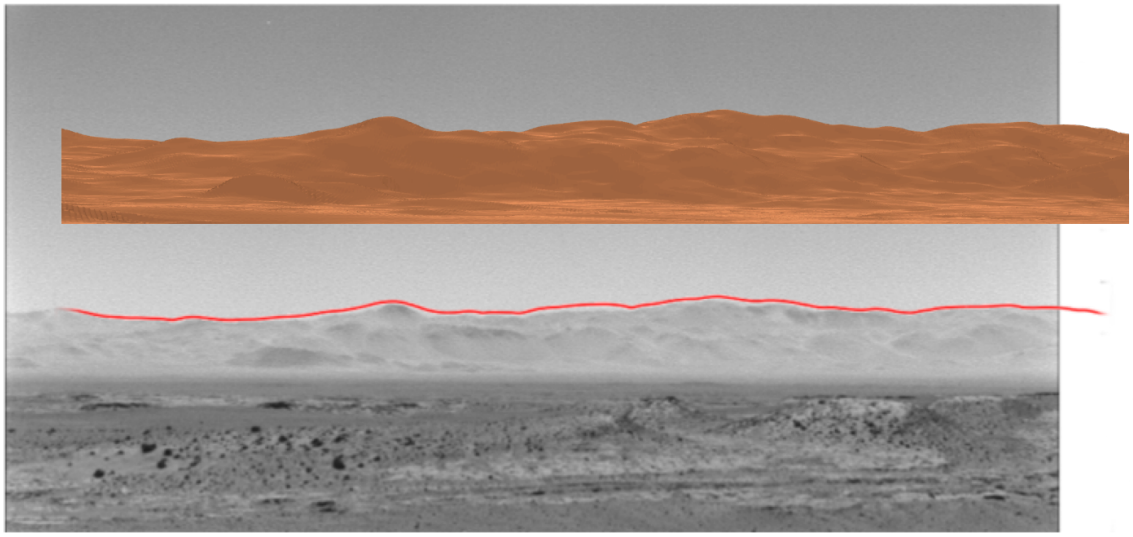

Figure B.1: ***DEM Derived Image Compared to Navcam Image***

The image derived from the DEM is shown superimposed on a Navcam image of the crater rim taken on Sol 635. A red line outlines the crater rim. The features in the virtual image and the Navcam images match each other very well, with a small horizontal offset. The product ID can be found in Appendix A.

pixels on the Navcam image need to be converted into an angular elevation using:

$$\delta_n = \delta_{max} - \theta \Delta h_n \tag{B.4}$$

here n are the rows from the image we are interested in δ_{max} is the maximum angular height from the DEM, θ is the vertical angular resolution of the Navcam image, and $\Delta h_n = | h_{max} - h_n |$ is the difference in pixel number between the largest feature and the row of interest.

A series of contour maps are created using the δ_n as the elevation. Column-by-column, the contour for each elevation closest to the observation point is recorded and a distance is attributed to it, again, using the Pythagorean theorem and the resolution of the DEM.

C Ball Bearing Experiment and Simulation

The transmission spectroscopy setup detailed in Chapter 4, Section 4.1 was also used to observe the transmission properties of 1.0-mm diameter reflective steel ball bearings. The ball bearings were placed on a glass surface and confined to an ø2 optical tube spacer, a black 2-inch diameter 2-mm tall, circular barrier, e.g. Figure C.1. The ball bearings are hexagonally packed in one layer, e.g. Figure C.2.

Transmission spectra were collected for zenith angles ranging from $0 - 40°$, however, this time spectra were collected for every 10° in the azimuth. Initially, this was done to conserve the amount of times the experiment needed to run, e.g. if the arrangement of the particles is static, as shown in Figures C.1 and C.2, then the observed transmittance should also be the same for the three runs.

During the experiment, it was noticed that there was a repeatable azimuthal component to the amount of light being transmitted through the setup. In hindsight, collecting data for every 10° instead of the standard 30° allowed the azimuthal component of the transmission to be better understood.

The majority of the transmitted light comes from photons that do not interact with the steel ball bearings at all, e.g. the gaps between the spheres as seen in Fig. C.2. The

Figure C.1: ***Experimental Setup: Packed Ball Bearings***

Image showing the ball bearings packed hexagonally confined to a circular barrier.

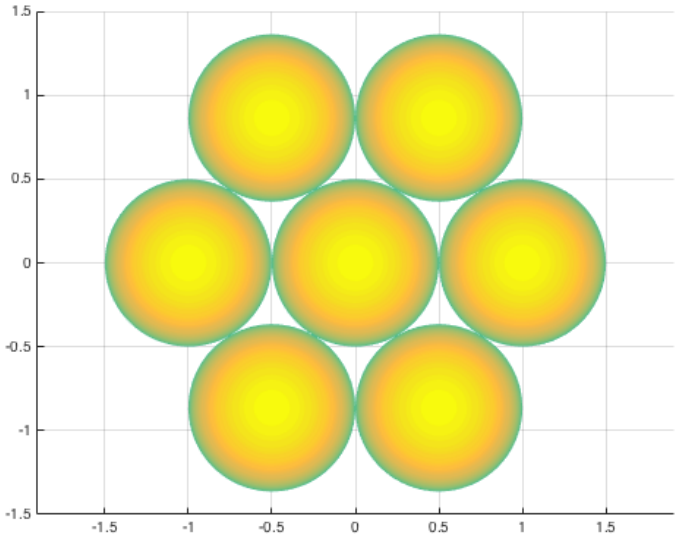

Figure C.2: ***Hexagonally Packed Spheres***

Diagram of hexagonally packed spheres, six spheres surround a central sphere. The central sphere touches each surrounding sphere at one point.

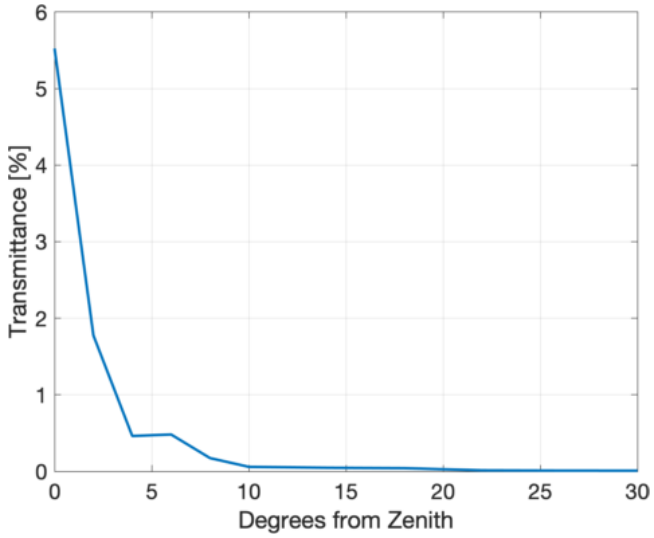

Figure C.3: ***Transmittance of Hexagonally Packed Ball Bearings***

Transmittance recorded with the mini-goniometer setup for 1.0-mm diameter steel ball bearings. Binned in 10° *azimuthally and elevations of* 0°, 2°, 4°, 6°, 8°, 10°, 14°, 18°, 22°, 26°, 30°.

transmission signal received can be seen in Figure C.3 in which the photons are azimuthally averaged for their respective elevations.

Assuming the ball bearings are perfect spheres, it is possible to treat this situation numerically, in which a photon hits the sphere and is reflected specularly. The unit normal reflection vector is defined mathematically as:

$$\hat{\mathbf{u}}_\mathbf{e} = \hat{\mathbf{u}}_\mathbf{i} - 2|\hat{\mathbf{u}}_\mathbf{i} \cdot \hat{\mathbf{x}}_\mathbf{s}|\hat{\mathbf{x}}_\mathbf{s} \tag{C.1}$$

Where $\hat{\mathbf{u}}_\mathbf{i}$ is the unit normal incident photon direction vector, $\hat{\mathbf{x}}_\mathbf{s}$ is the unit normal to the surface on the sphere the photon hits.

This was implemented as a three-dimensional numerical simulation in Matlab and was

allowed to run for several hundred thousand photons. The simulation preserves the geometry of the setup, each ball bearing has a radius of 0.5 mm and the ball bearings are hexagonally packed in one layer. The following sections detail how the simulation works and how the simulation and experimental results compare.

C.1 Initial State

Unlike the experimental, in which the ball bearings were confined to a circular barrier, the ball bearings in the simulation were situated in a rectangle roughly 50 mm $\times$ 44 mm. This is due to the hexagon packing scheme and the initial choice of how to set up the particles.

The ball bearings are placed in the X-Y plane. The central ball bearing is situated at the origin. There are 25 ball bearings placed surface-to-surface in the positive and negative x-direction, this has been termed row-zero. Rows 1 and -1, e.g. one row above and below row-zero, consist of 25 ball bearings in the positive and negative x-direction, again, placed surface-to-surface, meeting at the y-axis, termed row-one. The hexagonal packing defines the y-coordinate of each successive row as $y = \sqrt{3}nr$, where n is the row number and r is the radius of the ball bearing. Even rows, e.g. $[\pm 2, \pm 4, \pm 6, ..., \pm 24]$, are copies of row-zero at their respective y-coordinate. Odd rows, e.g. $[\pm 3, \pm 5, \pm 6, ..., \pm 25]$, are copies of row-one at their respective y-coordinate. There are 51 rows, even rows consist of 51 ball bearings and odd rows consist of 50 ball bearings. A schematic of the ball bearings in the numerical simulation can be seen in Figure C.4.

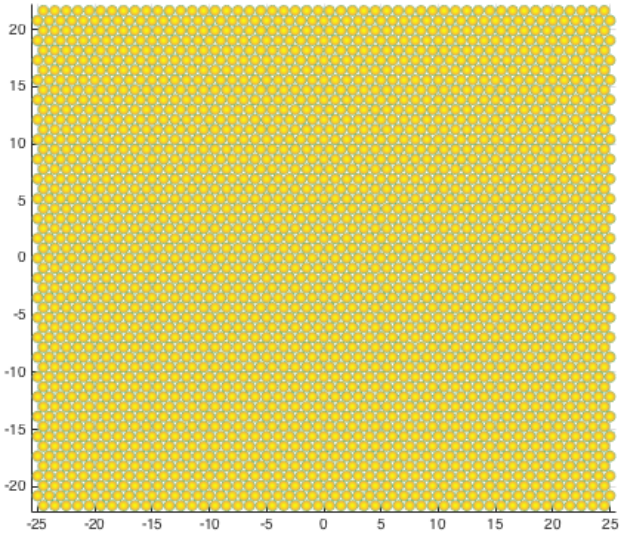

Figure C.4: ***Ball Bearing Placement in Numerical Simulation***

Visual representation of the ball bearing placement in the numerical simulation run to compare to the experimental work. The ball bearings are hexagonally packed and in the xy-plane.

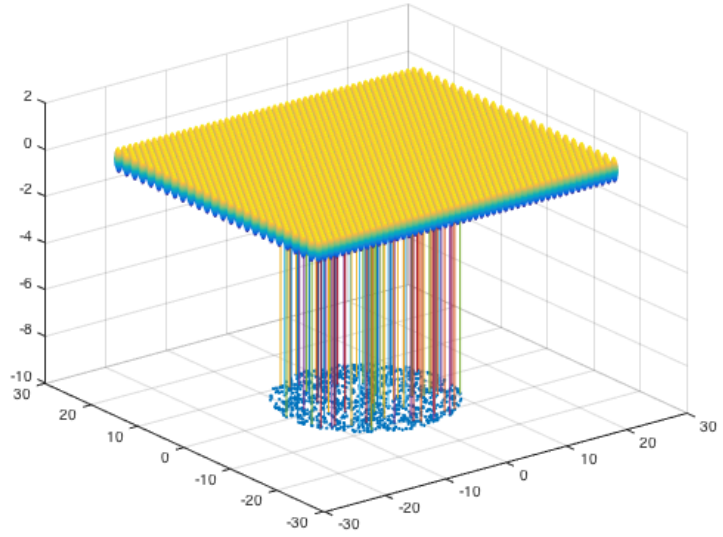

Figure C.5: ***Initial Photon Position and Displacement Vectors***

The dots below the spheres represent 1000 randomly generated photon positions, also shown here are displacement vectors for 100 of the photons. All photons in the initial state have the same displacement vector, $\tilde{\mathbf{u}} = [0 \cdot \hat{\mathbf{x}}, 0 \cdot \hat{\mathbf{y}}, 1 \cdot \hat{\mathbf{z}}]$*, e.g. perpendicular to the xy-plane and hitting the spheres from below.*

C.2 Run Time: The Not-So-Random Walk

At run time photons are randomly generated within a circle below the surface of ball bearings. The circle defines the edges of the incident beam of light coming from the light source in the experimental setup. The photons are collimated and so travel normal to x-y plane, e.g. $\tilde{\mathbf{u}} = [0 \cdot \hat{\mathbf{x}}, 0 \cdot \hat{\mathbf{y}}, 1 \cdot \hat{\mathbf{z}}]$.

Figure C.5 shows the initial position and direction vectors for 100 randomly generated photons placed below the sample.

The program checks if the photon will intersect a ball bearing, if the photon does not,

it will escape the system and be detected at an elevation of 0° measured from zenith. If however, the photon does interact with a ball bearing, the reflection vector is computed as in Eq. C.1. The photon then travels along this new path and the program determines if the photon interacts with a new ball bearing, if no interaction occurs, the photon, will escape the system and the program will record its azimuth and elevation. This process is allowed to repeat up to 100 times. In theory, one would not expect 100 reflections to take place in this simple scenario. During runtime, it is observed that about 0.03% of the particles required more than 20 bounces. It did not add any significant compute time to increase the number of bounces, especially since only 0.03% of photons required more than 20 bounces.

Figure C.6 shows the resulting interactions of the first 1000 randomly generated photons. It becomes quite clear that the majority of the photons eventually leave the system with an elevation angle $> 90°$, that is, the majority of photons are not transmitted through the bed of ball bearings. In this particular run, for only 1000 photons, only

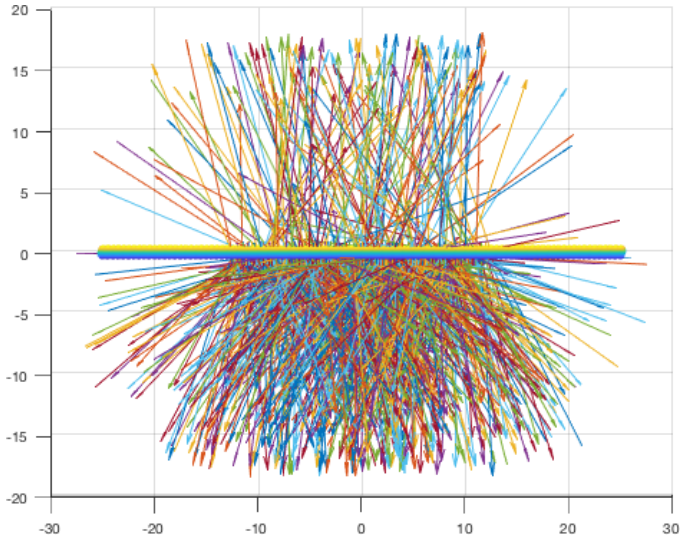

Figure C.6: ***Transmission and Reflection of Photons within the Numerical Simulation***

Visual representation of 1000 scattering photons in the numerical simulation. Each photon's path is plotted here, but is undetectable at this resolution. Note the majority of photons are reflected at elevation angles $> 90°$.

D Regolith and Rock Sample Tables

D.1 Regolith

Table D.1: ***Regolith Samples: Grain Sizes, Zenith Angles and Optical Depth***

Basalt	Medium	Thickness: 0.5 mm									
Run 1	Z.A.:	0°	2°	4°	6°	8°	10°	14°	20°	28°	38°
	O.D.:	0.5	0.5	0.5	0.3	0	0	0	0	0	0
Run 2	Z.A.:	0°	2°	4°	6°	8°	10°	14°	20°	28°	38°
	O.D.:	0	0	0	0	0	0	0	0	0	0
Run 3	Z.A.:	0°	2°	4°	6°	8°	10°	14°	20°	28°	38°
	O.D.:	0	0	0	0	0	0	0	0	0	0
Calcite	Thickness: 0.5 mm										
Run 1	Z.A.:	0°	2°	4°	6°	8°	10°	14°	18°	22°	26°	30°
	O.D.:	2	2	2	2	2	2	2	2	2	2	2
Run 2	Z.A.:	0°	2°	4°	6°	8°	10°	14°	20°	28°	38°	48°
	O.D.:	2	2	2	2	2	2	2	2	2	2	2
Run 3	Z.A.:	0°	2°	4°	6°	8°	10°	14°	20°	28°	38°	48°
	O.D.:	2	2	2	2	2	2	2	2	2	2	2
Cheto bentonite	Thickness: 0.5 mm										
Run 1	Z.A.:	0°	2°	4°	6°	8°	10°	14°	18°	22°	
	O.D.:	0.5	0.5	0.5	0.5	0.5	0.5	0.5	0.5	0.5	
Run 2	Z.A.:	0°	2°	4°	6°	8°	10°	14°	18°	22°	30°	40°
	O.D.:	1	1	1	1	1	1	1	1	1	1	1
Run 3	Z.A.:	0°	2°	4°	6°	8°	10°	14°	18°	22°	30°	40°
	O.D.:	0.6	0.6	0.6	0.6	0.6	0.6	0.6	0.5	0.5	0.5	0.5
JSC Mars-1	150 μm	Thickness: 0.5 mm									
Run 1	Z.A.:	0°	4°	6°	8°	10°	12°	14°	16°		
	O.D.:	0	0	0	0	0	0	0	0		

Continued on next page...

Table D.1: ***Regolith Samples, cont'd...***

JSC Mars-1	250 μm	Thickness: 0.5 mm								
Run 1	Z.A.:	0°	2°	4°	6°	8°	10°			
	O.D.:	0	0	0	0	0	0			
Run 2	Z.A.:	0°	2°	4°	6°	8°	10°			
	O.D.:	0	0	0	0	0	0			
Run 3	Z.A.:	0°	2°	4°	6°	8°	10°			
	O.D.:	0	0	0	0	0	0			
JSC Mars-1	250 μm	Thickness: 1.0 mm								
Run 1	Z.A.:	0°	2°	4°	6°	8°	10°			
	O.D.:	0	0	0	0	0	0			
Run 2	Z.A.:	0°	2°	4°	6°	8°	10°	14°	20°	
	O.D.:	1	1	1	1	1	1	0	0	
Run 3	Z.A.:	0°	2°	4°	6°	8°	10°	14°	20°	
	O.D.:	0.5	0.5	0.5	0.5	0	0	0	0	
JSC Mars-1	355 μm	Thickness: 0.5 mm								
Run 1	Z.A.:	0°	2°	4°	8°	16°	24°	32°	40°	
	O.D.:	3	3	3	1.6	0.6	0.6	0	0	
Run 2	Z.A.:	0°	2°	4°	6°	8°	10°	14°		
	O.D.:	0.5	0.5	0.5	0	0	0	0		
Run 3	Z.A.:	0°	2°	4°	6°	8°	10°	14°	20°	
	O.D.:	1.4	1.4	1.6	1.6	1.6	0	0	0	
JSC Mars-1	355 μm	Thickness: 1.0 mm								
Run 1	Z.A.:	0°	2°	4°	6°	8°	16°	24°	32°	40°
	O.D.:	1	1	1	1	1	1	0	0	0
Run 2	Z.A.:	0°	2°	4°	6°	8°	10°	14°	20°	
	O.D.:	2.2	2.4	2.4	2.4	2.4	1	1	0	
Run 3	Z.A.:	0°	2°	4°	6°	8°	10°	14°	20°	
	O.D.:	2.5	2.5	2.5	2.5	2.5	0.5	0.5	0.2	
JSC Mars-1	500 μm	Thickness: 1.0 mm								
Run 1	Z.A.:	0°	2°	4°	6°	8°	16°	24°	32°	40°
	O.D.:	4	4	4	4	3	1	0.6	0.6	0.4
Run 2	Z.A.:	0°	2°	4°	6°	8°	10°	14°	20°	
	O.D.:	3.2	3.2	3.2	3.2	1.2	1.2	1.2	0.5	
Run 3	Z.A.:	0°	2°	4°	6°	8°	10°	14°	20°	
	O.D.:	3.3	3.3	3.3	3.3	1.7	1.7	1	0.4	
JSC Mars-1	500 μm	Thickness: 2.0 mm								
Run 1	Z.A.:	0°	2°	4°	6°	8°	10°	16°	24°	32°	40°
	O.D.:	1	1	1	1	0	0	0	0	0	0

Continued on next page...

Table D.1: ***Regolith Samples, cont'd...***

JSC Mars-1	600 μm		Thickness: 1.0 mm								
Run 1	Z.A.:	0°	2°	4°	6°	8°	16°	24°	32°	40°	
	O.D.:	2.4	2.4	2.4	2.2	2.2	1	0	0	0	
Run 2	Z.A.:	0°	2°	4°	6°	8°	10°	14°	20°		
	O.D.:	3.4	3.4	3.5	3.5	2.2	1.6	0.7	0.7		
Run 3	Z.A.:	0°	2°	4°	6°	8°	10°	14°	20°		
	O.D.:	3.2	3.2	3.4	3.4	1.8	1	1	0.5		
JSC Mars-1	600 μm		Thickness: 2.0 mm								
Run 1	Z.A.:	0°	2°	4°	6°	8°	16°	24°	32°	40°	
	O.D.:	1.2	1.2	1.2	1	0	0	0	0	0	
JSC Mars-1	850 μm		Thickness: 1.0 mm								
Run 1	Z.A.:	0°	2°	4°	8°	16°	24°	32°	40°		
	O.D.:	4	4	4	3	1	1	0.5	0.5		
Run 2	Z.A.:	0°	2°	4°	6°	8°	16°	24°			
	O.D.:	4.2	4.2	4.2	4.2	2.8	0.8	0.8			
Run 3	Z.A.:	0°	2°	4°	6°	8°	16°	24°			
	O.D.:	4.5	4.5	4.5	4.5	2.6	1	1			
JSC Mars-1	850 μm		Thickness: 2.0 mm								
Run 1	Z.A.:	0°	2°	4°	8°	16°	24°	32°	40°		
	O.D.:	4	4	4	3	1	1	0.5	0.5		
JSC Mars-1	Unsieved		Thickness: 0.5 mm								
Run 1	Z.A.:	0°	2°	4°	6°	8°	16°	24°	32°	40°	
	O.D.:	2.5	2.5	2	2	0.6	0	0	0	0	
Run 2	Z.A.:	0°	2°	4°	6°	8°	10°	14°			
	O.D.:	0	0	0	0	0	0	0			
Run 3	Z.A.:	0°	2°	4°	6°	8°	10°	14°			
	O.D.:	0.2	0.2	0	0	0	0	0			
Kieserite			Thickness: 0.5 mm								
Run 1	Z.A.:	0°	2°	4°	6°	8°	10°	14°	20°	28°	38°
	O.D.:	2	2	2	2	2	2	2	2	2	2
Run 2	Z.A.:	0°	2°	4°	6°	8°	10°	14°	20°	28°	38°
	O.D.:	2	2	2	2	2	2	2	2	2	2
Run 3	Z.A.:	0°	2°	4°	6°	8°	10°	14°	20°	28°	38°
	O.D.:	2	2	2	2	2	2	2	2	2	2
Kieserite			Thickness: 1.0 mm								
Run 1	Z.A.:	0°	2°	4°	6°	8°	10°	14°	20°	28°	38°	48°
	O.D.:	2	2	2	2	2	2	2	2	2	2	2

Continued on next page...

Table D.1: ***Regolith Samples, cont'd...***

Run 2	Z.A.:	0°	2°	4°	6°	8°	10°	14°	20°	28°	38°	48°
	O.D.:	1.4	1.4	1.4	1.4	1.4	1.4	1.4	1.4	1.4	1.4	1.4
Run 3	Z.A.:	0°	2°	4°	6°	8°	10°	14°	20°	28°	38°	48°
	O.D.:	1.7	1.7	1.7	1.7	1.7	1.7	1.7	1.7	1.7	1.7	1.7

D.2 Haughton Impact Crater Rock Samples

Table D.2: ***Rock Samples: Porosity, Shock, Zenith Angles and Optical Depth***

BE 009 A1	Shock: 5-6 (high)							Thickness: 0.5 mm			
Run 1	Z.A.:	0°	2°	4°	6°	8°	10°	14°	18°	22°	26°	30°
	O.D.:	1	1	1	1	1	1	1	1	0	0	0
Run 2	Z.A.:	0°	2°	4°	6°	8°	10°	14°	18°	22°	26°	30°
	O.D.:	0.3	0.8	0.8	0.3	0.3	0	0	0	0	0	0
Run 3	Z.A.:	0°	2°	4°	6°	8°	10°	14°	18°	22°	26°	30°
	O.D.:	1.2	1.3	1.3	1	1	0.6	0.6	0.6	0.6	0.6	0.6
BE 009 A1	Shock: 5-6 (high)							Thickness: 1.0 mm			
Run 1	Z.A.:	0°	2°	4°	6°	8°	10°	14°	18°	22°	26°	30°
	O.D.:	0	0	0	0	0	0	0	0	0	0	0
BE 009 A13	Shock: low (1-2)							Thickness: 0.5 mm			
Run 1	Z.A.:	0°	2°	4°	6°	8°	10°	14°	18°	22°	26°	30°
	O.D.:	0	0	0	0	0	0	0	0	0	0	0
Run 2	Z.A.:	0°	2°	4°	6°	8°	10°	14°	18°	22°	26°	30°
	O.D.:	0	0	0	0	0	0	0	0	0	0	0
Run 3	Z.A.:	0°	2°	4°	6°	8°	10°	14°	18°	22°	26°	30°
	O.D.:	0	0	0	0	0	0	0	0	0	0	0
BE 009 A13	Shock: low (1-2)							Thickness: 1.0 mm			
Run 1	Z.A.:	0°	2°	4°	6°	8°	10°	14°	18°	22°	26°	30°
	O.D.:	0	0	0	0	0	0	0	0	0	0	0
Run 2	Z.A.:	0°	2°	4°	6°	8°	10°	14°	18°	22°	26°	30°
	O.D.:	0	0	0	0	0	0	0	0	0	0	0
Run 3	Z.A.:	0°	2°	4°	6°	8°	10°	14°	18°	22°	26°	30°
	O.D.:	0	0	0	0	0	0	0	0	0	0	0
BE 009 A14	Shock: 5-6 (high)							Thickness: 0.5 mm			
Run 1	Z.A.:	0°	2°	4°	6°	8°	10°	14°	18°	22°	26°	30°
	O.D.:	1	1	1	1	1	1	1	1	1	1	1
Run 2	Z.A.:	0°	2°	4°	6°	8°	10°	14°	18°	22°	26°	30°
	O.D.:	1.5	1.5	1	0.3	0.3	0.3	0.3	0.3	0.3	0.3	0.3

Continued on next page...

Table D.2: *Rock Samples, cont'd...*

Run 3	Z.A.:	0°	2°	4°	6°	8°	10°	14°	18°	22°	26°	30°
	O.D.:	2.5	2	1	1	1	0.3	0.3	0.6	0.3	0.1	0
BE 009 A14	Shock: 5-6 (high)							Thickness: 1.0 mm				
Run 1	Z.A.:	0°	2°	4°	6°	8°	10°	14°	18°	22°	26°	30°
	O.D.:	0.3	0.3	0.3	0.3	0.3	0.3	0.3	0.3	0.3	0.3	0.3
Run 2	Z.A.:	0°	2°	4°	6°	8°	10°	14°	18°	22°	26°	30°
	O.D.:	0	0	0	0	0	0	0	0	0	0	0
Run 3	Z.A.:	0°	2°	4°	6°	8°	10°	14°	18°	22°	26°	30°
	O.D.:	0	0	0	0	0	0	0	0	0	0	0
BE 010 A	Shock: 2-3 (low)							Thickness: 0.5 mm				
Run 1	Z.A.:	0°	2°	4°	6°	8°	10°	14°	18°	22°	26°	30°
	O.D.:	0.3	0.3	0.3	0.3	0.3	0.3	0.3	0.3	0.3	0.3	0.3
Run 2	Z.A.:	0°	2°	4°	6°	8°	10°	14°	18°	22°	26°	30°
	O.D.:	0	0	0	0	0.3	0.3	0.3	0.3	0.3	0.3	0.3
Run 3	Z.A.:	0°	2°	4°	6°	8°	10°	14°	18°	22°	26°	30°
	O.D.:	2.5	2	0.6	0	0.5	0	0.3	0.3	0	0	0
BE 010 A	Shock: 2-3 (low)							Thickness: 1.0 mm				
Run 1	Z.A.:	0°	2°	4°	6°	8°	10°	14°	18°	22°	26°	30°
	O.D.:	1	1	1	1	1	1	1	1	0	0	0
DI 08091	Shock: 4 (medium)							Thickness: 0.5 mm				
Run 1	Z.A.:	0°	2°	4°	6°	8°	10°	14°	18°	22°	26°	30°
	O.D.:	0.3	0.3	0.3	0.3	0.3	0.3	0.3	0.3	0.3	0.3	0.3
Run 2	Z.A.:	0°	2°	4°	6°	8°	10°	14°	18°	22°	26°	30°
	O.D.:	0.3	0.3	0.3	0.3	0.3	0.3	0.3	0.3	0.3	0.3	0.3
Run 3	Z.A.:	0°	2°	4°	6°	8°	10°	14°	18°	22°	26°	30°
	O.D.:	0.6	0.6	0.6	0.6	0.6	0.6	0.6	0.6	0.6	0.6	0.6
DI 08091	Shock: 4 (medium)							Thickness: 1.0 mm				
Run 1	Z.A.:	0°	2°	4°	6°	8°	10°	14°	18°	22°	26°	30°
	O.D.:	0	0	0	0	0	0	0	0	0	0	0
Run 2	Z.A.:	0°	2°	4°	6°	8°	10°	14°	18°	22°	26°	30°
	O.D.:	0	0	0	0	0	0	0	0	0	0	0
Run 3	Z.A.:	0°	2°	4°	6°	8°	10°	14°	18°	22°	26°	30°
	O.D.:	0	0	0	0	0	0	0	0	0	0	0
HMP 00214	Shock: low (1-2)							Thickness: 0.5 mm				
Run 1	Z.A.:	0°	2°	4°	6°	8°	10°	14°	18°	22°	26°	30°
	O.D.:	0.6	0.6	0.6	0.6	0.6	0.6	0.6	0.6	0.6	0.6	0.6
Run 2	Z.A.:	0°	2°	4°	6°	8°	10°	14°	18°	22°	26°	30°
	O.D.:	0.6	0.6	0.6	0.6	0.6	0.6	0.6	0.6	0.6	0.6	0.6
Run 3	Z.A.:	0°	2°	4°	6°	8°	10°	14°	18°	22°	26°	30°
	O.D.:	0.6	0.6	0.6	0.6	0.6	0.6	0.6	0.6	0.6	0.6	0.6

Continued on next page...

Table D.2: *Rock Samples, cont'd...*

HMP 00214		Shock: low (1-2)						Thickness: 1.0 mm				
Run 1	Z.A.:	0°	2°	4°	6°	8°	10°	14°	18°	22°	26°	30°
	O.D.:	0	0	0	0	0	0	0	0	0	0	0
Run 2	Z.A.:	0°	2°	4°	6°	8°	10°	14°	18°	22°	26°	30°
	O.D.:	0	0	0	0	0	0	0	0	0	0	0
Run 3	Z.A.:	0°	2°	4°	6°	8°	10°	14°	18°	22°	26°	30°
	O.D.:	0	0	0	0	0	0	0	0	0	0	0
SI 001 A		Shock: low (2-3)						Thickness: 0.5 mm				
Run 1	Z.A.:	0°	2°	4°	6°	8°	10°	14°	18°	22°	26°	30°
	O.D.:	0.6	0.6	0.6	0.6	0.6	0.6	0.6	0.6	0.6	0.6	0.6
Run 2	Z.A.:	0°	2°	4°	6°	8°	10°	14°	18°	22°	26°	30°
	O.D.:	0.6	0.6	0.6	0.6	0.6	0.6	0.6	0.6	0.6	0.6	0.6
Run 3	Z.A.:	0°	2°	4°	6°	8°	10°	14°	18°	22°	26°	30°
	O.D.:	0.6	0.6	0.6	0.6	0.6	0.6	0.6	0.6	0.6	0.6	0.6
SI 001 A		Shock: low (2-3)						Thickness: 1.0 mm				
Run 1	Z.A.:	0°	2°	4°	6°	8°	10°	14°	18°	22°	26°	30°
	O.D.:	0.6	0.6	0.6	0.6	0.6	0.6	0.6	0.6	0.6	0.6	0.6
Run 2	Z.A.:	0°	2°	4°	6°	8°	10°	14°	18°	22°	26°	30°
	O.D.:	0.6	0.6	0.6	0.6	0.6	0.6	0.6	0.6	0.6	0.6	0.6
Run 3	Z.A.:	0°	2°	4°	6°	8°	10°	14°	18°	22°	26°	30°
	O.D.:	0.6	0.6	0.6	0.6	0.6	0.6	0.6	0.6	0.6	0.6	0.6
SI 001 B		Shock: low (1-2)						Thickness: 0.5 mm				
Run 1	Z.A.:	0°	2°	4°	6°	8°	10°	14°	18°	22°	26°	30°
	O.D.:	0.6	0.6	0.6	0.6	0.6	0.6	0.6	0.6	0.6	0.6	0.6
Run 2	Z.A.:	0°	2°	4°	6°	8°	10°	14°	18°	22°	26°	30°
	O.D.:	1	1	1	1	1	1	1	1	1	1	1
Run 3	Z.A.:	0°	2°	4°	6°	8°	10°	14°	18°	22°	26°	30°
	O.D.:	1	1	1	1	1	1	1	1	1	1	1
SI 001 B		Shock: low (1-2)						Thickness: 1.0 mm				
Run 1	Z.A.:	0°	2°	4°	6°	8°	10°	14°	18°	22°	26°	30°
	O.D.:	0.6	0.6	0.6	0.6	0.6	0.6	0.6	0.6	0.6	0.6	0.6
Run 2	Z.A.:	0°	2°	4°	6°	8°	10°	14°	18°	22°	26°	30°
	O.D.:	0.6	0.6	0.6	0.6	0.6	0.6	0.6	0.6	0.6	0.6	0.6
Run 3	Z.A.:	0°	2°	4°	6°	8°	10°	14°	18°	22°	26°	30°
	O.D.:	0	0	0	0	0	0	0	0	0	0	0